DEVELOPMENT AND CHARACTERIZATION OF SINTERED POROUS BIOACTIVE GLASS SCAFFOLDS FOR MEDICAL APPLICATION

A THESIS SUBMITTED IN FULFILMENT OF THE REQUIREMENTS FOR THE DEGREE OF MASTER OF SCIENCE IN METALLURGICAL ENGINEERING

OF

THE UNIVERSITY OF NAMIBIA

BY

LINUS TSHIIMI ANGULA

201203016

October 2024

MAIN SUPERVISOR: Prof. Oluwagbenga Johnson

University of Namibia

School of Engineering and the Built Environment

CO-SUPERVISOR: Prof. Mxolisi Shongwe

Tshwane University of Technology, Pretoria, South Africa

School of Chemical and Metallurgical Engineering

DECLARATIONS

I, Linus Angula, hereby declare that this study is my own work and is a true reflection of my research and that this work, or any part thereof, has not been submitted for a degree at any other institution.

No part of this thesis/dissertation may be reproduced, stored in any retrieval system, or transmitted in any form or by means (e.g. electronic, mechanical, photocopying, recording or otherwise) without the prior permission of the author or the University of Namibia on that behalf.

I, Linus Angula, grant the University of Namibia the right to reproduce this thesis in whole or in part in any manner or format which the University of Namibia may deem fit.

Linus Tshiimi Angula	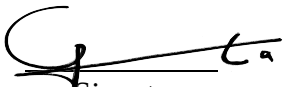	12.08.2024
Name of Student	Signature	Date

ABSTRACT

There is an ongoing effort to innovate engineering materials that are used in medical applications to support, enhance, or replace damaged tissue or perform a biological function. This study focuses on researching bioactive glass scaffolds resembling natural trabecular bone tissues that are widely used in medical applications. The research investigates the relationship between processing parameters and the resulting microstructures of borosilicate, borophosphate, and phosphate bioactive glass scaffolds. The study developed glass ceramics using traditional melt-quench methods; silicate composition S53B50 was processed at 1200 °C, while the P40B10 and Sr phosphate glasses were heated to 1100 °C. The sintering ability of the three types of glasses with a NaCl sacrificial pore-generating agent was achieved via spark plasma sintering technology at a rapid heat rate of 100 °C/min and temperatures ranging from 490- to 610- °C. The research work employed analytical techniques of thermogravimetric analysis (TGA), particle size analysis (PSD), X-ray diffraction (XRD), Fourier transform infrared spectroscopy (FTIR) and scanning electron microscopy (SEM) to gather data and characteristic results. It was observed that producing the glass ceramics by fritting the melts produced more desirable amorphous microstructures with less than 50% crystallization over casting and annealing. Also, the S53B50 scaffolds had the highest strength at 1.7 MPa and Sr glass had the most deformation at 1.62 mm. The findings are attributed to the partially crystallized microstructures, with indexes varying between 47 % and 58 %. Sintering increased scaffold density, compressive strength, and crystallinity while decreasing the porosity in this way demonstrating an ability to control scaffold properties for different applications through the sintering process. This research study contributes to the improvement of bioactive glass scaffolds and their potential applications in the clinical sciences of drug delivery systems.

LIST OF PUBLICATIONS

1. **Linus T. Angula**, Oluwagbenga T. Johnson, Mxolisi B. Shongwe and Petrina Kapewangolo (2024): “A Review Analysis of Porous Bio-Active Glass Development and their Multifaceted Clinical Application”. Under review for the Journal of Materials Science: Materials in Medicine.

2. **Linus T. Angula**, Oluwagbenga T. Johnson and Mxolisi B. Shongwe (2024): “A Comparative Study of Fritting and Casting Methods in the Synthesis of Melt-derived Bioactive Glass Scaffolds” To be submitted to the Science Direct journal of Results in Materials.

3. **Linus T. Angula**, Oluwagbenga T. Johnson and Mxolisi B. Shongwe (2024): “Microstructural and Mechanical Properties Analysis of Spark Plasma Sintered S53B50, P40B10 and Sr Bioactive Glass Scaffolds” To be submitted to the Science Direct journal of Results in Engineering.

4. **Linus T. Angula**, Oluwagbenga T. Johnson, Petrina Kapewangolo and Mxolisi B. Shongwe (2024): “Loading and Release Analysis of Hoodia Gordonii in Borosilicate, Borophosphate, and Phosphate Porous Bioceramic Glass Scaffolds” To be submitted to the International Journal of Pharmaceutics.

5. **Linus T. Angula**, Oluwagbenga T. Johnson, Mxolisi B. Shongwe and Petrina Kapewangolo (2022): “The Effect of Bioactive Glass Characteristics and Properties on the Controlled Drug Delivery Performance of Bioglass Scaffolds” Abstract presented at the University of Namibia Annual Research Conference on Agriculture, Engineering and Natural Sciences 2022.

TABLE OF CONTENTS

LIST OF FIGURES

LIST OF TABLES

LIST OF ACRONYMS AND ABBREVIATIONS

BG	Bioactive Glass
COD	Crystallography Open Database
DSC	Differential Scanning Calorimetry
EDS	Energy Dispersive Spectroscopy
FTIR	Fourier Transform Infrared Spectroscopy
HA	Hydroxyapatite
IB	Bioactivity Index
ICDD	International Centre for Diffraction Data
MBG	Mesoporous Bioactive Glass
PSD	Particle Size Distribution

SBF	Simulated Body Fluid
SEM	Scanning Electron Microscopy
SPS	Spark Plasma Sintering
TGA	Thermogravimetric Analysis
XRD	X-Ray Diffraction
T_g	Glass transition temperature
T_c	Glass crystallisation temperature
Mol. %	Mole percent

ACKNOWLEDGEMENTS

This journey, filled with challenges and learnings, has not only broadened my understanding of Material Science but also enriched me with invaluable life lessons. I find myself reflecting on the myriads of influences and support systems that have shaped this endeavour.

Firstly, I extend my deepest gratitude to Professor Johnson and Professor Shongwe. Your mentorship transcended the traditional roles of academic guidance. The paradigm shift you facilitated in my approach has left an indelible mark on my academic and personal growth. Henry Adams rightly said, "A teacher affects eternity; he can never tell where his influence stops."

Secondly, acknowledging the academics who laid the groundwork for my research is essential. Their extensive work provided a solid foundation for my study, embodying the adage, "If you add a little to a little, it soon becomes great."

Thirdly, to my parents, siblings, friends, and partner – your unwavering faith in me has been my stronghold. The environment of love, encouragement, and belief you provided has been vital in my journey. Earl Nightingale's definition of success as "the progressive realisation of a worthy goal" resonates deeply with me, as every day spent in your company and support has been a step towards success. Furthermore, I extend my appreciation to the technical staff and my peers at UNAM, Tshwane University of Technology (TUT) and University of Johannesburg (UJ). Your assistance, discussions, and feedback have been invaluable to me.

Lastly, I acknowledge the financial and resource support provided by the Federal Ministry of Education and Research (BMBF - Bundesministerium für Bildung und Forschung) MedPlantOS project team. This support was crucial in facilitating the research and is greatly appreciated. This thesis is not just a reflection of my work, but a mosaic of the contributions and support of each one of you. Thank you for being a part of my journey to mastery.

CHAPTER 1: INTRODUCTION

1.1 Motivation

Biomaterials come in various forms, such as powders and injectable nanoparticles, and can act as a structure like construction scaffolding but for biological purposes. In this context, cells work like builders, using the scaffold to create tissue. As the scaffold gradually breaks down, osteoblasts (bone-forming cells) move in and build the foundational elements of the tissue, leading to tissue growth. For a material to be suitable as a biomaterial, it must be biocompatible (safe for use in the body), non-reactive, mechanically strong, and easy to shape.

A particularly important group of biomaterials are bioceramics and bioactive glasses. These materials are preferred for use in clinical settings, such as implants, because their chemical and physical properties closely resemble those of human bone. Therefore, bioactive ceramic glasses are extensively used in orthopedics. They serve as scaffolds for regenerating and repairing soft and hard connective tissues and as vehicles for delivering drugs directly to specific sites in the body (Kumar, Kundu and Datt, 2011).

Immunization therapies, particularly those involving protein vaccine delivery, play a critical role in combating infectious diseases (Migneco *et al.*, 2020a). Additionally, the delivery of proteins and drugs is key in regenerative medicine for repairing and replacing damaged tissues and organs. There is a growing focus on controlled drug release systems that offer targeted, efficient drug delivery to specific sites of injury or infection, aiming to reduce side effects associated with traditional drug administration methods. With decreasing life expectancy, there is a demand for innovative materials to address the challenges of aging and tissue degeneration. This study aims to develop and evaluate mesoporous bioactive glasses for delivering medicinal plant extracts, showcasing their potential in improving treatments in orthopedics and beyond.

1.2 Theoretical Background

As people age, their bodies face deterioration and various health challenges. Often, medical treatments alone cannot fully restore health, necessitating the use of external aids to support bodily functions. Biomaterials are designed for this purpose, to be implanted in the body to repair damaged tissues (Ribeiro, Oliveira and Reis, 2022). Initially created to be inert and not react with bodily tissues, the focus has shifted towards developing bioactive materials that can interact with the body, encouraging cell regeneration and fighting off pathogens.

According to Hench (2006) and Kumar, Kundu and Datt, (2011), bioactive materials for clinical use are categorized into two types: Class A and Class B. Class A bioactive glass-ceramics promote bone growth directly on their surface, a process known as osteoconductivity, and can also activate cells to induce bone formation, known as osteoinduction. Class B materials, in contrast, only support osteoconductivity.

Gerhardt and Boccaccini (2010) explain that bioactive glass scaffolds are designed as highly porous, three-dimensional structures that facilitate cell attachment, proliferation, and differentiation into healthy bone tissue, all while gradually breaking down at a controlled rate. A key benefit of bioactive glasses is their ability to form hydroxyapatite (HA), $Ca_{10}(PO_4)_6(OH)$, layer when in contact with body fluids (Fig. 1-1), a critical feature for their effectiveness in medical applications.

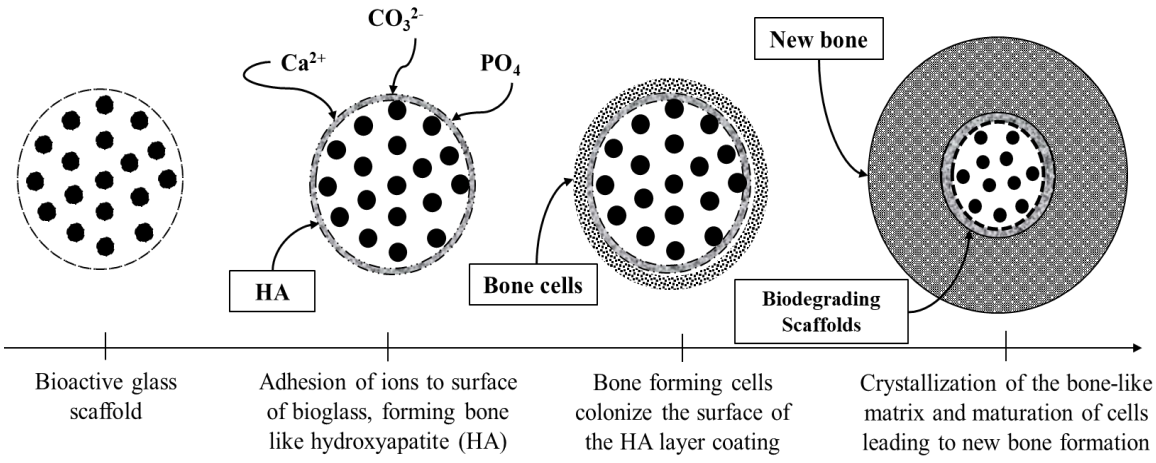

Figure 1-1: Bioactive Glass Scaffold Schematic Diagram of Bone Regeneration (Jones *et al.* 2010).

Bioactive glass production has been advanced through methods like melt derivation, sol-gel processes, and freeze casting as outlined by Rainer *et al.*, (2008), Lin *et al.* (2009), and Veljović *et al.* (2009). Melt quenching is straightforward but may struggle to achieve a consistent amorphous structure. The sol-gel technique allows for precise control over the material's composition and structure, although it typically requires extra steps to enhance mechanical properties. Freeze casting is effective for creating porous structures but demands precise control over freezing conditions.

Jones *et al.* (2010), highlight that optimizing scaffold structures to improve bioactivity and mechanical strength presents a challenge. Bioactivity influences factors like degradation rates and cell attachment, while porosity impacts mechanical strength and the available surface area for tissue regeneration. The effectiveness of porous scaffolds, in terms of both mechanical support and biological compatibility, depends on the material's composition, microstructure, and the production methods used. Enhanced mechanical strength ensures stability in load-bearing applications until new tissue can form.

Crucially, controlling porosity is essential for tailoring the scaffold's mechanical properties, offering the necessary support, flexibility, and space for tissue growth. Additionally, surface

modifications of the scaffolds play a significant role in their mechanical integrity and how well they integrate with existing tissue.

1.3 Statement of the Problem

The main obstacles in creating bioactive glass (bioglass) scaffolds are achieving an amorphous structure and ensuring they are mechanically adaptable for various bodily functions. An amorphous structure, lacking long-range atomic order, is preferred in bioglass scaffolds because it facilitates dissolution and ion release, key for stimulating cellular responses and enhancing bioactivity. Meanwhile, mechanical adaptability is critical for replicating the properties of natural tissues, ensuring scaffolds can support proper load, flexibility, and stress distribution.

Developing bioglass scaffolds that combine an amorphous structure with mechanical adaptability involves navigating complex challenges, including the selection of fabrication techniques. Sol-gel derived bioactive glasses, for example, offer improvements over melt-derived counterparts by supporting a broader range of bioactivity and compositions, with SiO_2 content of up to 90% compared to the 60% limit of melt-derived glasses. This method also increases surface area and porosity, which enhances bone bonding and degradation. However, the inconsistency in pore distribution can hinder their effectiveness in medical applications.

A significant limitation with current bioglass scaffolds is their poor mechanical strength and the difficulty in maintaining an amorphous state during production, critical for optimal hydroxyapatite formation in simulated body fluid (SBF). This research focuses on examining the sintering capabilities of different types of bioactive glasses, including borosilicate, borophosphate, and phosphate, to address these challenges.

1.4 Research Aim and Objectives

The aim of the research study is to develop and characterize porous bioactive glass scaffolds for medical applications. The objectives are to:

i. Prepare highly porous scaffolds with a pore generating agent.
ii. Determine time-temperature sintering conditions without adverse crystallization.
iii. Examine mechanical behaviour of the porous scaffolds.

1.4.1 Research Study Question

Can Spark Plasma Sintering rapidly fabricate highly porous bioactive glass ceramic scaffolds while maintaining an amorphous state with low crystallization?

1.5 Scope of Research

This study involved mixing dry chemicals that produced three different types of ceramic glasses by melting and annealing method. The glasses are characterized as they are developed to scaffolds by sparks plasma sintering (SPS). Characterization involved thermogravimetric analysis (TGA), particle size analysis (PSD), X-ray diffraction (XRD), and Fourier transform infrared (FTIR) and scanning electron microscopy with energy dispersive spectroscopy (SEM-EDS).

1.6 Structure of Thesis

This thesis comprises of an introductory Chapter 1 and a review of the literature, which is presented in Chapter 2. This chapter provides the fundamental concepts that are pertinent to the investigation. Chapter 3 introduces the research methodology, which outlines the experimental and characterization techniques that have been employed in this study. The findings are documented in Chapter 4 and subsequently discussed in Chapter 5. In Chapter 6, the thesis is concluded by discussing key findings and proposing a forward-thinking approach to expand on this study.

CHAPTER 2: LITERATURE REVIEW

This chapter comprehensively covers various aspects of bioactive glass materials published in recent literature. It begins with an introduction to bioactive glass, detailing its evolution from traditional glass compositions. The chapter then explores the properties of bioactive glass, including biocompatibility, bioactivity, and mechanical characteristics. It delves into the synthetic development of bioactive glasses, discussing methods like melting derivation and solution gelation, along with fabrication methods for bioactive glass scaffolds. The chapter also examines the porosity of these scaffolds and the techniques used for their characterization. Different types of bioactive glass scaffolds are discussed, including silicate-based, borate-based, and phosphate-based, with a comparison of their features. Lastly, the chapter addresses the application of these scaffolds in drug delivery, highlighting the commercial viability of mesoporous bioactive glass (MBG) drug delivery systems.

2.1 Introduction to Bioactive Glass Materials

The concept behind using bioactive glass as implant material is that it can form a strong and rapid bond with the surrounding tissue, eliminating the need for mechanical fixation. Hench, (2006) made a groundbreaking discovery that sparked significant interest in the field of bioactive glasses and glass ceramics as biomedical materials. It was found that certain glasses composed of SiO_2-CaO-Na_2O-P_2O_5 did not trigger the formation of fibrous tissue upon contact with living tissue; instead, these glasses chemically bonded to the biological tissues. This discovery paved the way for further research and development into bioactive glasses (Jones, 2013). The unique property of bioactive glasses stems from their ability to undergo kinetic modification upon implantation. Upon contact with living tissue, the surface of bioactive glass develops a biologically active layer known as hydroxycarbonate apatite (HCA). The formation of this HCA layer enables the bonding between the implant and tissues.

Bio ceramics and bioactive glasses are subcategories within biomaterials that find extensive use in medical applications. They serve as scaffolds which are designed to mimic the structure of trabecular bone, providing a framework for new bone growth. They are commonly used as implant materials for repairing tissue and interacting with biological systems for diagnosis and treatment of diseases and ailments (Rousselle *et al.*, 2019; Domingues Goncalves, Balestri and Reinwald, 2020; Park *et al.*, 2023). These materials can be bioabsorbable or non-degradable, and they should be nontoxic, biocompatible, and not trigger a negative immunological response (Valente, Brolo and Suleman, 2020). They are designed to provide suitable surface area-to-volume ratios, porosities, pore interconnectivities, and mechanical strengths (Rubežić *et al.*, 2020). Biomaterials can be functionalized to enhance their bioactivity, such as through surface modification using proteins, incorporation of bioactive drugs, growth factors, or cells. They are used in various applications including nerve, lung, skin, orthopaedic tissues, and drug delivery. Biomaterials play a crucial role in tissue regeneration, controlled drug release, and creating local bioactive microenvironments to promote cellular responses and tissue repair. They are also used in bone regeneration, orthopaedic/dental implants, wound healing, and tissue engineering.

2.1.1 History of Traditional Glass Composition

Traditional glass composition has a long and rich history that dates back thousands of years. From its origins in ancient civilizations such as Mesopotamia and Egypt, traditional glass composition has evolved over time to meet the diverse needs and demands of society. The age of glass science began in 1886 with the publication of the catalog of Schott und Genossen, which contained 44 optical glass compositions (Kurkjian and Prindle, 2005). Since then, there have been major discoveries and changes in glass composition. One example is a glass composition that includes soda-lime base glass materials, an oxide of vanadium for ultraviolet light blocking properties, and an oxide of selenium for clarity and

decolorization (Sayre and Smith, 1961). Additionally, there are glass compositions that include components such as P_2O_5, SiO_2, B_2O_3, Al_2O_3, ZrO_2, and group I-based oxides (Choi, Youngseok and Choi, 2018). These examples demonstrate the diverse range of components used in traditional glass compositions throughout history.

These fundamental constituents, when subjected to high temperatures during the melting process, undergo a chemical reaction resulting in the formation of an amorphous and translucent material with diverse properties and countless applications (Rawlings, Wu and Boccaccini, 2006). Silica provides stability to the glass structure while alkalis like soda ash or potash act as fluxes that lower the melting point, thus facilitating the production process. Lime functions as a stabilizing agent for alkaline materials by improving their durability and resistance to wear effects. Glass is a unique material that lacks a regular crystalline structure, instead having a disordered arrangement of atoms. This amorphous structure gives glass its distinct properties, such as transparency and the ability to be shaped into various forms. The structure of glass is different from that of crystals, which have a highly ordered arrangement of atoms (Gavinho *et al.*, 2019). The ability of a substance to form a stable glass or crystal from a melt is influenced by the differences or similarities between the local structures of glasses and crystals of the same composition (Muñoz and Sánchez-Muñoz, 2019).

The chemical structure of the Silica-Soda-Lime traditional glass network is characterized by the presence of Na^+ and Ca^{2+} ions within the silica network shown in Figure 2-1 (Nandi *et al.*, 2016). These ions have different structural organizations, with Ca^{2+} ions having a greater affinity for non-bridging oxygens than Na^+ ions. The structural behavior of these ions is linked to their different diffusivities, with Na^+ ions diffusing faster than Ca^{2+} ions due to their bonding to a smaller number of non-bridging oxygens. The formed ionic bonds are also less strong in the case of Na^+ ions (Serva *et al.*, 2020).

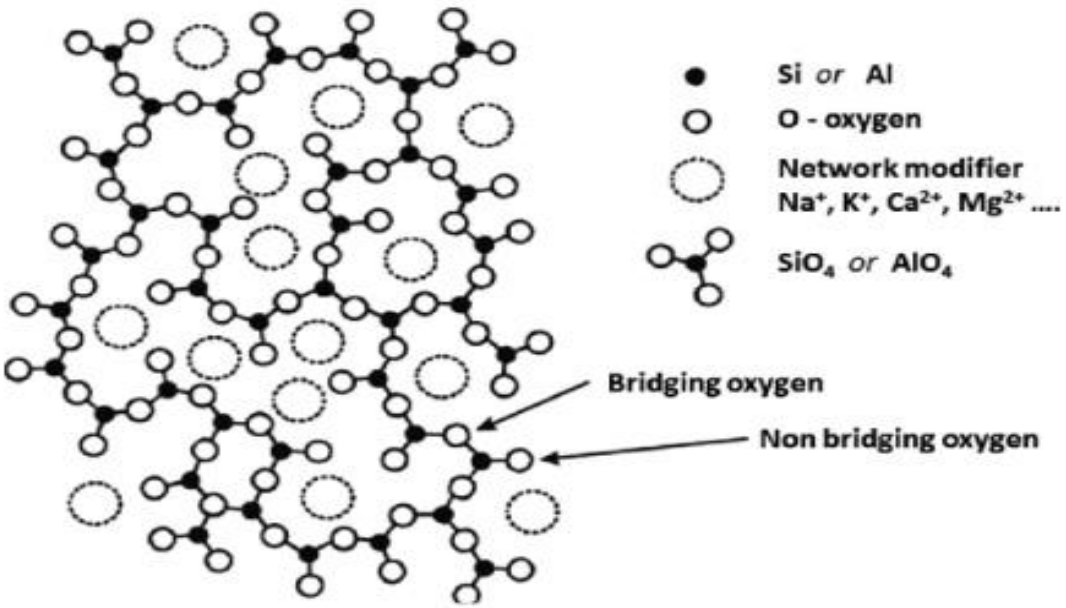

Figure 2-1: Schematic Representation of a Typical Bioactive Glass Network Including Modifiers, Bridging and Non-Bridging Oxygen (Nandi *et al.*, 2016).

2.1.2 Transition from Traditional to Bioactive Glass

Advancements in glassmaking techniques and scientific understanding have led to the development of bioactive glass materials with unique compositions and properties. These bioactive glasses promote biological activity and integration with living tissue. The first bioactive glass composition, 45S5, was able to bond to living bone and stimulate osteogenesis through the release of biologically active ions (Baino, Hamzehlou and Kargozar, 2018). Glass-ceramics with high strength and toughness have been successfully developed, and efforts are being made to further improve their damage resistance (Fu, Beall and Smith, 2017). A new bioactive glass composition has been developed that shows high stability against crystallization, high bioactivity, and the ability to be formed into complex 3D shapes, making it a potential alternative for tissue regeneration (Souza *et al.*, 2017). Inorganic composite bioactive glass has been incorporated into mechanical 3D scaffolds, increasing their compressive strength for bone regeneration (Lemos, Patrício and Pereira, 2016).

Bioactive glasses have unique properties that make them highly versatile in regenerating hard tissues such as bones and teeth. They have advantages like strong interfacial bonding, stimulating osteogenesis, and forming a hydroxyapatite layer when implanted. They are used in millions of patients worldwide for repairing bone and dental defects and have potential for soft tissue repair and drug delivery (Baino, Hamzehlou and Kargozar, 2018). The development of bioactive glasses has gone through several eras, says Hench, (2013), with the sol-gel method replacing conventional glass processing methods. They have applications in dentistry, including remineralization and hypersensitivity treatment (Hench, 2015; Me, Mh and Bagheri, 2015).

The chemical reactivity of bioactive glasses can be precisely controlled by adjusting their composition and heat treatment protocols. This control over reactivity is a unique advantage of bioactive glasses compared to other materials used for bone grafting or implantable devices (Baino, Hamzehlou and Kargozar, 2018). The surface reactions of bioactive glasses with living bone, which lead to the formation of a bone-bonding hydroxyl-carbonate apatite layer, were crucial in the early development of these biomaterials (Haque *et al.*, 2020).

The synthesis of bioactive glass nanoparticles has been a focus of research, with applications including drug delivery systems, injectable materials, scaffolds, and coatings for implants. Mesoporous bioactive glasses, synthesized via sol-gel routes, have further expanded the possibilities for bone regeneration and the incorporation of therapeutic ions (Baino, Fiorilli and Vitale-Brovarone, 2017). For instance, strontium, zinc, cobalt fluoride and magnesium are incorporated into some newly developed compositions, presenting improved therapeutic effects when released inside the body (Nandi *et al.*, 2016). This innovative strategy has shown promising results in the development of bioactive glasses with inherent antibacterial properties. Furthermore, Bioactive glasses have been investigated as carriers for controlled

drug release, including antibiotics, growth factors, and anti-inflammatory drugs. Studies have shown that bioactive glasses can effectively release these medicinal agents (Cannio *et al.*, 2021; Nasr Azadani *et al.*, 2021). The use of bioactive glasses in dentistry, reconstructive surgery, and the treatment of infections has shown potential bioactivity and biocompatibility (Migneco *et al.*, 2020a). The sol-gel method is commonly used to prepare drug carriers, including bioactive glasses, due to its simplicity and ability to produce particles with high homogeneity and purity (Rana *et al*, 2020).

Mesoporous bioactive glasses (MBGs) have been developed, which exhibit ultrafast mineralization rates and can be used for sustained drug delivery (Chyzy, Tomczykowa and Plonska-Brzezinska, 2020). The versatility of oxide-based glass systems has been expanded with the development of MBGs, allowing for their potential use in biomedical applications in the field of drug delivery, where they can be utilized to provide localized and targeted therapy.

2.2 Properties of Bioactive Glass Material

Bones possess the remarkable capability of undergoing self-regeneration, wherein any bone that sustains damage in any manner can reproduce and repair itself autonomously. Nevertheless, when faced with extensive damage, bone tissues are unable to regenerate to fill the void created by the injury. Consequently, alternative materials are employed to occupy the damaged area and aid in the growth of new tissues that possess the same strength as the original bone. The efficacy of bioglasses in that regard stems from its highly compatible nature with the human body, specifically with bone tissues (Jones *et al.*, 2016). Its ability to efficiently facilitate the healing process in the defected area can be attributed to its remarkable biocompatible and bioactive capacity to interact with the host response in a suitable manner. Bioactivity and biocompatibility may appear to have similar meanings, but they are actually distinct concepts; bioactivity refers to the effects of an agent on living

matter or tissues, while biocompatibility relates to the compatibility and lack of toxic or immunological response of a material when exposed to living tissues in the body (Haque *et al.*, 2020).

2.2.1 Biocompatibility

Biocompatibility in relation to bioactive glasses pertains to their capacity to interact harmoniously with living tissues, without eliciting any undesirable effects. This entails a comprehensive assessment of the materials' influence on cellular activity, encompassing critical aspects such as cell proliferation, viability, and differentiation, as well as their potential to incite an inflammatory response. Numerous scientific investigations have been conducted to explore and shed light on the biocompatibility of diverse bioactive glasses. Wuersching *et al.*, (2023), for instance, conducted a study where they discovered that two newly developed bioactive restorative materials exhibited highly favorable biocompatibility characteristics, as evidenced by the presence of a healthy cell morphology and the absence of any adverse effects on host cells. In a similar vein, Sergi *et al.*, (2020) undertook research aimed at enhancing the biocompatibility of bioactive glass, resulting in the development of a variant that showcased heightened cellular viability when compared to the standard bioactive glass. Moreover, Bellucci *et al.*, (2020) employed a three-dimensional cellular model to meticulously evaluate the biologic performance of bioactive glasses, ultimately revealing that the novel glass compositions exhibited superior biocompatibility in comparison to the conventional glass. Additionally, Anand *et al.*, (2019) dedicated their efforts to the exploration of mesoporous bioactive glasses, ultimately concluding that these materials demonstrated minimal toxicity and were deemed suitable for employment within the realm of bone tissue engineering. Finally, Arepalli *et al.*, (2019) directed their attention towards the assessment of the blood compatibility of magnesia-doped bioactive glasses, and

their findings were indicative of an augmented level of bioactivity and biocompatibility when compared to their non-magnesia-doped counterparts.

As an outcome of various interactions occurring at the interface between bioactive glass and adjacent tissues, a dynamic layer is formed to actively facilitate integration mechanisms while promoting bonding at the site. Typically comprising steps including ion exchange phenomena alongside matrix dissolution/re-crystallization stages resulting hydroxyapatite precipitation ensure cellular attachment as well as proliferation., and ultimately the formation of new bone tissue. Thus, the ability to form a durable and resilient connection with living tissues, is the phenomenon known as bioactivity with regards to bioglasses.

2.2.2 Bioactivity

Bioactivity refers to the ability of the glass to form a strong bond with living bone or tissue when exposed to body fluids, leading to the formation of a hydroxyapatite layer (Stanic, 2017; Baino, 2018). This bioactive behavior is crucial for the integration of the glass with the surrounding tissues and for promoting osteogenesis, angiogenesis, and antibacterial activity (Saravanakumar, Rajkumar and Rajendran, 2011). Generally, the interface of a bioactive glass in vitro testing undergoes the five reaction stages described below (Hench, 2006; Baino, 2018).

1. Leaching and the formation of silanols, as cation exchange occurs involving the substitution of monovalent and divalent cations, specifically Na^+ and Ca^{2+}, within the glass, as well as H^+ ions from the solution. As a result, silanol bonds (Si-OH) are formed on the glass surface through Equation 2.1:

   $$Si\text{-}O\text{-}Na^+ + H^+ + OH^- \rightarrow Si\text{-}OH^+ + Na^+_{(aq)} + OH^-$$

   The pH of the solution rises, and a silica-rich layer is created. If phosphate ions are present in the glass composition, they may also be released.

2. The loss of soluble silica and further formation of silanols as the cation exchange reaction progresses and the pH increases, hydroxyl ions attack the Si-O-Si bonds. When Si-O bonds are broken, soluble silica ($Si(OH)_4$) is lost in the solution following Equation 2.2:

$$Si\text{-}O\text{-}Si + H_2O \rightarrow Si\text{-}OH + OH\text{-}Si$$

This leads to an increase in the number of silanols at the interface between the glass and the fluid.

3. Polycondensation of silanols as hydroxyl groups can react and combine with one another as follows in Equation 2.3.

$$Si\text{-}OH + OH\text{-}Si \rightarrow Si\text{-}O\text{-}Si$$

Resulting in the formation of a silica-rich amorphous layer known as silica gel. The silica gel layer has the capability to absorb ions from the solution and provides a favorable environment for the precipitation of HA.

4. Calcium (Ca^{2+}) and phosphate (PO_4^{3-}) ions diffuse through the silica gel layer from both the solution and the gel itself following Equation 2.4:

$$CaO + P_2O_5 \rightarrow CaO\text{-}P_2O_5$$

Leading to the formation of an amorphous film rich in CaO and P_2O_5 on top of the silica gel layer.

5. The final stage involves the crystallization of the calcium- and phosphate-rich layer, resulting in the formation of HA as shown in Equation 2.5:

$$CaO\text{-}P_2O_5 + OH^- + CO_3^{2-} \rightarrow Ca_5(PO_4, CO_3)_3(OH)$$

The presence of additional ionic species, such as carbonates (which migrate from the solution to the glass surface) and ions released by the glass, can cause the HA formed on the implant surface to be non-stoichiometric and instead consist of a mixed apatite comprising hydroxycarbonates.

The level of bioactivity of a material, in terms of its interaction with the host bone, can be estimated using the bioactivity index, I_B. This index is defined as the number of days required for 50% of the material surface to bond with living tissue (Kim, Clark and Hench, 1989):

$$I_B = \frac{100}{t_{0.5\ bb}}$$

Days required for half the material surface to be bonded are denoted by $t_{0.5\ bb}$. It has been reported that the thickness of the bonding zone between a bioactive implant and bone is directly proportional to the I_B value (Hench, 1991). When the goal is to restore large bone defects, the formation of new blood vessels through angiogenesis is crucial for ensuring the delivery of nutrients, growth factors, and oxygen, as well as facilitating the arrival of stem cells to the injured site. Bioactive silicate glasses have been shown to significantly enhance angiogenesis, both in laboratory settings and in living organisms (Kargozar, Baino, *et al.*, 2018b). While the bioactivity mechanism described above was initially developed for a specific type of silicate glass, it can generally be applied to most types of silicate bioactive glasses (Rahaman *et al.*, 2011). Additionally, it has been noted that the presence of crystalline phases in bioactive glass-ceramics leads to slower bonding kinetics and bone regeneration rates (Oonishi *et al.*, 1999, 2000).

Furthermore, glasses containing B_2O_3 as a network former or co-former oxide exhibit a bioactivity mechanism similar to that of silicate glasses, but with faster apatite formation kinetics (Liu *et al.*, 2010). On the other hand, phosphate glasses have a tendency to rapidly dissolve in aqueous environments(Knowles, 2003), which often prevents the formation of a stable surface apatite layer unless the glass composition is carefully designed to adjust and slow down the dissolution kinetics (Leonardi *et al.*, 2010).

Bioactive glasses can potentially form tissue attachments with bone through various mechanisms. One type of attachment is bony integration, where the bioactive glass promotes

the formation of new bone tissue and integrates with the existing bone structure (Sarker *et al.*, 2015). This attachment is beneficial as it provides mechanical stability and long-term durability. Another type of attachment is connective tissue vessel formation, where the bioactive glass stimulates the growth of blood vessels in the surrounding tissue (Shah and Czechowska, 2018). This attachment is important for the delivery of nutrients and oxygen to the healing site. However, there are also potential drawbacks to these attachments. Bony integration may lead to stress shielding, where the bioactive glass absorbs the load-bearing function of the bone, resulting in bone resorption and weakening (Kargozar *et al.*, 2019). Connective tissue vessel formation may cause fibrous encapsulation, where excessive scar tissue forms around the bioactive glass, limiting its integration with the surrounding bone tissue (Kargozar, Mozafari, *et al.*, 2018). Therefore, while tissue attachments between bioactive glasses and bone offer advantages in terms of bone healing and vascularization, careful consideration is needed to avoid potential complications.

2.2.3 Mechanical Properties of Bioactive Glass

The mechanical properties of bioactive glasses play a vital role in determining their suitability as biomaterials in various applications. To function effectively within the human body, these glasses must possess sufficient mechanical strength to withstand the physiological stresses and loads that they may encounter. This requirement includes the need for adequate compressive strength, tensile strength, and fracture toughness (Kargozar, Baino, *et al.*, 2018a). However, it is important to note that the mechanical properties of bioactive glasses can exhibit considerable variation depending on several influential factors, including composition, processing techniques, and test parameters (Stanic, 2017). Consequently, it can be quite challenging to compare and analyze the mechanical properties reported in the existing literature due to the diverse range of test setups and parameters employed in different studies (van Gestel *et al.*, 2018). Consequently, it is crucial to approach

the interpretation of mechanical testing results for bioactive glasses with great care and attention (Baino, Ferraris, *et al.*, 2019). This is particularly important given the fact that a thorough understanding and optimization of the mechanical properties of bioactive glasses are essential for their successful application in the fields of tissue engineering and regenerative medicine (Rahmati and Mozafari, 2020).

By utilizing techniques such as controlled crystallization and compositional control, researchers have been able to enhance the mechanical properties of bioactive glasses and glass-ceramics. These techniques involve sintering the materials and adjusting their composition to achieve desired properties. For example, in the study by Tian et al., high-strength mica-containing glass-ceramics were prepared from granite wastes by bulk crystallization, and the mechanical properties of the glass-ceramics were found to improve with increasing SiO_2/Al_2O_3 molar ratio (Tian *et al.*, 2022). Similarly, Hung *et al.*, (2023) tailored bioactive $CaO\text{-}SiO_2\text{-}P_2O_5$ glass-ceramics using a nucleating agent, resulting in high mechanical flexural strength and hardness. Loh *et al.*, (2023) investigated the role of sintering temperature on bioactive glass-ceramics and found that the sintering process improved the crystallization and hardness of the final product. These studies demonstrate the potential of controlled crystallization and compositional control in enhancing the mechanical properties of bioactive glasses and glass-ceramics. These, improved mechanical properties make the glass-ceramics more suitable for load-bearing applications, expanding their potential use in orthopedic implants and other medical devices. Therefore, the controlled crystallization of bioactive glasses into glass-ceramics offers a promising avenue for improving their mechanical properties. The transformation of bioactive glasses into glass-ceramics through controlled crystallization is an effective method for enhancing their mechanical properties (Silva *et al.*, 2021).

2.3 Synthetic Development of Bioactive Glasses

Bioactive ceramics and glasses for medical applications are synthesized using two distinct methods following the process routes shown in Figure 2-2 adopted from Stanic, (2017). One common method is melt-quenching, which involves melting the raw materials and rapidly cooling them to form a glass. Another method is sol-gel, where a precursor solution is prepared and then converted into a gel through hydrolysis and condensation reactions (Arango-Ospina and Boccaccini, 2022). These gels are then dried and heated to form a glass (Haque *et al.*, 2020).

In addition to these methods, researchers have also developed glass-ceramics by controlling the crystallization through sintering of bioactive glasses (Massera, 2020). By controlling the crystalline phase, overall crystallinity, and crystal size, the bioactivity, mechanical properties, and dissolution profile of the glass-ceramics can be improved (Tüncer, Yücesoy and Öksel Karakuş, 2022).

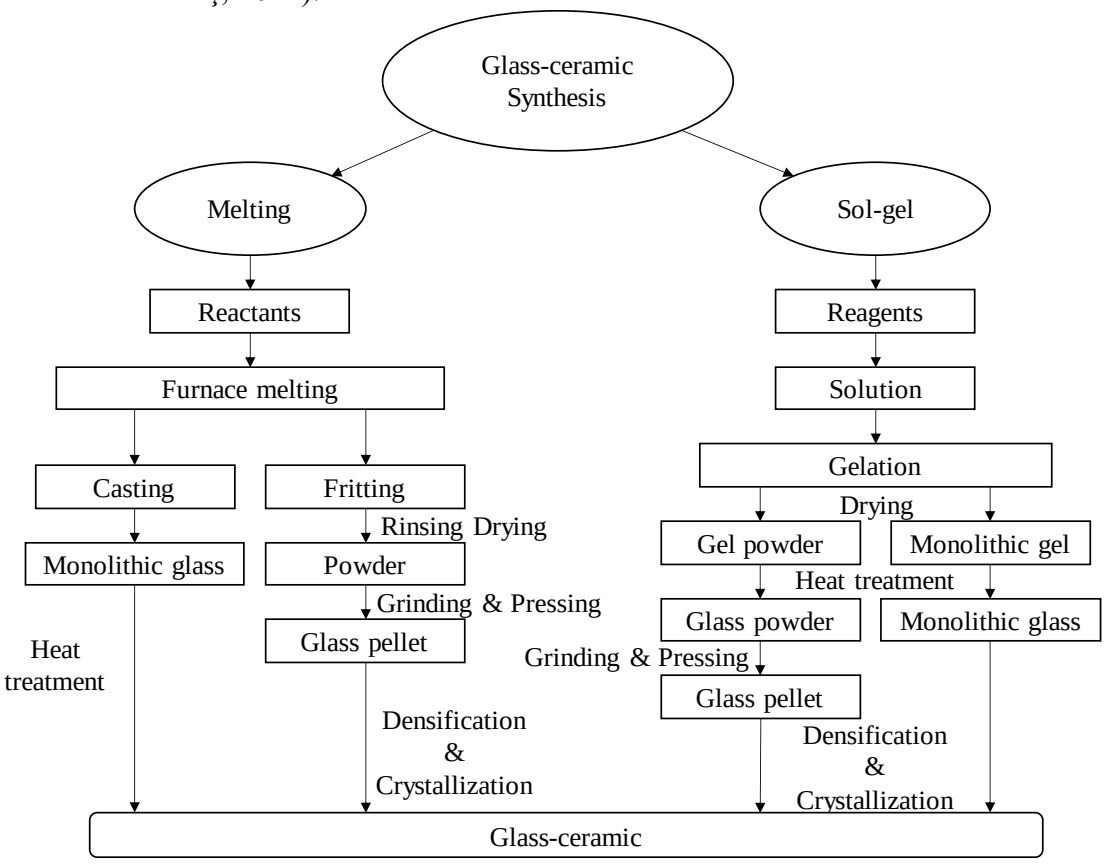

Figure 2-2: Process Flow Stages in the Synthesis of Glass-Ceramics (Stanic, 2017).

2.3.1 Melting Derivation of Bioactive Glasses

Melt quenching, a widely employed method, is utilized in the preparation of bioactive glasses. Historically, this technique has been employed in the development of various glasses, starting with bioglass 45S5 (Kokubo and Yamaguchi, 2016). The procedure entails melting a combination of constituent oxides of carbonates, with stoichiometric amounts and high purity, at elevated temperatures (Li *et al.*, 2019).

Powdered ingredients are subjected to high temperatures, surpassing 1100°C, leading to their melting, followed by a rapid cooling process to solidify the atomic structure (Skallevold *et al.*, 2019). Nonetheless, this technique poses certain challenges, such as diminishing bioactivity at higher sintering temperatures and the inability to fabricate porous scaffolds (Peitl Filho, LaTorre and Hench, 1996). The application of heat treatment can affect the mechanical properties of silica-based bioactive glasses, as it induces the formation of crystalline phases alongside the glassy phase, thereby causing stress release (Prasad, 2017). The crystallization of glass leads to a gradual decrease in ionic diffusivity and bioactivity (Skallevold *et al.*, 2019).

2.3.2 Solution Gelation of Bioactive Glasses

A recent study described the successful synthesis of a quaternary bioactive glass with a composition of $60SiO_2$–$34CaO$–$4MgO$–$2P_2O_5$ (mol%) using the sol-gel approach (Bento, Gaddam and Ferreira, 2021). Sol-gel processing technique has been recognized for its ability to produce silica glass with exceptionally low hydroxyl content since the early 90's (Prasad, 2017). The sol-gel method proves instrumental in fabricating 45S5 bioactive glass-ceramic. It offers advantages such as superior compositional control and the possibility to incorporate unique material properties (Vafa, Bazargan-Lari and Bahrololoom, 2021). It is a sophisticated chemical approach for the synthesis of single or multiple components in the form of thin solid films, ultrafine powders, high surface area porous materials, dense abrasive

materials, as well as continuous glass and ceramic fibers (Haque *et al.*, 2020). Research indicates that the heat treatment of bioactive glass within 550°C to 700°C can lead to precipitation, which influences its microstructural and functional properties (El-Ghannam, Hamzawy and Yehia, 2001).

The fabrication of oxide materials typically requires high temperatures, which poses a significant obstacle. However, the sol-gel method offers a wet chemical process to produce oxide materials at low temperatures. As a conventional and industrial method, sol-gel is still rarely employed for the synthesis of varied chemical compositions commercialized products as depicted in Table 2-1 below adopted from Baino, (2018).

Table 2-1: Examples of Bioactive Glass Compositions in Wt.%.

Glass name	Production	SiO_2	P_2O_5	B_2O_3	Na_2O	K_2O	CaO	MgO	CaF_2
45S5	Melting	45	6	–	24.5	–	24.5	–	–
S53P4	Melting	53	4	–	23	–	20		–
1-98	Melting	53	2	1	6	11	22	5	–
S55F5	Melting	52	5.8	–	19.6	–	11.7	–	10.9
Biosilicate	Melting	48.5	4	–	23.75	–	23.75	–	–
CEL2	Melting	43.8	6.9	–	15.0	6.1	23.6	4.6	–
ICEL2	Melting	1.9	66.4		9.7	3.9	15.2	2.9	–
13-93	Melting	53	4	–	6	12	20	5	–
13-93B1	Melting	34.4	3.8	19.9	5.8	11.7	19.5	4.9	–
13.93B3	Melting	–	3.7	56.6	5.5	11.2	18.5	4.6	–
58S	Sol-gel	58.2	9.2	–	–	–	32.6	–	–
70S30C	Sol-gel	71.4	–	–	–	–	28.6	–	–

Solution gelation involves the utilization of inorganic alkoxides and metal chlorides as precursors, which undergo hydrolysis and polycondensation reactions in an acidic or basic environment (Haque *et al.*, 2020). Subsequently, the sol undergoes further condensation

reactions to form a network with the liquid phase, resulting in gel formation and ultimately, the gel is sintered to create glass.

The preparation of a porous scaffold with bioglass using the melt quenching method presents a challenge due to crystallization during high-temperature sintering. Conversely, gel glasses possess a higher surface area, rendering them more bioactive in comparison to glasses produced by melt quenching (Li *et al.*, 2019). In this regard, the sol-gel method serves as an efficient approach. It enables the creation of a diverse range of glass compositions and shapes through the sol-gel process. Nonetheless, a combination of various technologies with either of the traditional synthesis routes, is possible to obtain porosity, apatite forming ability, and a greater surface area, surpassing the properties from a sole melt/sol-gel method. This ultimately leads to excellent mechanical properties (Haque *et al.*, 2020). However, it critical to note that bioactive glass powders exhibits specific behaviors during thermal treatments which are still argumentative, particularly crystallization, which can influence its final properties (Mecca, Bellucci and Cannillo, 2023).

2.3.3 Fabrication Methods of Bioactive Glass Scaffolds

A fundamental characteristic of scaffolds is their porosity, which is achieved through various fabrication methods. Sintering approaches of producing porous scaffold from glass-ceramic powders illustrated in Figure 2-3 typically involve the use of pore space holders, decomposing porogens, and sintering without the assistance of pore-forming agents. Pore space holders like NaCl are incorporated into the matrix and subsequently removed, creating voids. Decomposing porogens, such as PVA or $NH_4(HCO_3)$, are mixed with the matrix material and undergo decomposition upon heating, leading to the formation of pores. In contrast, the sintering process without any pore-assisting agent involves the thermal compaction of materials, where particles coalesce to form a solid mass, but without reaching the melting point. This process inherently can lead to some porosity due to the spaces left

between the particles, especially if not fully compacted (Cyster *et al.*, 2005; Wang and Zhang, 2010).

Traditional fabrication methods generally include:

- Powder Sintering: Traditional powder sintering of bioglass involves using metallurgy techniques (Badiee *et al.*, 2022) in a process that starts with synthesizing bioglass powders, then mixing them with other components for desired compositions and physical characteristics (Staniewicz-Brudnik *et al.*, 2022). The mixture is sintered in air atmosphere, heating powders for bonding and densification says Elsayed *et al.*, (2021). Resulting scaffolds have adjustable porous structure and mechanical properties (Hua *et al.*, 2021).
- Foam Replica Method: This is one of the older techniques utilized for the fabrication of 45S5 Bioglass® scaffolds. The process involves the use of a foam structure which acts as a template. The foam is impregnated with the bioglass slurry, and then subjected to heat treatment up to 1100 °C, during which the glass crystallizes and the foam structure is burnt out, leaving behind a porous bioglass scaffold (Fiume *et al.*, 2021).
- Melt Molding: This method is based on the use of thermoplastic polymers. The polymer is melted and then cast into a desired shape to create the scaffold. It is a straightforward conventional technique and has been a staple in scaffold fabrication for some time (Adel, ElMeligy and Elkasabgy, 2022).

Modern Techniques:

- Solid Freeform Fabrication (SFF): This is an umbrella term that includes various advanced techniques for scaffold fabrication. Some of the techniques under SFF are:
    - Three-dimensional Printing (3DP): It involves layer-by-layer printing of the scaffold material to achieve the desired structure.

- Fused Deposition Modeling (FDM): A continuous filament of thermoplastic material is deposited layer by layer in a predetermined path.
- Ink-jet Printing: Uses droplets of the scaffold material ejected from a nozzle to form the desired structure (Fu *et al.*, 2011).

▪ 3D Printed Porous Models: 3D printing of porous scaffolds differs from SFF in biomaterials by using techniques like binder jetting and liquid deposition modeling (LDM) with silicates or calcium phosphate (CaP) materials (Lu *et al.*, 2022). SFF employs photo-crosslink able polymer resins for rapid fabrication (Li *et al.*, 2021). 3D printing customizes scaffold shapes based on patient needs through computed tomography scans, while SFF focuses on lattice structures with controlled porosity percentages. Emerging trends in the field of 3D printing in tissue engineering, such as the integration of bioprinting with other technologies like stem cells, biomaterials, and bio fabrication techniques, are moving the technology to the forefront of the field (Veeman *et al.*, 2021).

Powder sintering remains a relevant method for producing porous bioactive ceramic glass scaffolds for medical applications. This method offers several advantages in fabrication. It allows for binder-free fabrication of bioactive scaffolds without the need for post-processing techniques (Kamboj, Ressler and Hussainova, 2021). The combination of precise composition synthesis with sintering of bioactive glass in the scaffold fabrication process provides biocompatibility, adaptive degradation, strength, and bioactivity (Jain *et al.*, 2022). The fabrication process can be optimized by adjusting the composition and heat treatment temperature, resulting in scaffolds with appropriate pore sizes for osteointegration and bone formation (Abdollahi *et al.*, 2021).

2.3.4 Porosity of Sintered Bioactive Glass Scaffolds

Sintered porous bioactive glass scaffolds are highly desirable for medical applications due to their special bone mimicking properties (Fu *et al.*, 2011). These scaffolds exhibit a three-dimensional porous structure that closely resembles the architecture of natural trabecular bone (Liu *et al.*, 2012). The intricate structure plays a crucial role in facilitating efficient cell infiltration and tissue ingrowth, thereby promoting seamless integration with the surrounding biological environment (Martelli, Bellucci and Cannillo, 2023).

The porosity of these bioactive glass scaffolds allows for enhanced transport of nutrients, oxygen, and metabolic waste products within the scaffold matrix (Hatton *et al.*, 2019). It also provides an excellent substrate for cellular adhesion and proliferation, fostering optimal tissue regeneration processes (Essien *et al.*, 2012). Moreover, this interconnected pore network facilitates vascularization by providing channels through which blood vessels can grow into the scaffold implant site.

Hierarchically, the bioactive glass scaffolds possess a unique combination of macro-, meso-, and micropores, which contribute to their overall functionality and performance (Fu *et al.*, 2011). The macroscopic pores, with diameters greater than 100 μm, promote cell infiltration and facilitate tissue ingrowth (Liu *et al.*, 2012). The mesopores, with diameters ranging from 2-50 nm, enhance the surface area available for ion exchange and promote bioactivity by allowing for the deposition of calcium and phosphate ions from body fluids (Martelli, Bellucci and Cannillo, 2023). The micropores, with diameters less than 2 nm, further enhance the bioactivity by providing additional sites for ion exchange and spreading of cell signalling molecules (Essien *et al.*, 2012).

2.3.4.1 Mesoporous Bioactive Glass Scaffolds

In recent years, mesoporous bioactive glass scaffolds have gained attention in the field of biomaterials due to their versatile applications and unique characteristics. These scaffolds

exhibit a highly ordered porous structure at the nanoscale, which allows for increased surface area compared to classical bioactive glasses. As such, mesoporous bioactive glass scaffolds hold great potential in drug delivery systems.

The mesoporous structure of these scaffolds enables efficient loading and controlled release of therapeutic agents (Wu and Chang, 2012). The large surface area facilitates high drug-loading capacities, while the pore arrangement provides pathways for sustained and targeted release (Schumacher, Habibovic and van Rijt, 2021). This capability offers significant advantages over traditional methods of drug administration by directly delivering therapeutics to specific tissues or cells.

By utilizing mesoporous bioactive glass scaffolds as carriers for therapeutic agents, it is possible to enhance treatment outcomes through improved efficacy and reduced side effects (Mansour *et al.*, 2023). Moreover, this technology presents opportunities for personalized medicine with tailored drug release profiles based on individual patient needs.

Overall, the emergence of mesoporosity in bioactive glass scaffold design opens new horizons in biomedical applications, particularly relating to enhanced control over drug delivery systems. It allows for the development of more effective treatments and therapies, promoting faster healing and improved patient outcomes (Wu and Chang, 2014).

2.3.4.2 The Impact of Porosity on Mechanical integrity

The impact of pore characteristics on the mechanical integrity of sintered porous bioactive glass scaffolds is an important consideration. The desired porosity allows for the infiltration of cells and tissue ingrowth, promoting proper functionality. The targets for cortical bone, are a higher range of compressive strength approximately 100 to 160 MPa require lower porosity of 30% to 70%, and for trabecular bone, a lower range of compressive strength of less than 10 to 60 MPa at higher porosity levels depicted in Figure 2-3 to approximate 60% to 90% (Baino, Ferraris, *et al.*, 2019).

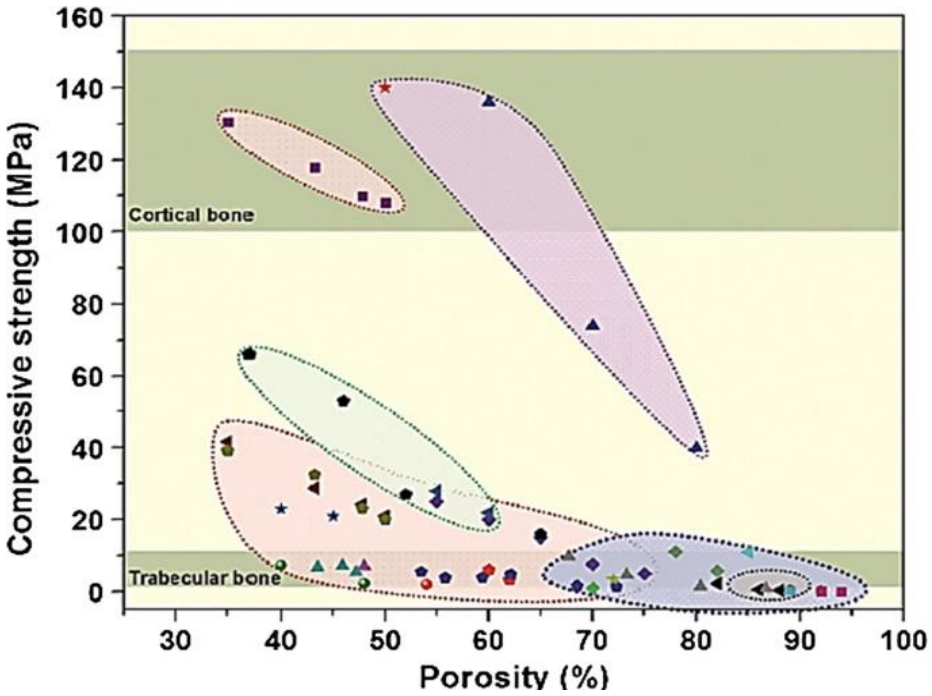

Figure 2-3: Compressive Strength as a Function of Porosity for Cortical and Trabecular Bone Structures.

However, the highly porous nature of these scaffolds can present challenges in terms of mechanical properties (Jeyachandran and Cerruti, 2023). Therefore, researchers must strike a balance between achieving the desired level of porosity in bioactive glass scaffolds and maintaining sufficient mechanical integrity. By optimizing the sintering process and controlling the composition of bioactive glasses, researchers aim to produce porous scaffolds that possess both high bioactivity and adequate mechanical strength (Baino and Fiume,

2019). This balance is crucial to ensure the success and longevity of these scaffolds in medical applications.

2.3.5 Characterization Techniques for Sintered Porous Scaffolds

In addition to the development of bioactive glass compositions that can be sintered without crystallization, it is also important to characterize and evaluate the properties of the sintered porous bioactive glass scaffolds. Several characterization techniques have been employed to assess the structure, morphology, mechanical properties, and bioactivity of these scaffolds. Thermal characterization, such as Thermogravimetric Analysis (TGA), Differential Thermal Analysis (DTA), and Differential Scanning Calorimetry (DSC), can provide information on the thermal behavior and crystallinity of the synthesized material for scaffold fabrication (González González *et al.*, 2022). Another commonly used technique is scanning electron microscopy, which allows for the elemental examination and imaging of the scaffold's surface morphology, pore size distribution, and interconnectivity (Bohorquez-Moreno, Öksüz and Dinçer, 2023).

Complementary techniques such as X-ray diffraction (XRD) and Fourier Transform Infrared Spectroscopy (FTIR), can be used to identify the phases present and degree of crystallization in the sintered bioactive glass scaffolds. These techniques provide valuable information about the structural and compositional properties of the scaffolds, which can help researchers understand the relationship between crystallization behavior and bioactivity in order to optimize the performance of these scaffolds for medical applications.

Mechanical properties, such as compressive strength and elastic modulus, can be determined through uniaxial testing to evaluate the load-bearing capacity of the scaffolds (Olăreț *et al.*, 2021) as discussed in the porosity impacts above. However, tribology wear analysis of bioactive glass scaffolds is a method used in this study to assess the resistance of these scaffolds to damage when they are subjected to mechanical stress, such as friction and wear.

As a result, this analysis provides valuable insight into the scaffold's durability and longevity in a real-world medical context (Araujo, Bartolomé and Mello-Castanho, 2020).

2.3.5.1 The Impact of Crystallization on Bioactivity

The impact of crystallization on the bioactivity of sintered porous bioactive glass scaffolds is a subject that remains in dispute within the scientific community. Extensive research has been conducted to investigate whether crystallization adversely affects the material's ability to promote biological activity (Baino, 2018). While certain studies suggest that crystallization can reduce bioactivity, there are contrasting findings indicating that specific compositions and levels of crystallization have negligible effects on the material's performance. To evaluate how crystal formation influences bioactivity, it is crucial to comprehend the relationship between glass composition and its propensity for undergoing partial or complete crystallization during sintering.

Crystallization can reduce the bioactivity of glasses by decreasing the surface area available for reactions with body fluids. The crystalline phases formed during heat treatment may not be as reactive as the amorphous phases (Montazerian *et al.*, 2024). The highly disrupted silica network prevalent in typical bioactive glasses poses challenges because it tends to favor crystal formation rather than remaining amorphous. Interestingly, studies have demonstrated that it might be possible to produce bioactive glasses with reduced crystallization tendencies. This can be achieved by using special formulations with high B_2O_3 content and partial or complete substitution of SiO_2 with P_2O_5. These formulations, offer wider thermal working ranges before crystallization temperatures as cited by Erasmus *et al.*, (2017), therefore their amorphous nature is preserved despite calcination at relatively high temperatures. However, defining an optimal level of amorphism isn't necessarily synonymous with achieving enhanced bioreactivity; researchers sought instead for easily

sinterable glasses devoid of undesirable signs of crystalline structure development (Bellucci *et al.*, 2014).

This desire for amorphous bioactive glasses stems from concerns that partially or fully crystallized bodies could compromise the structural integrity of the scaffolds and hinder their ability to promote cell attachment and proliferation. Crystallization in bioactive glass scaffolds can lead to a decline in the material's bioactivity. This decline in bioactivity may be attributed to a decrease in the rate of ionic dissolution, which is crucial for the release of biologically active ions and the formation of a bioactive layer on the scaffold surface. While crystallization can potentially reduce the bioactivity of sintered porous bioactive glass scaffolds, advances in production methods are offering promising solutions by minimizing this effect and maintaining the beneficial properties of these scaffolds.

2.4 Types of Bioactive Glass Scaffolds

Bioactive glass scaffolds can be classified into different types based on their composition, including silicate, borate, and phosphate-based scaffolds. Silicate-based bioactive glass scaffolds, such as those studied by Aalto-Setälä *et al.*, (2023), have been shown to dissolve incongruently, resulting in the formation of hydrous silica and subsequent precipitation of hydroxyapatite. Borate-based bioactive glass scaffolds, as investigated by Ensoylu *et al.*, (2022), have demonstrated improved mechanical strength and enhanced in vitro hydroxyapatite-forming ability when hexagonal boron nitride nanoparticles were incorporated into the glass matrix. Phosphate-based bioactive glass scaffolds, as discussed by Gomes *et al.*, (2023), involved the initial mixture of bioactive glass and hydroxyapatite particles, followed by heat treatment to induce structural changes and the formation of hydroxyapatite. These different types of bioactive glass scaffolds offer unique properties and potential applications in tissue engineering and bone regeneration.

2.4.1 Silicate-based Bioactive Glass Scaffolds

Silicate-based bioactive glass scaffolds are the most studied and utilized in the field of biomedical applications, tissue engineering, and drug delivery systems (Al-Harbi *et al.*, 2021). These scaffolds are predominantly composed of silicon dioxide (SiO_2) along with other oxides such as calcium oxide (CaO) and phosphorus pentoxide (P_2O_5). These scaffolds of bioactive glasses, glass-ceramics, and mesoporous systems are tailored to achieve controlled degradation rates that mimic tissue growth (Baino, Barberi, *et al.*, 2019). Silicate-based nanoceramics and bioactive glasses have been combined with different polymeric systems to form nanocomposites with enhanced mechanical properties and improved biological performance (Liang *et al.*, 2021). Recent advancements in additive manufacturing/3D printing techniques, such as robocasting, have enabled the fabrication of macroporous silicate-based bioactive glass scaffolds with suitable mechanical properties and bioactivity (Ben-Arfa and Pullar, 2020). Sol-gel-synthesized bioactive glasses, including high-silica-content sol-gel bioactive glasses, have shown promise in robocasting applications, offering greater porosity and bioactivity compared to melt-produced glasses.

2.4.2 Borate-based Bioactive Glass Scaffolds

Borate-based bioactive glass scaffolds have gained attention due to their unique properties, including high glass transition temperature, low melting temperature, and good solubility. These scaffolds are composed of boron oxide (B_2O_3) along with other oxides such as calcium oxide (CaO) and sodium oxide (Na_2O). These scaffolds have shown therapeutic and regenerative effects in vivo (da Silva *et al.*, 2022). Borate glasses and borosilicate glasses, which are types of borate-based bioactive glasses, have the ability to convert to apatite and/or an apatite-like phase and directly bond to bone and the degradation rate of borate-based bioactive glasses can be matched with that of the target tissue (Bromet *et al.*, 2023). Concerns regarding the cytotoxicity of borate bioactive glasses have been addressed, as recent studies

have shown little to no cytotoxicity in vivo and enhancement of tissue regeneration (Yamaguchi, 2022). Titanium-containing borate bioactive glass scaffolds have also been investigated for potential bone loss applications, and they have demonstrated bactericidal efficacy and the ability to support cell proliferation and activity (Shafaghi *et al.*, 2021).

2.4.3 Phosphate-based Bioactive Glass Scaffolds

Like borate, phosphate glasses have gained attention as alternatives to silicate bioactive glasses due to their tailorable dissolution behavior and lower processing temperatures. Phosphate-based bioactive glass scaffolds are composed of phosphorus pentoxide (P_2O_5) along with other oxides such as sodium oxide (Na_2O) and calcium oxide (CaO) (Hyunh *et al.*, 2021). These scaffolds have shown excellent results in terms of architecture, composition, and functionality in recent study by Ruiz-Aguilar *et al.*, (2022), and have demonstrated bioactivity and osteoconductivity, forming hydroxyapatite (HA) crystalline aggregates with a cauliflower-like morphology in vitro studies (Ruiz-Aguilar, 2023). The incorporation of bioactive glass in biphasic calcium phosphate (BCP) scaffolds has also been investigated, resulting in improved physical properties, compressive strength, antibacterial activity, and in vitro bioactivity (Monmaturapoj *et al.*, 2022). Although phosphate glasses have advantages over silicate-based bioglasses, they have been reported to be inferior in facilitating cell attachment.

2.4.4 Comparison and Contrasting of Bioglasses

Silicate, borate, and phosphate-based bioactive glass scaffolds have several similarities and differences. Firstly, all three types of scaffolds exhibit bioactivity, promoting cell attachment and tissue regeneration. Secondly, they release bioactive ions such as silica, borate, and phosphate, which have specific effects on cell behavior and tissue growth. However, the release kinetics and ion concentrations differ among the different types of scaffolds, which can affect their biological performance(Al-Harbi *et al.*, 2021).

In terms of mechanical properties, silicate-based bioactive glass scaffolds are known for their higher mechanical strength compared to borate and phosphate-based scaffolds. This mechanical strength is essential for load-bearing applications such as bone tissue engineering. On the other hand, borate-based scaffolds have low melting temperatures, making them suitable for fabricating complex shapes and structures (Kaur *et al.*, 2014).

In terms of biocompatibility, all three types of scaffolds have been shown to be biocompatible and non-toxic. However, the specific biological responses may vary depending on the type of tissue and application. For example, silicate-based scaffolds have been reported to enhance angiogenesis, while borate-based scaffolds have shown antibacterial properties (Khurshid *et al.*, 2019). Furthermore, the degradation behavior of the different types of scaffolds varies. Silicate-based scaffolds degrade slowly, providing a long-term release of bioactive ions. Borate-based scaffolds degrade rapidly, making them suitable for temporary applications such as wound healing. Phosphate-based scaffolds degrade at an intermediate rate, allowing for controlled release of ions and subsequent bone regeneration (Ruiz-Aguilar *et al.*, 2022).

2.5 Drug Delivery Medical Applications of Porous Bioglass Scaffolds

BG scaffolds are captivating modern devices for their potential as controlled drug delivery systems and protein vaccines due to their ability to release therapeutic agents as depicted in Figure 2-4 adopted from Thananukul *et al.*, (2021), and promote an immune response, concurs various authors in their recent publications (Lee, Cho and Kim, 2022; Toosi *et al.*, 2022; Tulyaganov *et al.*, 2022).

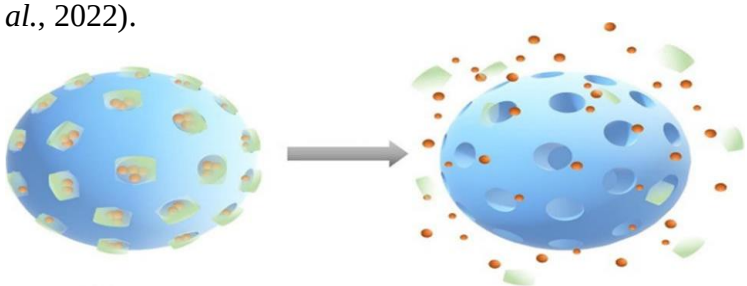

Figure 2-4: Porous Carrier for Drug Delivery Depicting 'Smart Gating' Biomolecule Releasing (Thananukul *et al., 2021)*.

A promising application of BG scaffolds is as protein vaccine delivery systems. Vaccines based on protein antigens are effective in preventing and treating infectious diseases, allergies, and cancers, but their delivery is often hindered by low stability and a short half-life. BG scaffolds have been shown to increase the stability and bioavailability of protein vaccines, promoting their sustained release and uptake by antigen-presenting cells (Lee, Cho and Kim, 2022). For instance, a recent study reported the use of mesoporous BG nanoparticles loaded with hepatitis B surface antigen (HBsAg) as a potential vaccine against the hepatitis B virus. The BG nanoparticles were found to enhance the immunogenicity and stability of HBsAg, leading to higher antibody titters and longer-lasting protection against the virus in mice (Toosi *et al.*, 2022).

BG scaffolds have also shown promise as controlled drug delivery systems for various therapeutic agents, including antibiotics, growth factors, and anticancer drugs. The porous structure of BG scaffolds allows for the loading and sustained release of drugs, while their bioactivity promotes tissue regeneration and wound healing (Leach *et al.*, 2006; Tulyaganov *et al.*, 2022; Che *et al.*, 2023). Another example is a recent study reporting the use of BG-collagen/poly (glycolic acid) scaffold nanoparticles loaded with vancomycin as a potential treatment for osteomyelitis. The BG nanoparticles were found to enhance the antibacterial activity and biocompatibility of vancomycin, leading to effective bone regeneration and eradication of bacteria in a rabbit model (Tulyaganov *et al.*, 2022). Furthermore, BG scaffolds have been investigated for their potential in combination therapies, where multiple therapeutic agents are delivered simultaneously or sequentially for synergistic effects. For instance, a recent study reported the fabrication of porous scaffolds containing collagen-poly glycolic acid blends and various quantities of BG, loaded with both insulin-like growth factor-1 and bone morphogenetic protein-2 for enhanced bone regeneration. The BG scaffolds were found to promote cell proliferation, differentiation, and mineralization,

leading to improved bone regeneration and mechanical properties in a rat model (Toosi *et al.*, 2022).

2.5.1 Commercial Viability of MBG Drug Delivery Systems

Numerous published experiments in Table summarize the performance of various forms of MBG particles, fibers, spheres, and scaffolds in their drug delivery potential of some commercial biomolecules (Wu, Chang and Xiao, 2011). In particular, MBGs can be used as a controlled drug release system for malignant tumors, making them a promising candidate for cancer therapy (Sharifi *et al.*, 2022). The high drug loading capacity and specific surface area of MBGs also allow for the sustained delivery of drugs and therapeutic ions, which can be released during material dissolution in contact with biological fluids (Migneco *et al.*, 2020b).

Table 2-2: Published Experiments of Various Forms of MBGs for Drug/Growth Factor Delivery and Bone Regeneration Application.

MBG	Composition	Biomolecule	Loading efficiency (%)	Delivery time (days)	Publication
Particles	58Si-36Ca-6P 80Si-15Ca-5P 80Si-15Ca-5P	Gentamicin Ibuprofen Ipriflavone	36-48 35 1-11	>10	Xia, W. et. al., 2008 Lopez-Noriega, et. al., 2010 Fan, Y. et. al., 2011
Discs	100Si 90Si-5Ca-5P 80Si-15Ca-5P	Tetracycline Metoclopramide Phenanthrene	10-18 15-45 5.15	>5	Zhao, L. et. al., 2008 Lin, H. M. et. al. 2010
Spheres	100Si 85Si-10Ca-5P	Triclosan Ibuprofen Bovine serum	9.1-10.7 20 4-16	>14	Arcos, D. et. al., 2009 Kang, X. et. al., 2011 Wu, C. et. al., 2010
Fibres	70Si-25Ca-5P	Gentamicin	5.5-14.4	>4	Hong, Y. et al., 2010
Scaffolds	80Si-15Ca-5P 80Si-15Ca-5P 80Si-15Ca-5P	Gentamicin Dexamethasone VEGF	11 16 90	>7	Zhu, Y. et. al., 2011

					Wu, C. et. al., 2011 Dai, C. et. al., 2012
Composites	80Si-15Ca-5P 80Si-15Ca-5P	Naproxen Dexamethasone	1.1 54	>10	Li, X. et. al., 2008 Zhu, M. et. al., 2011 Xia, W. et. al., 2008 Ramaswamy, Y. et. al., 2009 Chang, J. et. al. 2010

While the use of MBGs for drug delivery and bone tissue regeneration has shown significant promise, there are still some challenges to overcome before they can be widely commercialized. One major challenge is ensuring the reproducibility of MBG synthesis, which can impact their properties and performance (Guduric *et al.*, 2022). Additionally, the mesoporous channel structure and MBG composition can affect common cell evaluation assays, leading to inconclusive results (Guduric *et al.*, 2022). These factors must be considered carefully to ensure the reliability and reproducibility of MBGs for clinical applications. The burst release of drugs and poor compatibility with other materials have limited their applications. One effective way to overcome these challenges is to modify MBGs with a polymer brush. Polymer modification can improve the stability, biocompatibility, and drug-release properties of MBGs (Yao *et al.*, 2022). Similarly, ion-doped MBGs have been developed to enhance their therapeutic efficacy for biomedical applications (Arcos and Portolés, 2023).

Another challenge is the regulatory approval process, which can be lengthy and expensive. The use of MBGs for drug delivery and bone tissue regeneration falls under the category of medical devices, which are subject to strict regulations by regulatory agencies such as the US Food and Drug Administration (FDA) and the European Medicines Agency (EMA). The regulatory approval process can involve preclinical studies, clinical trials, and post-

marketing surveillance, which can take several years and require substantial financial resources (Wu and Chang, 2012).

2.6 Gaps in Literature

Previous studies on amorphous bioactive glass scaffolds have identified several limitations regarding their mechanical strengths. One key limitation is the brittleness of bioactive glasses, which hinders their widespread use in clinical practice (Fiume *et al.*, 2020). (Fu *et al.*, 2011) presents an opposing opinion, suggesting that mechanical strength may not be a limiting factor in the utilization of bioactive glass scaffolds for bone repair. This observation challenges the customary notion and invites further investigation into the parameters that influence the mechanical performance of these materials.

Contrastingly, (Kaur *et al.*, 2019) argue the inherent limitations of bioactive glasses and ceramics, specifically their low mechanical strength and fracture toughness, which present significant challenges for their use in load-bearing applications. This viewpoint is shared by (Jain *et al.*, 2022), who emphasize the critical importance of mechanical and in-vitro properties in the development of bioglass-based scaffolds for medical use.

Moreover, recent progresses in the field, as reviewed by (Kaou *et al.*, 2023), demonstrate the potential for overcoming these limitations through the development of diverse types of bioactive glasses, including silicate-, borate-, and phosphate-based compositions. Such innovations emphasize the active nature of research in this domain and the ongoing efforts to enhance the applicability of bioactive glasses in tissue engineering.

CHAPTER 3: METHODOLOGY

This chapter outlines the synthesis process of melt-derived bioactive glasses (BGs), utilizing a methodology like that of conventional soda-lime-silica glasses. The study prepares glass samples by melting, followed by scaffold formation through spark plasma sintering (SPS). The experimental setup includes a single muffle furnace for melting to produce glass ingot and frits. The study leverages SPS to explore sintering temperatures, heating rate, and holding time. Characterization of the synthesized glasses covers a range of techniques—thermal analysis, electron microscopy, and X-ray diffraction—to measure glass decomposition, thermal stability, particle size distribution, phase crystallization, density, pore interconnectivity, and mechanical strength. This investigation adopts a mixed-method approach, both quantitative and qualitative, to examine three distinct glass compositions: S53B50, P40B10, and Sr.

3.1 Research Materials

The starting analytical grade materials pictured in Appendix 3 (Fig. A-1) were mainly sourced from United Scientific (PTY) LTD, a trusted South African supplier of high-purity reagents and laboratory ware. A list of all chemical reagents supplied for this study is presented in Table 3-1.

Table 3-1: High Purity Synthesis Chemical Reactants.

Item Code	Item Description	Chemical Formula	Analytical Grade
CHEM615-20	Sodium Carbonate Anhydrous 500 g	Na_2CO_3	99.9%
CHEM045-00	Boric Acid 500 g	H_3BO_3	99.5%
S2329NN0050	Silica Fine Powder CP 500 g	SiO_2	98.5%
S2485NN0050	Sodium Hexametaphosphate CP 500 g	$NaPO_3$	85.0%
S2705NN0050	Strontium Carbonate CP 500 g	$SrCO_3$	97.0%
CHEM068-02	Calcium Carbonate 500 g	$CaCO_3$	99.9%

CHEM010-12	Ammonium Di-hydrogen Orthophosphate 500 g	$(NH_4)_2HPO_4$	98.0%
P1945TC00500	Phosphorous Pentoxide 500 g	P_2O_5	99.5%
CHEM615-25	Sodium Chloride 500 g	NaCl	99.5%
CHEM615-13	Sodium Bicarbonate 500 g	$NaHCO_3$	99.5%
CHEM515-25	Potassium Chloride 500 g	KCl	99.5%
T248-2	Hydrochloric Acid 1.00 N (1.00 M) 500 ml	HCl	1.0 M
CHEM405-08	Magnesium Chloride 500 g	$MgCl_2$	99.0%
C0439NN0050	Calcium Chloride $2H_2O$ Cristals Dihydrate AR 500 g	$CaCl_2.2H_2O$	98.0%
CHEM615-65	Sodium Sulphate 500 g	Na_2SO_4	99.0%
T1503B	Tris(hydroxymethyl)ami9nomethane AR 500 g	$NH_2C(CH_2OH)_3$	-

In addition to the reagents the experiments further utilized other consumables and laboratory ware all described with their respective functions in Table 3-2 below.

Table 3-2: Experimental Consumables and Laboratory Ware.

Consumable	Function
150 ml Plastic screw-lid bottles	Powder handling for dry mixing and storing.
Ceramic Melting Crucible	Melting in a furnace at high temperature.
Graphite paper	Prevent melts from fusing with crucible wall.
⌀ 20mm Graphite die and punch	Sintering punches and die and serve as electrodes.
Acetone/Ethanol	Cleaning of lab ware to minimize contamination.
Deionized water	Ultrasonic bath medium for salt leaching.

3.2 Reagents Batch Preparation

A targeted blend of borosilicate bioactive glass S53B50 which is made up of 26.93% SiO_2, 26.93% B_2O_3, 21.77% CaO, 22.66% Na_2O, and 1.72% P_2O_5 in mole percentages was synthesized by combining SiO_2, Na_2CO_3, H_3BO_3, $CaCO_3$, and $NaPO_3$ starting reagents.

Similarly, a borophosphate glass P40B10 ($40P_2O_5$-20SrO-20CaO-$10B_2O_3$-$10Na_2O$) and the phosphate glass Sr ($50P_2O_5$-40SrO-$10Na_2O$) were prepared as well from $NaPO_3$, H_3BO_3, $SrCO_3$, $CaCO_3$, P_2O_5 and $(NH_4)_2HPO_4$ analytical reagents. The synthesis process; started with precisely measuring with a micro balance scale in Figure 3-1 and combining the appropriate quantities of initial reagents in accordance with calculated blending mass ratios from converting the targeted molar ratios as follows:

a. Determined the molar ratios of the different components in the desired composition.
b. Calculated the mass ratios of the reagents by multiplying the molar ratios of each component by their respective molar masses.
c. Used the starting reagents to write the balanced chemical reactions below, predicting the decomposition reactions that produce each component.
d. Multiplied stoichiometric coefficients of the reactants with the molar masses and dividing it by the molar masses of the products formed in the reaction will yield a decomposition factor.
e. Assumed the production of a 100 g specimen and multiply the desired mass fraction of each component by the respective decomposition factor to find the reactants required mass fraction for a 100 g batch.

Chemical reactions for S53B50, P40B10 and Sr glasses predicting the formation of each component of the final composition follow a decomposition nature as described below. However, SiO_2 and P_2O_5 were introduced as pure compounds whilst $Ca_3(PO_4)_2$ and $Sr_3(PO_4)_2$ precursors were formed first using $(NH_4)_2HPO_4$ in a decomposition reaction with the respective $CaCO_3$ and $SrCO_3$ carbonates.

S53B50 - $26.93SiO_2$-$22.66Na_2O$-21.77CaO-$26.93B_2O_3$-$1.72P_2O_5$ (mol. %):

- $Na_2CO_3 \rightarrow Na_2O + CO_2$
- $2H_3BO_3 \rightarrow B_2O_3 + 3H_2O$

- $2CaHPO_4 \cdot 2H_2O \rightarrow 2CaO + P_2O_5 + 5H_2O$
- $CaCO_3 \rightarrow CaO + CO_2$

P40B10 - $40P_2O_5$-20SrO-20CaO-$10B_2O_3$-$10Na_2O$ (mol. %) and **Sr** - $50P_2O_5$-40SrO-$10Na_2O$ (mol. %):

- $2(NH_4)_2HPO_4 + 3CaCO_3 \rightarrow Ca_3(PO_4)_2 + 4NH_3 + 3CO_2 + 3H_2O$
- $2(NH_4)_2HPO_4 + 3SrCO_3 \rightarrow Sr_3(PO_4)_2 + 4NH_3 + 3CO_2 + 3H_2O$
- $2Ca_3(PO_4)_2 \rightarrow 6CaO + 4P + 5O_2$
- $2Sr_3(PO_4)_2 \rightarrow 6SrO + 4P + 5O_2$
- $2NaPO_3 \rightarrow Na_2O + P_2O_5$
- $2H_3BO_3 \rightarrow B_2O_3 + 3H_2O$

Handling fine powders during batching pictured in Appendix 3 (Fig A-2) required diligent caution to avoid contamination and maintain personal safety by using sterile lab-ware, goggles, gloves, and a lab coat to avoid direct contact with reagents. Furthermore, the batch size was reduced to $2/3$ of the 100 g batches for appropriate mixing in plastic bottle sample containers.

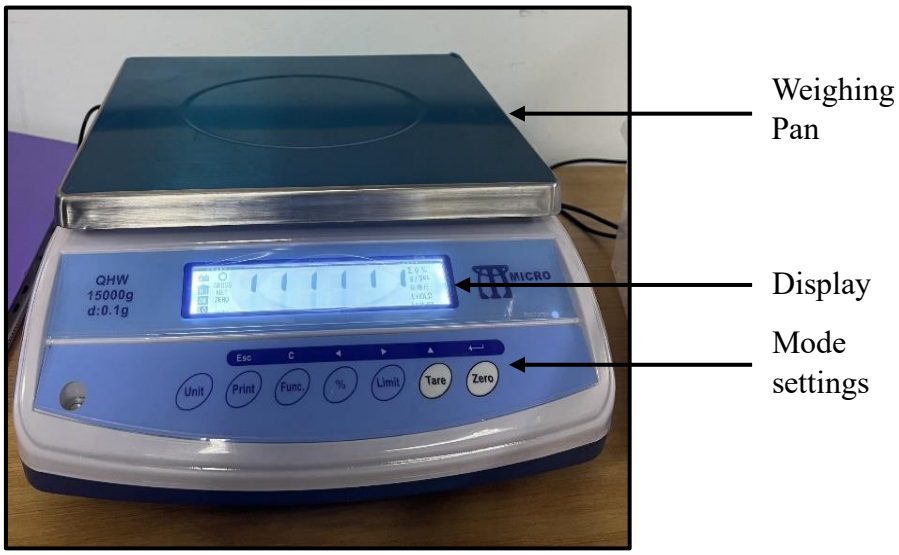

Figure 3-1: Micro QHW-15 Top Pan Balance Scale.

A Tabular T2F mixer in Figure 3-2 was used to mix the batches for 2 hours at 100 rpm to achieve homogeneity in containers pictured in Appendix 3 (Fig. A-3) for dry mixing. The mixed powders were then labelled as blend A, blend B and blend C for S53B50, Sr and P40B10 targets respectively. 1-gram samples were measured from each blend and subjected to thermogravimetric analysis.

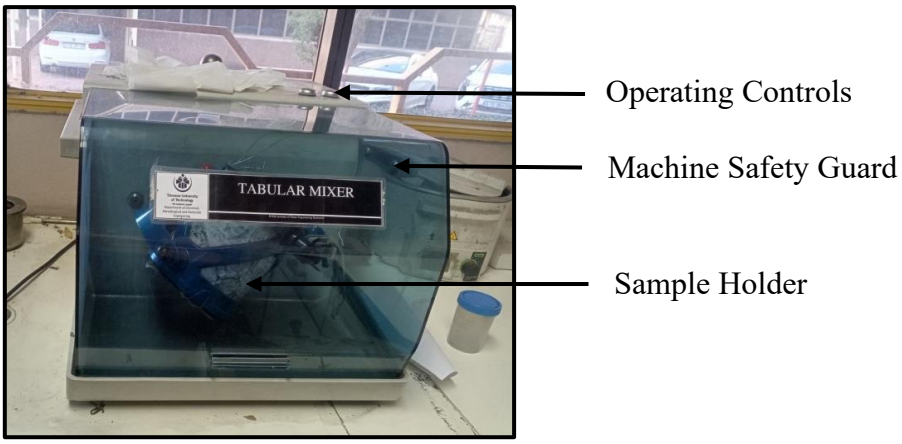

Figure 3-2: T2F System Schatz Tabular Mixer.

Thermal Gravimetric Analysis (TGA) was executed on the starting powder blends, through a gradual increase in temperature of a specimen in a TGA 4000 furnace see Figure 3-3, while its weight is gauged on an analytical balance that remains external to the furnace. TGA detects a decline in mass if a thermal incident involves the loss of a volatile component.

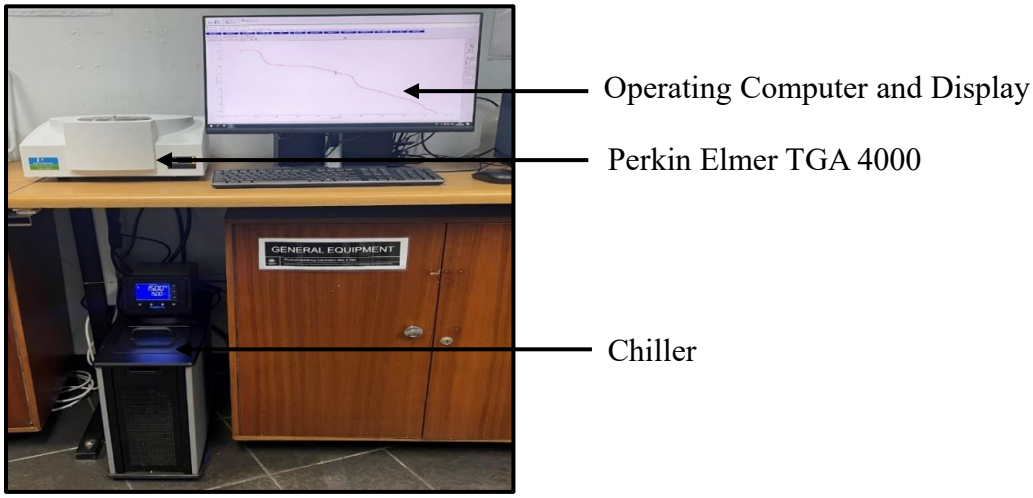

Figure 3-3: Perkin Elmer Thermogravimetric Analyzer 4000.

The sample weight is then plotted against temperature or time to elucidate the thermal stability of the material, including but not limited to the loss of solvent and plasticizers in

polymers, the water of hydration in inorganic materials, and, lastly, the decomposition of the material.

3.3 Melting and Annealing

A muffle furnace pictured in Appendix 4 (Fig A-4) was used to synthesize both borosilicate and phosphate glasses by melting at 1200 ^{o}C and 1100 ^{o}C respectively. The different batches of raw materials were subjected to a comparative experimental study via melt-cast-annealing and melt-quenching methods to investigate the effects on the material's crystalline structure and properties. The methodology commences with both samples undergoing an identical melting phase, where the materials were heated to their melting points, and maintained at this soak temperature for 1 hour to ensure a homogenous melt was achieved. During melting the S53B50 composition was held at 800 ^{o}C whilst the P40B10 and Sr compositions were held at 600 ^{o}C for 1 hour, this was to allow for complete decomposition deduced from the TGA thermal stability observations. The average heating rate for the muffle furnace was below 15 ^{o}C/min and the maximum operating thermostat temperature is 1200 ^{o}C, therefore the muffle did not at any point overshoot past targeted temperatures.

In the melt-cast-annealing approach, the molten glass was cooled within the furnace to below 800 °C, then the crucible containing a monolithic glass ingot was removed and air cooled to room temperature. All the glass ingots were then annealed at the same time by slowly heating them in the furnace from ambience to 470 ^{o}C over a 12-hour interval. Subsequently, ingots were slowly cooled in furnace to below 50 ^{o}C by simply switching off, facilitating the release of internal stresses, and preventing crack formation. This annealing process is crucial in developing a stable glass structure with uniform properties. The dry glass monoliths pictured in Appendix 4 (Fig A-7) were measured for bulk density by submerging them in deionized water using a 500ml measuring cylinder. Three readings were observed at different initial volumes to minimize meniscus levelling parallax errors. Conversely, the melt-quenching

technique diverges at the post-melt phase, wherein the molten glass was rapidly quenched, by immersion in deionized water, causing a sharp temperature-drop to ambient conditions within minutes from the high melting temperatures. This abrupt thermal transition inhibits crystalline growth, yielding amorphous frits pictured in Appendix 4 (Figs. A-5 and A-6) that were dried overnight in an oven at 90 °C. All melts were performed in ceramic mantle

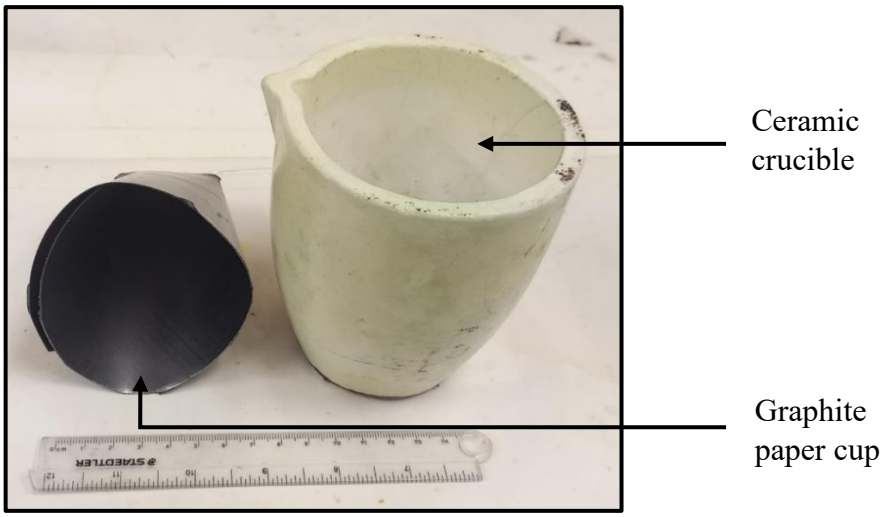

Figure 3-4: Ceramic Crucible and Folded Graphite Paper Cup used for Material Handling During Melting.

crucibles using graphite paper folded cups shown in Figure 3-4. This was critical in avoiding contamination of the melts, preventing glass ingots from fusing to crucibles and then also allowing for viscous melt pouring into water to quench.

3.4 Milling

Glasses were crushed to reduce size to an appropriate mill charge size of less than 2mm particles pictured in Appendix 5 (Fig. A-8) with a porcelain ceramic mortar and pestle. A Retsch PM 100-CM planetary ball mill in Figure 3-5 was used to dry grind melt produced glasses to powder. Glass ingots labelled melt A (S53B50), melt B (P40B10) and melt C (Sr) were ground separately using a zirconium (ZrO_2) lined jar and a steel ball of mass 396 g pictured in Appendix 5 (Fig. A-9) at 350 rpm for 1 hour. Also, frits labelled melt 1 (S53B50), melt 2 (P40B10) and melt 3 (Sr) were ground using the same equipment and settings. The mill was set to reverse rotation in 15-minute intervals with a 5-minute break time.

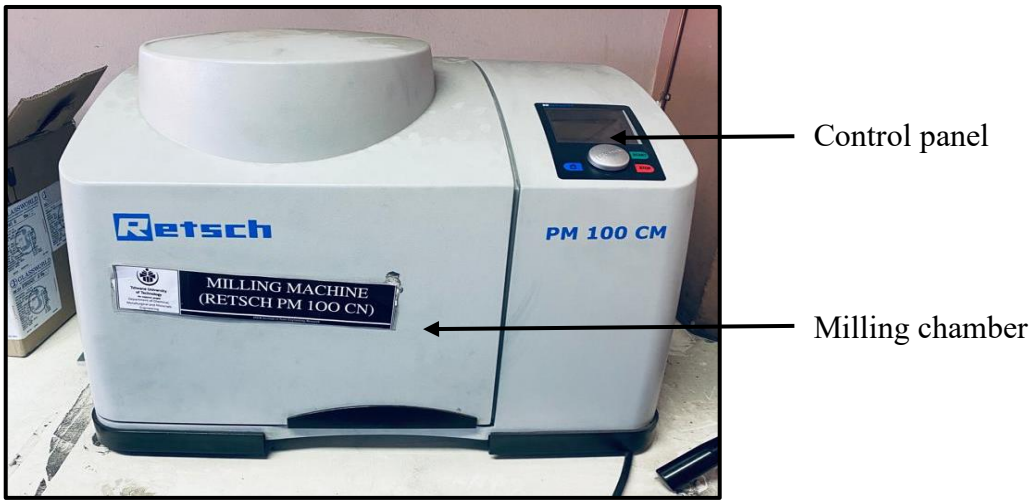

Figure 3-5: Retsch PM 100-CM Planetary Ball Mill.

The milled powders were than characterized for particle size distributions using a Malvern Panalytical Mastersizer 2000E within the range 0.1 – 1000 µm. By analyzing the particle size distribution, it was possible to further determine the average particle size, the range of particle sizes, and the cumulative distribution. This is essential for optimizing powder compaction and sintering, where the particle size distribution can affect the final product's quality and performance. The resulting powders were labelled powder A, B and C for the normalized melt-cast-annealed material; powders 1, 2 and 3 for the melt-quenched material, Additionally, NaCl powder granules were also milled for 2 hours to get fine powders used as a space holding pore generator during sintering production of porous scaffolds.

3.5 Porous Scaffold Fabrication

Fine sodium chloride was selected as a sacrificial porogen after a test using 50 vol. % of PVA failed during rapid sintering. The PVA seemed to react with glass powder at elevated temperatures and broke the punches during heating and therefore sintering could not be achieved. A tabular was used again to mix 15 g of NaCl with 22.70 g of powder A, 25.02 g of powder B and 21.46 g of powder C using 10 steel balls for 3 hours. The final sintered pellet was designed to have a height of 3.5mm and a total volume of 1.099 cm^3. Using 2.17 g/cm^3 density of NaCl; 60 vol. % porogen blends were prepared for scaffold forming using a type KCE®FCT H-HP hybrid furnace with a 2200 °C maximum sintering temperature capacity in Figure 3-6. Measurements of ±4 g were used for sintering each scaffold by SPS, 20 mm diameter sintered specimen are pictured in Appendix 6 Figures A-11 and A-20.

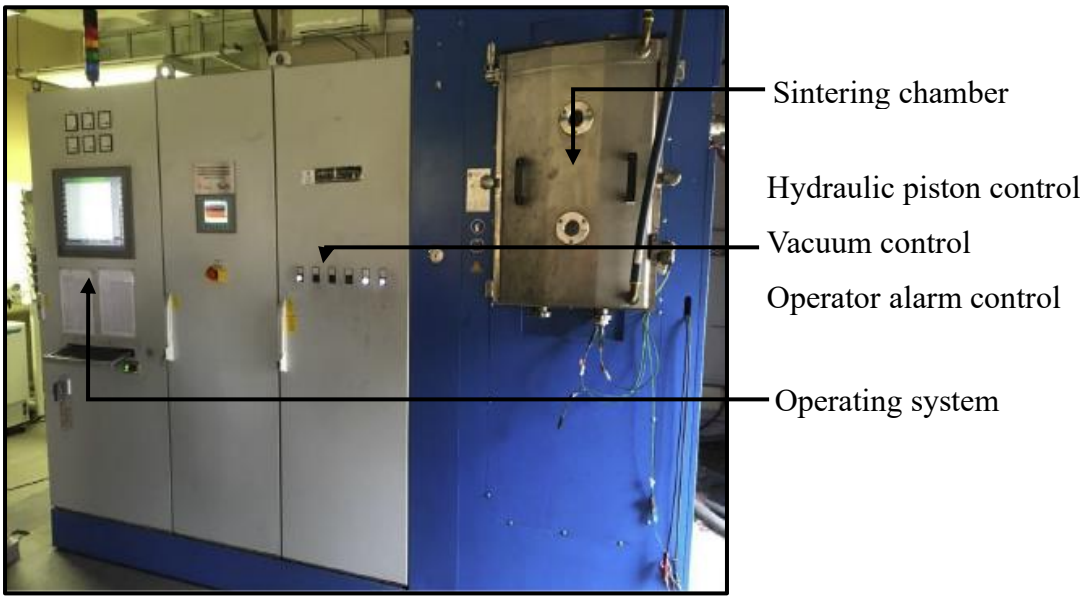

Figure 3-6: SPS KCE®FCT H-HP Hybrid Sintering Furnace.

SPS is a novel technique which offers a significant advantage in terms of a remarkably short processing time. This method typically involves four main stages, namely gas removal and vacuuming, pressure application, resistance heating, and the cooling phase. Compared to traditional sintering techniques, which may take several hours or even days to achieve similar results, Spark Plasma Sintering can accomplish the same task within a few minutes. This

remarkable sintering rate is achievable in SPS due to the high heating rates that can be readily achieved through internal heating of the sample, unlike external heating in the case of conventional sintering methods. The compositions synthesized in this work are characterized by Erasmus *et al.*, (2017) in a previous study and a differential thermal analysis yielded thermal characteristics adopted in Table 3-3. This work provided important benchmarks for sintering temperatures below the onset of crystallization characterised for the S53B50, P40B10 and Sr powders.

Table 3-3: Glasses S53B50, P40B10 and Sr Thermal Properties and Sintering Work Range Temperature Characteristics.

Characteristic temperature (^{o}C)	S53B50	P40B10	Sr
Glass transition temperature (T_g, ±2 ^{o}C)	510	509	436
Onset of crystallization temperature (T_x, ±2 ^{o}C)	672	633	540
Working range ($\Delta T = T_x - T_g$, ±4 ^{o}C)	162	124	104

The holding time at pyrolysis temperatures was selected to be 10 minutes for SPS, whereas a heating rate of 100 °C/min was used for all sintered samples. Hot working ranges for the different composition were divided to 4-quantiles, so the second and third quartiles were selected as pyrolysis temperatures. Parameters used for sintering powders to solid scaffold in Table 3-4, and 3 samples were produced for each scaffold composition.

Table 3-4: Spark Plasma Sintering Parameters.

Scaffolds	Hold Time (min)	Heating Rate (°C/min)	Temp. (°C)
S53B50	10	100	590
			610
P40B10	10	100	570
			600
Sr	10	100	490
			520

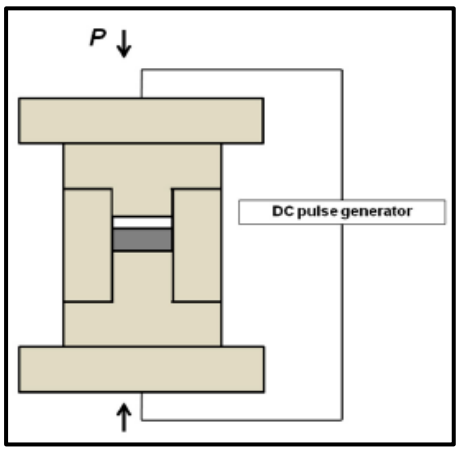

Figure 3-7: Pressure-less SPS.

Furthermore, to observe maximum porosity pressure less sintering punch and die arrangement was used as depicted in Figure 3-7 above. Unlike traditional SPS, which uses pressure to consolidate powder materials, pressure-less SPS does not apply any mechanical force during sintering. This approach is particularly beneficial because the goal is to achieve high porosity of the material, and it avoids the compaction and shrinkage that usually occurs under pressure. In this context, the use of a pressure-less SPS punch and die arrangement, specifically 20 mm diameter graphite dies, was important. The size of the die determines the size of the sample that can be processed. The 20 mm dies used are suitable for creating moderately sized samples while maintaining uniformity in heating and sintering process. Additionally, lining the die with graphite paper is a crucial step in SPS. Graphite paper serves multiple purposes by acting as a release agent, facilitating the easy removal of the sintered material from the die, and it can also help in uniformly distributing the electric current and heat during the sintering process. This is especially important in SPS, where electric current and heat are critical factors in achieving the desired material properties.

3.5.1 Sacrificial Salt Porogen Leaching

Salt porogen leaching is a technique prominently used in the field of tissue engineering for the fabrication of porous implants, particularly bioglass scaffolds. The use of NaCl as a porogen in this process is favourable due to its solubility, availability, and non-toxicity, making it a suitable choice for creating biocompatible scaffolds. After the scaffold are sintered, they undergo a leaching process using an ultrasonic temperature-controlled cleaner in Figure 3-8. Sintered compacts are immersed in deionized water that is

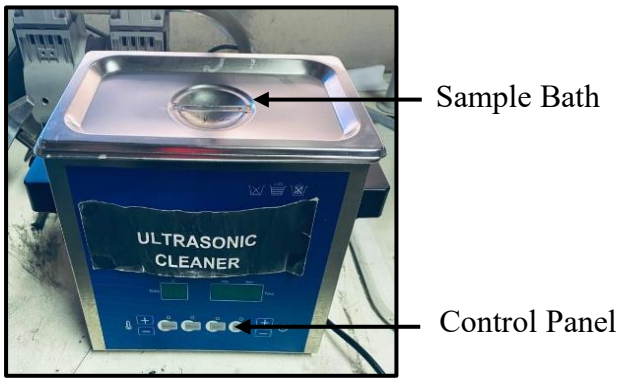

Figure 3-8: An Ultrasonic Cleaner.

heated to 80 °C and degassing for 1 hour. During this stage, the NaCl particles dissolve and are washed away, leaving behind a network of interconnected pores. The final product is a scaffold with a porous structure, where the size and connectivity of the pore are controlled by the size of the NaCl particles used as the porogen.

3.5.2 Scaffold Cutting

The cutting operation of scaffolds to reveal their cross-section for characterization, was done using a Chennai Metco Baincut Low-Speed Saw (Baincut LSS) equipped with a diamond cutting disc shown in Figure 3-9. The use of a Baincut LSS, is crucial for precision cutting of delicate materials like ceramic glass scaffolds. Low-speed sawing reduces the risk of inducing thermal damage or altering the microstructure of the material during cutting. The use of a diamond cutting disc enhances the cutting efficiency and precision. Diamond discs are known for their hardness and durability, making them ideal for cutting through a variety of materials, including the very brittle glass-ceramics.

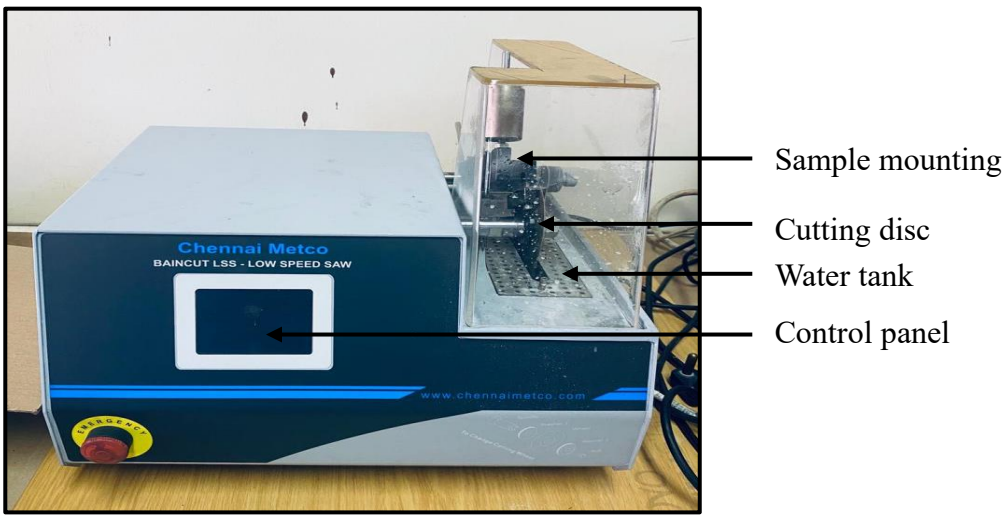

Figure 3-9: Chennai Metco Baincut Low-Speed Saw.

Proper handling and fixation of the scaffold specimen is essential to ensure accurate cuts. The equipment includes mechanisms and fixtures to securely hold the scaffold in place during cutting, reducing the risk of displacement or damage. This allows for precise control

over the cutting process, ensuring that the integrity of the scaffold's cross-section is maintained for accurate characterization.

3.6 Characterization of Powders and Scaffolds

3.6.1 Powder Particle Size Distribution

The methodology for Particle size distribution (PSD) analysis of the six powders each with a sample size of 1-3 g was done utilizing the Mastersizer 2000 laser diffraction particle size analyzer. Initially, each powder sample, normalized from a melt (A, B and C) or quenched to frits from a melt (1, 2 and 3), was carefully prepared. Given their small sample sizes, consistent and homogenous dispersion was crucial to avoid particle agglomeration, which could skew results. Once prepared, the samples were loaded into the mastersizer analyzer. The analyzer then captured scattering data, processed by its software to compute a detailed particle size distribution profile for each sample. This profile provided both graphical and numerical representations of the distribution, offering an in-depth understanding of the particle size characteristics of each powder.

3.6.2 Thermal Gravimetric Analysis

A TGA 4000 instrument was utilized to conduct analysis on four samples obtained from powders A to C, in addition to a control sample of Zeolite bioglass powder. During this process, the temperature of each sample was incrementally increased in a furnace, while its weight was measured using an analytical balance situated externally to the furnace. During the TGA analysis, any reduction in mass was observed when a thermal event resulted in the loss of a volatile component. Chemical reactions, such as combustion, led to mass losses, whereas physical changes, such as melting, did not. The weight of each sample was graphed against temperature to depict thermal transitions in the material, such as the dissipation of solvents and plasticizers in polymers, the removal of water of hydration in inorganic materials, and ultimately, the decomposition of the material.

3.6.3 Powder Fourier Transform Infrared Spectroscopy

0.5g powder samples of powders A, B and C were scanned for bond energy vibrations. The examination of ceramic glass powders was conducted through the application of FTIR spectroscopy. To perform this task, a Bruker spectrophotometer was utilized with a scanning range of 500-4500 cm^{-1}. The outcomes of this technique allowed for the acquisition of significant information regarding the distinct chemical bonds that exist within the analysed samples. Consequently, the findings of this investigation contribute significantly to the understanding of the chemical properties of ceramic glass powders (Lara-Ochoa, Ortega-Lara and Guerrero-Beltrán, 2021).

3.6.4 X-Ray Diffraction Analysis

In the study, X-ray Diffraction (XRD) analysis was specifically applied to characterize powder samples and solid scaffolds. Powder samples were prepared as pictured in Appendix 5 (Fig. A-10) and analyzed, including three normalized from a melt labelled A, B, & C and three quenched to frits from a melt labelled 1, 2, & 3. These samples were examined alongside a control sample of Zeolite bioglass powder. XRD diffraction analysis was carried out on the surface of specimen using a PANalytical Empyrean diffractometer in Figure 3-10. The analysis offers valuable insight into the structural properties and composition of materials because, XRD is a widely used technique in the field of material science for determining the crystal structure and phases present in each sample. The diffractometer employed monochromatic Cu Kα radiation under a tension of 40 kV and 45 mA. The purpose of the XRD analysis was to identify the crystal peaks and determine the phases present in both the powders and the sintered scaffold specimen. During the diffraction, a scanning step mode of 0.02 was utilized. The diffractions were collected over a 2Θ range between 5^{o} to 90^{o} at room temperature.

Furthermore, six solid scaffold samples were analysed using XRD. These samples comprised scaffolds from S53B50 composition sintered at temperatures of 590 and 610 °C, P40B10 sintered at 570 and 600 °C, and Sr sintered at 490 and 520 °C.

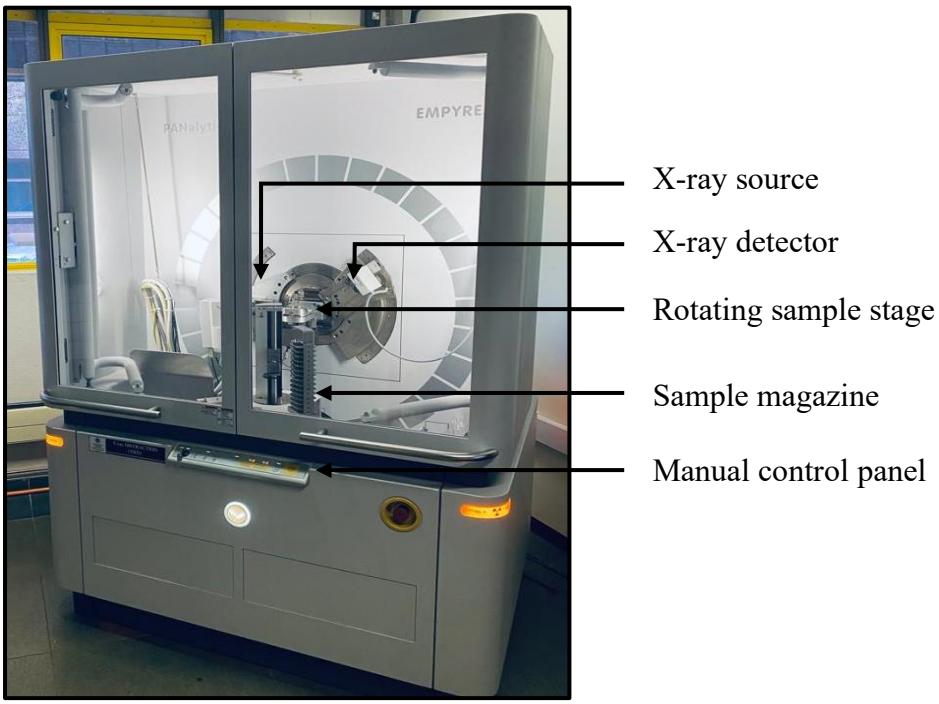

Figure 3-10: A PANalytical Empyrean X-rays Diffractometer.

The identification of phase components was performed using X'pert High Score Plus software, a commonly used tool for the analysis and interpretation of diffraction peaks. The analysis focused on understanding the phase transformations and crystalline structure development at different sintering temperatures. The XRD technique was pivotal in identifying the crystal peaks and determining the phases present in these sintered samples. Through this approach, detailed insights were gained into the microstructural evolution of the materials, from powdered form to sintered scaffolds, thereby enhancing the understanding of their mechanical and biological properties.

3.6.5 Microscopy and Surface Analysis

Scanning Electron Microscopy (SEM) and Energy Dispersive X-ray Spectroscopy (EDS) played a crucial role. The SEM analysis, conducted using a JEOL JSM-7900F SEM in Figure 3-11, afforded high-resolution images that revealed the surface morphology of the samples.

Coupled with the SEM, the Tru-Q powered EDS system enabled the determination of the elemental composition of the samples. This analysis was particularly important for confirming the presence of specific elements in the powder samples and for understanding the elemental distribution within the sintered scaffolds.

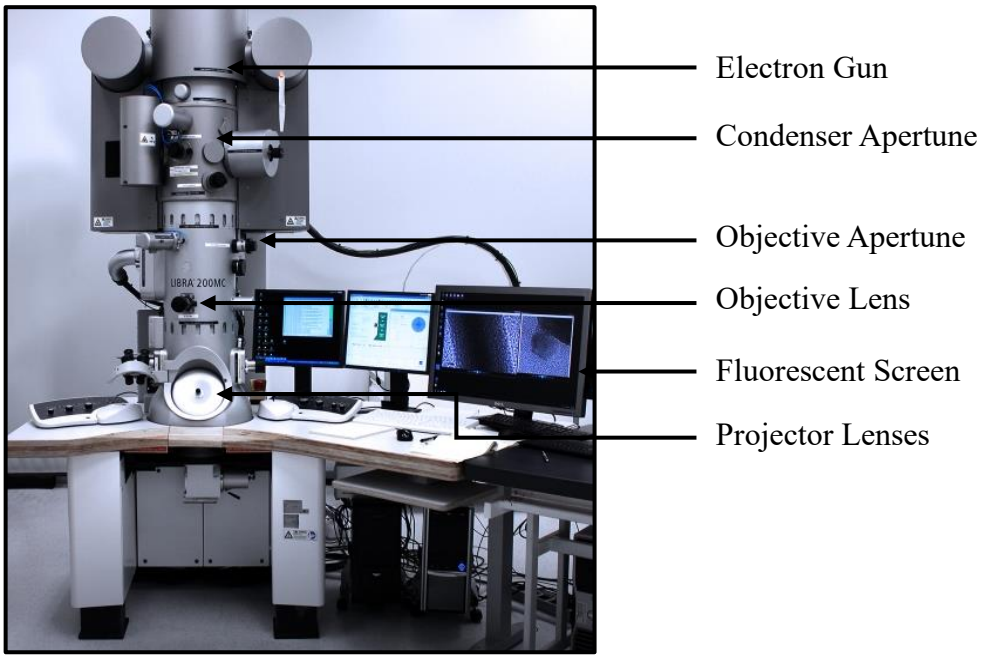

Figure 3-11: A JEOL JSM-7900F Scanning Electron Microscope.

For the solid scaffolds, the focus was on quantifying the porosity, which is a critical parameter for assessing the quality and potential applications of sintered materials. Microscopic images of the porous surfaces were obtained at low magnification. These images were then analyzed using FIJI ImageJ, an open-access software. ImageJ provided a platform for accurate and quantitative analysis of the porosity by allowing measurements of pore sizes and distribution across the scaffold surfaces. The combined use of these analytical techniques provided a multifaceted understanding of the materials under study. It bridged the gap between the microstructural and crystallographic perspectives, offering a comprehensive view of the samples' properties.

3.6.6 Compression Load Bearing Analysis

Four samples being S53B50 no porogen, Sr sintered at 520°C, P40B10 at 600°C, and S53B50 at 610°C were analyzed at the Council of Scientific and Industrial Research (CSIR), Mechanical Testing Facility. The Instron Model 1342 machine in Figure 3-12, equipped with Tungsten Carbide Presses, was utilized, ensuring high precision and consistency in the testing process. Each specimen was prepared with specific dimensions: diameters ranging from 19.92 to 20.37 mm and anvil heights between 10.60 and 11.00 mm, to maintain uniformity across tests.

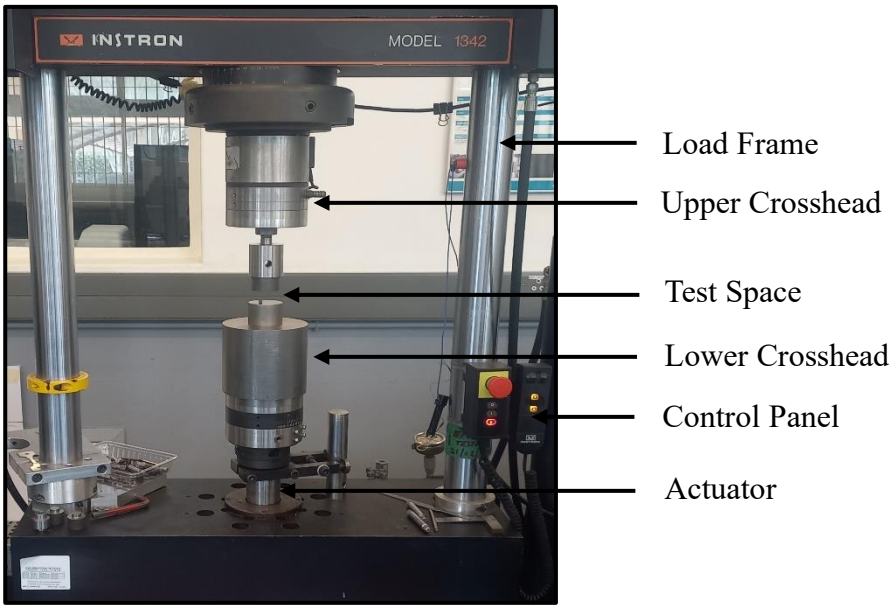

Figure 3-12: A Instron Model 1342 Compression Testing Machine.

The tests were conducted under controlled conditions, with a consistent room temperature of 21.00°C and a loading rate of 0.50 mm/min. Throughout the testing process, the samples were subjected to increasing compressive forces until failure. The data collected included the maximum load-bearing capacity, deformation patterns, and the point of fracture. These data points were crucial in determining the compressive strength, stiffness, and overall structural integrity of the bioglass scaffolds.

3.6.7 Tribology Wear Analysis

The wear analysis of sintered porous scaffolds was done at the Surface Engineering Research Laboratory (SERL), with an Anton Paar TRB3 Tribometer (version 8.1.8). Samples of Sr, P40B10, and S53B50 were tested under two different loads, 3N and 5N, for a duration of 10 minutes each. The tribometer's parameters included a single-way mode, a linear speed of 0.03 cm/s, and an acquisition rate of 15.0 Hz. The focus of the research was to understand the wear mechanisms and properties of these bioactive glasses when subjected to varying loads. This was crucial for assessing their potential applications in biomedical fields, where material endurance and reliability are paramount.

The wear rate calculations were based on measurements of the worn track section and load, with the wear rates expressed in $mm^3/N/m$. Tests were conducted under laboratory conditions with temperatures around 28 °C, target temperature at 24°C, atmospheric pressure approximately 101.4 Pa, and humidity ranging from 42-45%. This setup provides valuable data on the wear characteristics of the glasses at different sintering temperatures and under varying mechanical stresses. By analyzing the wear patterns and rates at these loads, one could infer the materials' suitability for various biomedical applications, including their durability and long-term performance in the human body.

CHAPTER 4: RESULTS

This chapter carefully presents the findings of the research study. It begins with the batch preparation of reagents, followed by analyzing their thermal decomposition. It then details the batch melting process, including assessments of bulk density. It proceeds with the preparation of glass-ceramic powders and their analysis through X-ray powder diffraction, FTIR spectroscopy, SEM and EDS. Further, it elaborates on the fabrication of scaffolds via Spark Plasma Sintering, examining their phase identification and crystallization through X-ray diffraction. Lastly, the chapter evaluates the porosity and mechanical properties of the scaffolds, including compression load-bearing tests and tribology wear analysis.

4.1 Batch Preparation of Reagents

In the study, three different bioactive glass batches were prepared, each with distinct compositions: Borosilicate (S53B50), Borophosphate (P40B10), and Phosphate (Sr). For each glass type, the percentage of each oxide by molar mass (mol.%) and the corresponding mass factions were calculated in Table 4-1.

Table 4-1: Batch Preparation of S53B50, P40B10, and Sr Bioactive Glass Reagent Mass Fractions, and Actual Masses used in Two Trials.

Borosilicate (S53B50)						
Oxide	**mol.%**	**Mass Fraction**	**Reagent**	**100g Batch +5% loss (g)**	**Mass Trial 1 (g)**	**Mass Trial 2 (g)**
SiO_2	26.93	0.254	SiO_2	26.7	17.8	18.1
B_2O_3	26.93	0.295	H_3BO_3	55.0	36.7	36.0
Na_2O	22.66	0.221	Na_2CO_3	39.6	26.4	25.9
CaO	21.77	0.192	$CaCO_3$	28.4	18.9	19.3
P_2O_5	1.72	0.038	P_2O_5	4.1	2.7	2.8
Total	100.01	1.000		153.8	102.5	102.1

Borophosphate (P40B10)						
Oxide	**mol.%**	**Mass Fraction**	**Reagent**	**100g Batch +5% loss (g)**	**Mass Trail 1 (g)**	**Mass Trail 2 (g)**
P_2O_5	40.00	0.557	P_2O_5	58.5	39.0	39.5
SrO	20.00	0.203	$SrCO_3$	28.9	19.3	18.9
CaO	20.00	0.110	$CaCO_3$	19.8	13.2	13.0
B_2O_3	10.00	0.068	H_3BO_3	12.7	8.5	8.7
Na_2O	10.00	0.061	$NaPO_3$	21.0	14.0	14.3
Total	100.00	1.000		140.9	93.9	94.4
Phosphate (Sr)						
Oxide	**mol.%**	**Mass Fraction**	**Reagent**	**100g Batch +5% loss (g)**	**Mass Trail 1 (g)**	**Mass Trail 2 (g)**
P_2O_5	50.00	0.598	P_2O_5	62.8	41.9	41.4
SrO	40.00	0.349	$SrCO_3$	53.4	35.6	35.1
Na_2O	10.00	0.053	$NaPO_3$	18.1	12.1	12.3
Total	100.00	1.000		134.3	89.5	88.8

For the S53B50 batch, the mass of reagents needed for a 100g batch, considering a 5% loss were measured. The actual masses used in two trials were reduced by $\frac{1}{3}$, revealing slight variations to loosely fit powders in containers for homogenous mixing, but maintaining mass fractions for all components. Silicon dioxide (SiO_2) and boron oxide (B_2O_3) had the highest mol.% at 26.93 each, while phosphorus pentoxide (P_2O_5) had the lowest at 1.72 mol.%.

The P40B10 batch has P_2O_5 having the highest mol.% at 40.00, with the subsequent trials demonstrating a consistent mass measurement across the two trials for each reagent. Lastly, in the Sr batch, P_2O_5 and strontium oxide (SrO) were the primary components, with 50.00 mol.% and 40.00 mol.%, respectively. The trials for this batch also indicated a small discrepancy between the two trials' mass measurements.

4.2 Thermal Decomposition of Reagents

TGA performed on the starting reactants powder blends of revealed distinct thermal stability and decomposition characteristics for each sample presented in Figure 4-1. A comparative Zeolite bioglass powder was also analyzed as a control sample for glass synthesis.

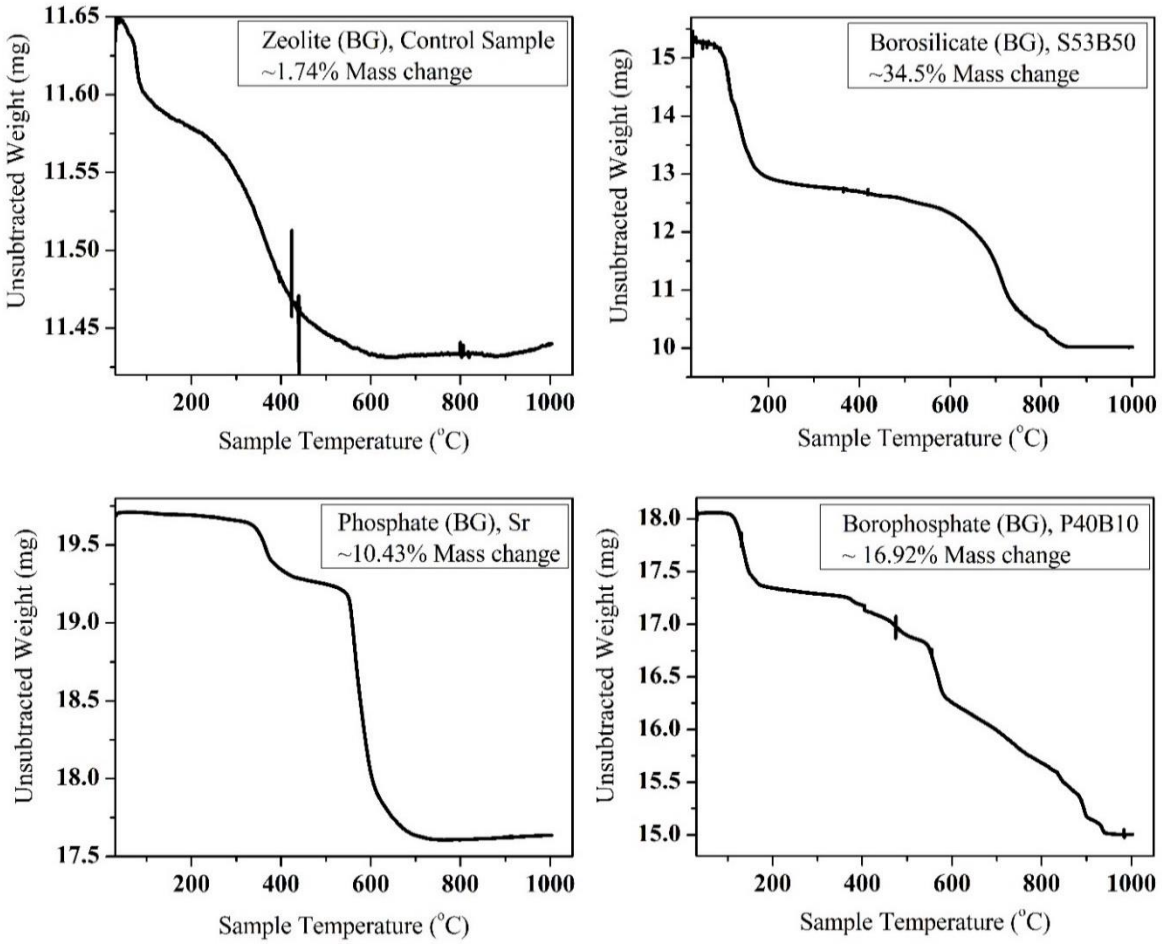

Figure 4-1: TGA of Zeolite (control), S53B50, Sr and P40B10 Powders Graphically Displaying the Mass Change as a Function of Temperature.

The Zeolite bioglass control sample had a small mass loss of 1.74% and remained stable from 600°C. The S53B50 sample had a large mass loss of 34.5% and showed major thermal events from 600°C to 900°C. Sr glass sample had a mass loss of 10.43% and showed decomposition or structural changes between 300°C and 700°C. The Borophosphate P40B10 sample had a mass loss of 16.92% and underwent major thermal decomposition from 300°C to 700°C.

4.3 Batch Melting

The process of melting the glass blends, namely S53B50 (Blend A), P40B10 (Blend B), and Sr (Blend C), involved a series of temperature increments starting from the ambient temperature presented in Table 4-2. In the case of Blend A, the temperature set points of the furnace gradually increased to 1200°C in specific intervals, with a final soaking of 1 hour. Temperature points designated longer intervals time up to 800°C for complete decomposition, which could reach up to 5 hours and 15 minutes at the final stage. P40B10 and Sr melting followed a similar procedure to Blend A, however, the maximum soaking temperature was at 1100°C.

Table 4-2: Temperature Progression Profile for Batched Glass Blends S53B50 and Sr and P40B10 during Furnace Melting.

S53B50		Sr and P40B10	
Temperature set point. (^{o}C)	Interval to set point. (min)	Temperature set point (^{o}C)	Interval to set point. (min)
400	45	400	45
800	105	800	105
1000	165	1000	165
1100	195	1100	195
1200	255	1150	255
1150	315	-	-

In the section concerning the operation of charging the furnace, different masses of blends were recorded for each of the two tests. Blend A had a mass range that varied from 35.25 g to 30.09 g, while Blend B ranged from 30.07 g to 30.13 g, and Blend C ranged from 30.57 g to 27.12 g. The duration of Blend A's exposure to the furnace spanned from 9 hours and 50 minutes to 6 hours and 40 minutes, whereas Blends B and C had shorter durations that did not exceed 6 hours. The maximum temperature attained during the melting process was

consistently 1200°C for Blend A, while Blends B and C reached slightly lower peak temperatures.

Table 4-3: Operational Parameters and Results for Melting Tests on Blends A (S53B50), B (P40B10), and C (Sr).

Furnace charge operation	Blend A		Blend B		Blend C	
	Test 1	Test 2	Test 1	Test 2	Test 1	Test 2
Blend mass (g)	35.25	30.09	30.07	30.13	30.57	27.12
Time in furnace (h: min)	9:50	6:40	5:20	6:00	5:20	7:25
Maximum temperature (°C)	1200	1200	1104	1100	1106	1120
Removal temperature (°C)	673	636	690	650	650	681
Annealed glass mass (g)	23.31	17.96	25.87	25.12	17.82	10.08

The temperature at which the blends were removed from the furnace, referred as the removal temperature in Table 4-3, exhibited slight variations among the blends. Blend A was removed at approximately 673°C and 636°C, Blend B at 690°C and 650°C, and Blend C at 650°C and 681°C. After the melting process, the mass of the annealed glass was found to be lower than the initial blend mass. Specifically, Blend A retained approximately 23.31 g to 17.96 g, Blend B ranged from 25.87 g to 25.12 g, and Blend C had a significantly lower mass of 17.82 g to 10.08 g. These variations in mass indicate different levels of material retention or transformation during the melting process.

4.3.1 Bulk Density

The bulk density measurement procedure was the water displacement method for melts A (S53B50), B (P40B10), and C (Sr). The density measurement results presented in Table 4-4 included water volume measurements across three tests for each melt type. In each test for Melt A, the initial water volume started at 50 ml and after immersion, rose to 60 ml, resulting in an average displacement of 10.3 ml. Melt B began with the same initial volume but

showed a slightly lower average displacement at 9.7 ml. Melt C, with a consistent initial volume of 50 ml, demonstrated the smallest average displacement of 8.0 ml.

Table 4-4: Water Displacement Volumes for Density Measurements of Melts A (S53B50), B (P40B10) and C (Sr).

Water volume measurement	Melt A			Melt B			Melt C		
	Test 1	Test 2	Test 3	Test 1	Test 2	Test 3	Test 1	Test 2	Test 3
Initial (ml)	50	106	140	50	101	142	50	100	138
Final (ml)	60	117	150	60	110	150	58	109	145
Displaced (ml)	10	11	10	10	11	8	8	9	7
Average (ml)	10.3			9.7			8.0		

For the density trials in Table 4-5, Melt A showed a tight grouping with two identical results of 2.33 g/cm^3 and a slightly lower 2.12 g/cm^3, averaging 2.26 g/cm^3 with a minimal standard deviation of 0.12. Melt B displayed greater variability, with measurements ranging from 2.28 to 3.14 g/cm^3, averaging 2.65 g/cm^3 and a standard deviation of 0.44, indicating less consistency in the results. Melt C had densities spanning from 1.98 to 2.55 g/cm^3, with an average of 2.25 g/cm^3 and a standard deviation of 0.28, suggesting moderate consistency across trials.

Table 4-5: Density Results of Monoliths from Melts A, B, and C.

Glasses	Trail 1 (g/cm^3)	Trail 2 (g/cm^3)	Trail 3 (g/cm^3)	Avg. (g/cm^3)	Std Dev.
Melt A (S53B50)	2.33	2.12	2.33	2.26	0.12
Melt B (P40B10)	2.51	2.28	3.14	2.65	0.44
Melt C (Sr)	2.23	1.98	2.55	2.25	0.28

4.4 Glass-ceramic Powders Preparation

Table 4-6 outlines the milling of ceramic-glass ingots and frits to produce bioglass powders. Melt A (S53B50) had two trials, starting with charge masses of 23.31 g and 17.96 g, and ending with 20.59 g and 17.05 g. The milling balls weighed around 396.08 g and did not significantly change. Melt B (P40B10) showed slight mass differences, beginning with 18.03 g and 25.14 g and ending with 17.28 g and 24.71 g, with the ball mass consistently near 396 g. Melt C (Sr) started with 17.82 g and 10.08 g, finishing with 17.39 g and 9.86 g, while the ball mass stayed at 396.01 g. This showcases the ball milling's efficiency and stability in producing powders from glass-ceramic melts, demonstrating minimal losses in mass reduction and steady ball weight suggests negligible sample contamination.

Table 4-6: Ball Milling Powder Production Pre- and Post-Grinding Masses.

Milling operation	Melt A→Powder A		Melt B→Powder B		Melt C→Powder C	
	Trail 1	Trail 2	Trail 1	Trail 2	Trail 1	Trail 2
Charge mass (g)	23.31	17.96	18.03	25.14	17.82	10.08
Ball mass before mill (g)	396.08	396.01	396.01	396.02	396.01	396.01
Discharge mass (g)	20.59	17.05	17.28	24.71	17.39	9.86
Ball mass after mill (g)	396.01	396.01	396.01	396.01	396.01	396.00

The milling results of S53B50 (Powders A and 1), P40B10 (Powders B and 2), and Sr (Powders C and 3), when analyzed for their particle size distributions in Figures 4-2 and 4-3, reveal distinct characteristics for each material under the normalized and fritted approaches.

The normalized approach resulted in a particle size distribution where D_{10} was 5.7 µm and D_{90} was 280.3 µm, indicating a broad range of particle sizes with a significant presence of larger particles in powder A. Powder B exhibited a D_{10} of 1.7 µm and a D_{90} of 56.1 µm, reflecting a much finer particle size distribution compared to Powder A. The normalized

PSD for Powder C showed the finest particle size with a D_{10} of 0.8 µm and a D_{90} of 14.1 µm, indicating a high level of powder fineness.

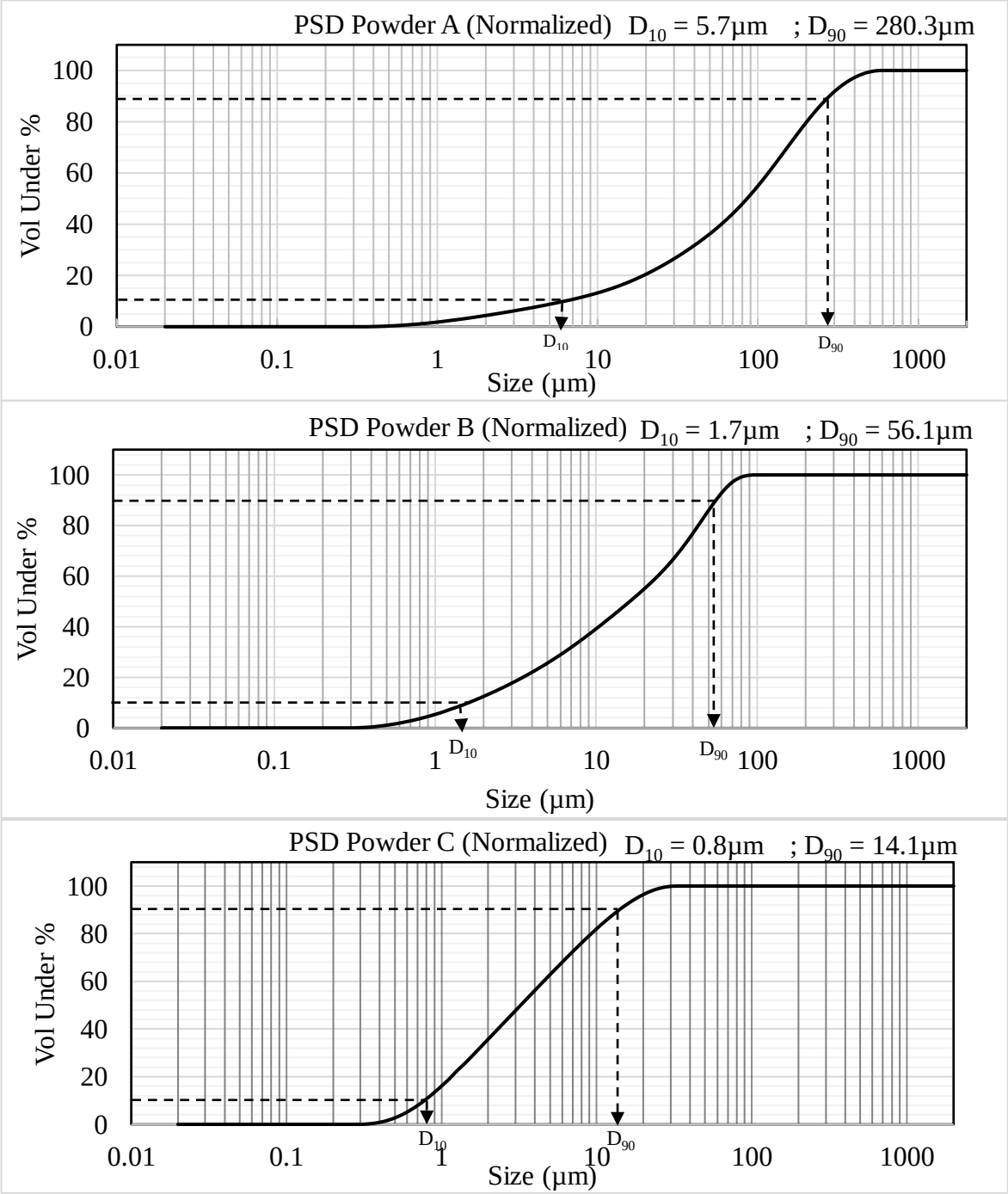

Figure 4-2: PSD Plots of Melt-Cast-Anneal or 'Normalized' S53B50 (Powder A), P40B10 (Powder B) and Sr (Powder C) Glass-Ceramic Powders.

In contrast, the fritted approach for powder 1, showed a D_{10} of 2.3 µm and a D_{90} of 98.6 µm, suggesting a finer and more uniform powder with fewer large particles. Powder 2 demonstrated a D_{10} of 2.0 µm and a D_{90} of 61.4 µm, aligning closely with the normalized

approach but slightly coarser. The fritted method powder 3 presented an even finer distribution with a D_{10} of 0.2 µm and a D_{90} of 5.6 µm, showcasing the effectiveness of the fritted approach in producing ultra-fine powders.

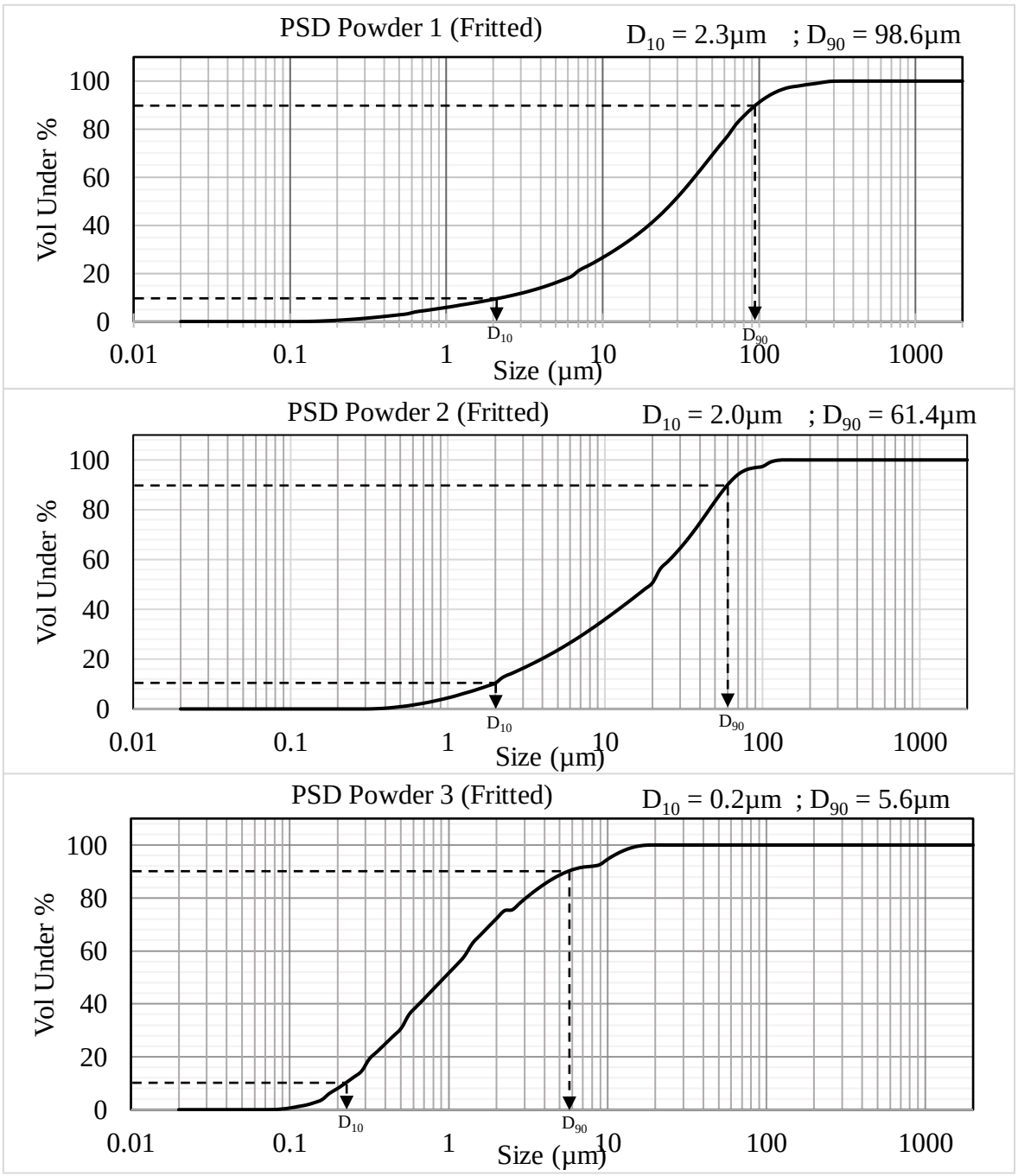

Figure 4-3: PSD Plots of Fritted S53B50 (Powder 1), P40B10 (Powder 2) and Sr (Powder 3) Glass-Ceramic Powders.

4.5 X-ray Powder Diffraction Analysis

Comparative analysis of X-ray diffraction peaks was conducted on normalized and fritted powder samples presented in Figures 4-4 and 4-5. The intensity of diffracted X-rays, measured in arbitrary units (a.u.), was plotted against the 2-theta scale, ranging from 10 to 90 degrees. Powder C showed a complex diffraction pattern with multiple sharp peaks, indicative of crystalline material. Powder B exhibited a similar complexity with fewer pronounced peaks of lower intensity compared to Powder C, suggesting a lesser degree of crystallinity. In contrast, Powder A presented a broader, hump-like pattern with no sharp peaks, suggesting an amorphous or poorly crystalline structure.

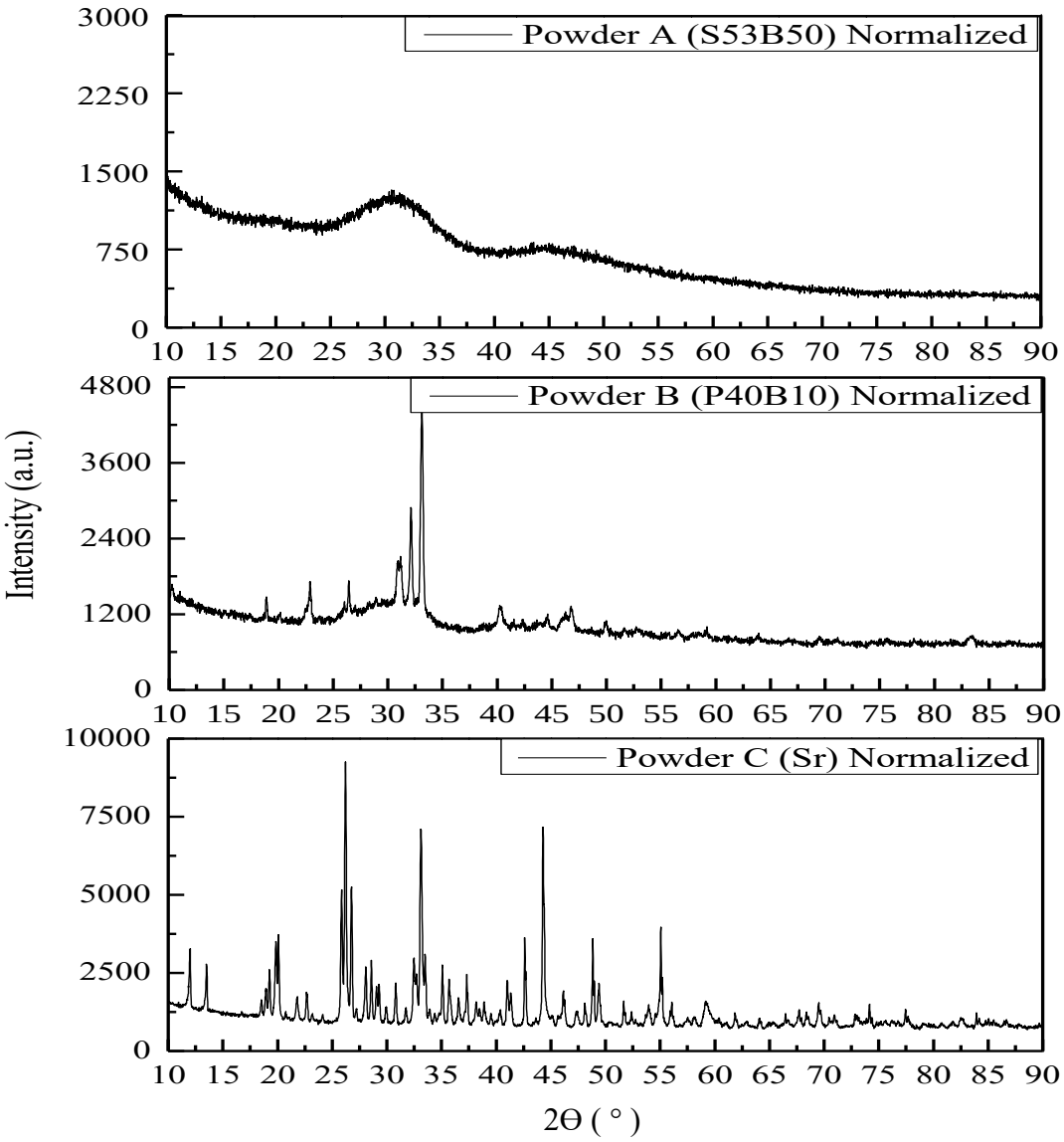

Figure 4-4: Comparative XRD Analysis of the Normalized Powders A, B and C.

The XRD analysis provided valuable insights into the microstructural changes induced by the fritting process as powder 3 exhibited a subdued and broad intensity profile with no significant peaks, indicating a largely amorphous structure or very fine crystallites. Powder 2 displayed a similar pattern to powder 3, with a broad intensity envelope and a lack of sharp peaks, which again suggests an amorphous nature. However, the presence of minor fluctuations in the intensity of powder 1 showed a slightly more pronounced peak at lower 2-theta values, suggesting some degree of crystallinity.

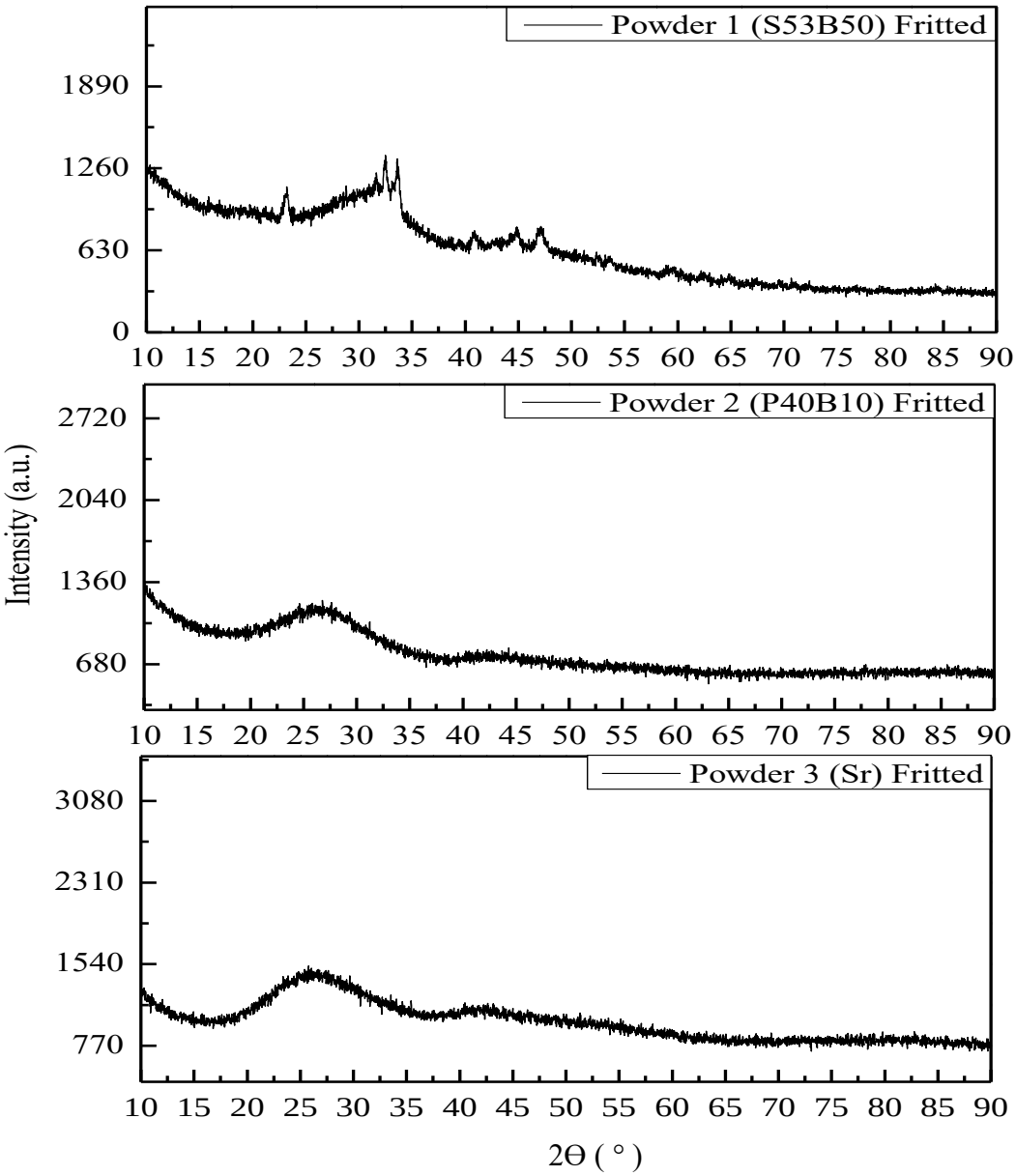

Figure 4-5: Comparative XRD Analysis of the Fritted Powders 1, 2 and 3.

4.6 FTIR Analysis

The Fourier-Transform Infrared (FTIR) spectroscopy analysis of the Zeolite Bioactive Glass (BG) scaffold presented in Figure 4-6 demonstrates distinct absorbance peaks. A significant

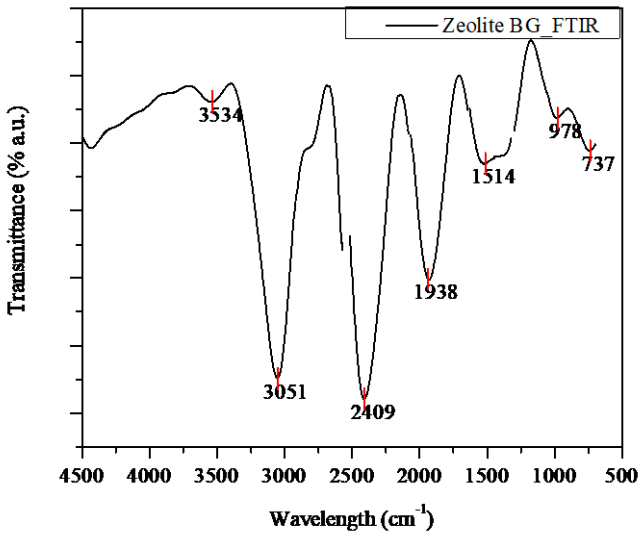

Figure 4-6: FTIR Analysis of a Zeolite Bioglass Sample.

peak was observed around 3534 cm^{-1}, as well as peaks near 3051 cm^{-1} and 2409 cm^{-1} were apparent. The spectrum showed a strong absorption band near 1938 cm^{-1} and a broad peak at 1514 cm^{-1}. Other notable peaks included those around 978 cm^{-1} and 737 cm^{-1}. Powder A in Figure 4-7 has characteristic absorbance peaks at 3440 cm^{-1}, and a strong at 2980 cm^{-1}.

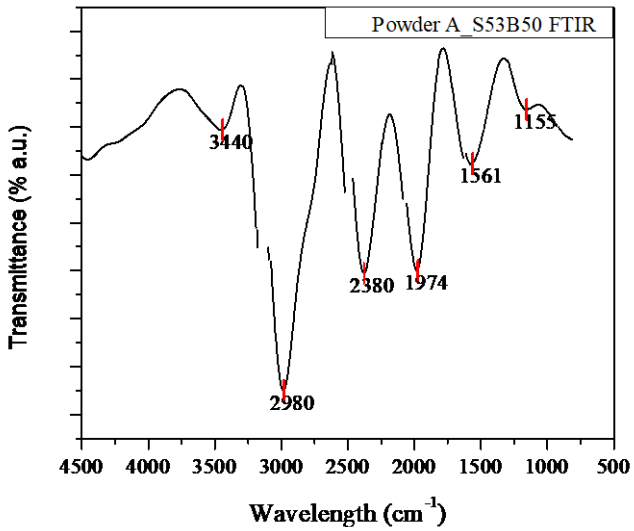

Figure 4-7: FTIR Analysis of the Borosilicate Sample.

Additional significant peaks were observed at 2380 cm^{-1} and 1974 cm^{-1}. Then, absorption features from the fingerprint region were seen at 1561 cm^{-1} and 1155 cm^{-1}.

The FTIR of Powder B in Figure 4-8 identified absorbance peaks at distinct wavenumbers. Prominent peaks were recorded at 3434 cm^{-1}, 2827 cm^{-1} and 2191 cm^{-1}. Then, fingerprint region absorption features from 1920 cm^{-1} to 1920 cm^{-1}.

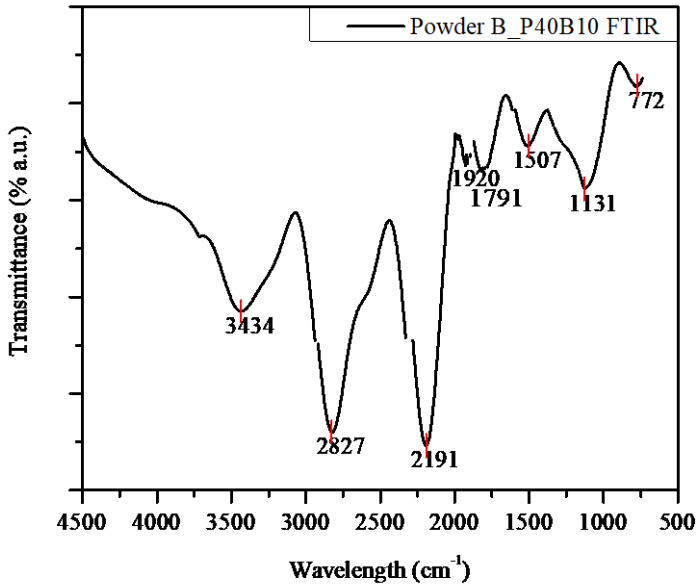

Figure 4-8: FTIR Analysis of the Borophosphate Sample.

Powder C FTIR in Figure 4-9 meticulously revealed four strong absorbance peaks that delineate its molecular structure. A prominent peak was detected at 3322 cm^{-1}, and a broader

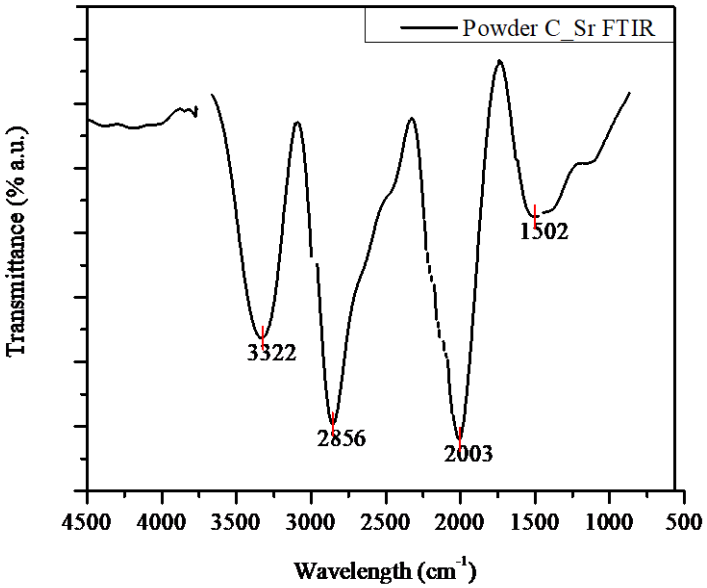

Figure 4-9: FTIR Analysis of the Phosphate Sample.

peak at 2856 cm^{-1}. The absorption peaks seen at 2003 cm^{-1} and 1502 cm^{-1} are strong as well, with later typically broad.

4.7 Powder SEM and EDS

The SEM micrograph in Figure 4-10 below is the Zeolite bioactive glass powder sample's physical morphology, displaying an array of particle sizes, where several spectrums were analyzed to assess compositional variations across the sample. The EDS data corresponding to Spectrum 22 corroborates the SEM observations, presenting an overall elemental constituent of O, Si, Na, Ca and P.

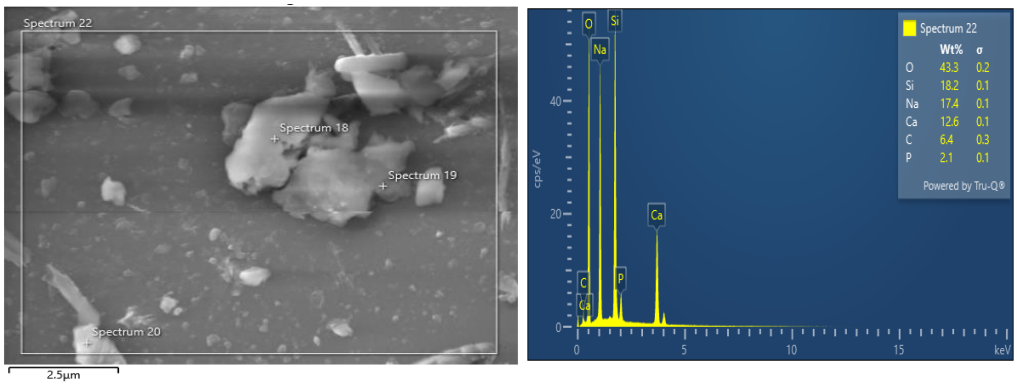

Figure 4-10: Zeolite Powder Sample Morphology SEM and EDS.

In Figure 4-11 a borosilicate powder sample micrograph, shows the varying particulate shapes and sizes typical of ground glass. This granular morphology indicates a broad distribution of particle dimensions. The associated energy-dispersive X-ray spectroscopy (EDX) spectrum identifies the elemental composition with notable peaks for Si, O, and minor peaks for Na, Ca, C, Mg, and Al. The EDX analysis demonstrates a homogenous elemental distribution across the scanned area, suggesting a uniform glass composition.

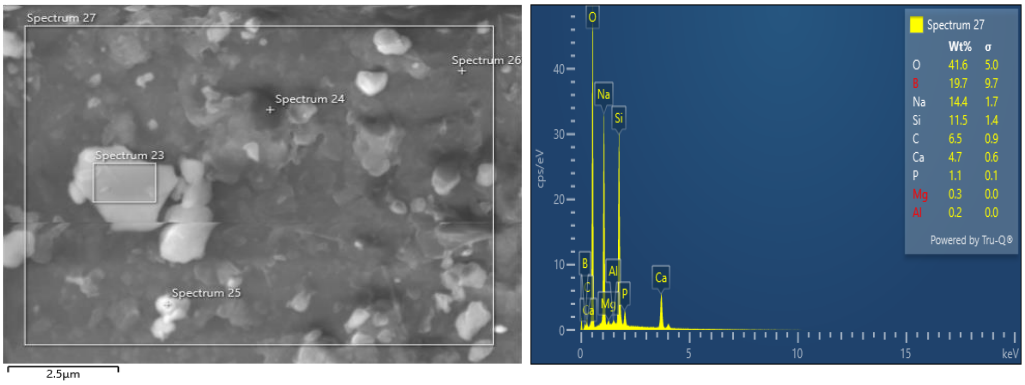

Figure 4-11: Borosilicate Powder A Sample Morphology SEM and EDS.

The electron micrograph in Figure 4-12 depicts a borophosphate glass sample with a varied particulate landscape, showcasing a mix of both fine and larger crystalline-like structures. The heterogeneity in particle size distribution is evident. Energy-dispersive X-ray spectroscopy (EDX) analysis reveals prominent peaks for O, P, Ca, and Sr, with minor peaks for Na, Al, and trace levels of Cu. The high levels of phosphorus and oxygen correlate with the phosphate backbone of the glass network, while the presence of strontium and calcium highlights the potential for bioactive properties.

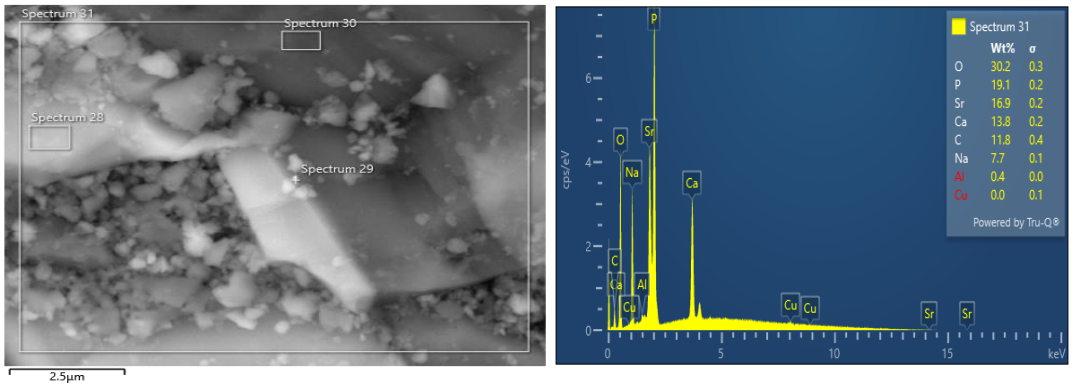

Figure 4-12: Borophosphate Powder B Sample Morphology SEM and EDS.

Micrograph Figure 4-13 showcases the phosphate sample with a prominent crystalline structure. The particle morphology, as visualized, indicates a well-defined, faceted crystal, likely representative of a mature crystallization process. The energy-dispersive X-ray spectroscopy (EDX) data associated with the micrograph reveals a significant peak for Sr, O, C, P, and Na.

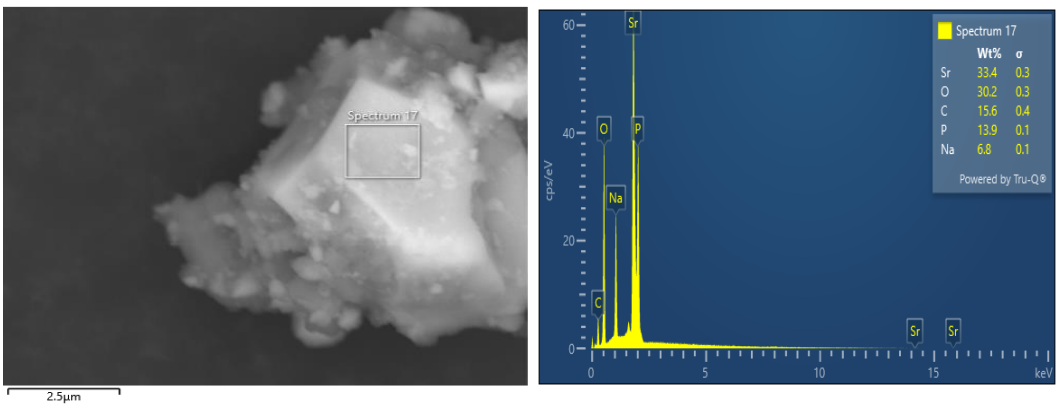

Figure 4-13: Phosphate Powder C Sample Morphology SEM and EDS.

4.8 Spark Plasma Sintering Scaffold Fabrication

In the fabrication of porous scaffolds via Spark Plasma Sintering (SPS), varied sintering temperatures and times were used for the different sample compositions. Samples S53B50 and P40B10, with initial masses ranging from 4.02 g to 4.06 g, underwent sintering at temperatures between 540°C and 610°C for a duration of 10 minutes each see Table 4-7.

Figure 4-14: S53B50 Sintered Specimen before NaCl Porogen Removal by Salt Leaching.

Table 4-7: Varied Sintering Parameters and Corresponding Masses of Porous Scaffolds Post-Leaching.

Sintering Sample	Powder + NaCl Sample Mass (g)	Sintering Temperature (°C)	Sintering Time (min)	Scaffold Mass after Salt Leaching (g)
S53B50	4.08	550	10	Not sintered
S53B50	4.06	590	10	2.37
S53B50	4.02	610	10	2.53
P40B10	4.01	540	10	Not sintered
P40B10	4.05	570	10	2.44
P40B10	4.01	600	10	2.38
Sr	4.00	460	10	Not sintered
Sr	4.02	490	10	2.88
Sr	4.02	520	10	2.74

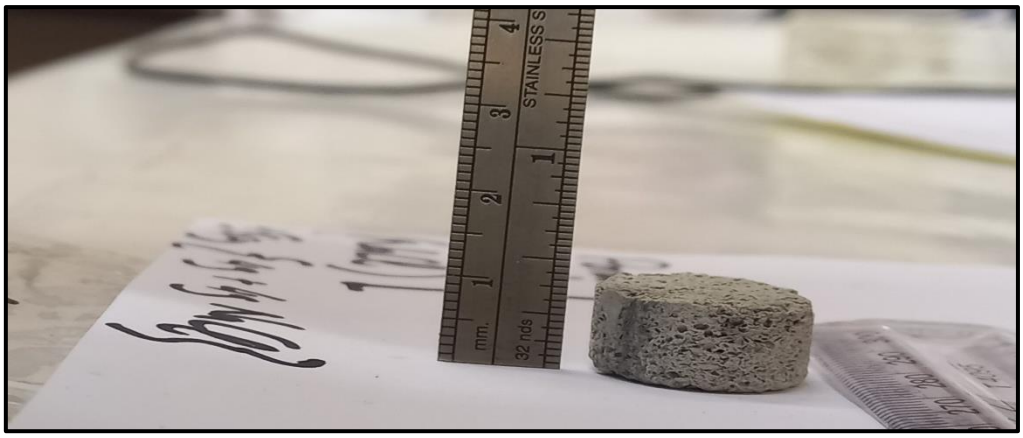

Figure 4-15: S53B50 Sintered Specimen after Nacl Porogen Removal by Salt Leaching.

The S53B50 samples sintered at 590 °C and 610 °C (Fig 4-14 and-15) resulted in post-leaching masses of 2.37 g and 2.53 g, respectively, while the P40B10 samples sintered at 570 °C and 600 °C exhibited final masses of 2.44 g and 2.38 g (Fig 4-16). Notably, the S53B50 and P40B10 samples set to sinter at 550 °C and 540 °C, respectively, were not sintered. Additionally, Sr samples with a consistent mass of 4.02 g were sintered at lower temperatures of 490 °C and 520 °C, also for 10 minutes, resulting in post-leaching masses of 2.88 g and 2.74 g upon completion.

Figure 4-16: Porous Scaffolds After Ultrasonic Cleaning and NaCl leaching.

4.8.1 Scaffold's Phase Identification X-ray Diffraction

The XRD pattern analysis of two S53B50 samples, sintered at 590°C and 610°C, revealed distinct phase compositions. The sample sintered at 590°C exhibited a pattern indicating the presence of calcium silicate (Ca_2SiO_4), silicon oxide (SiO_2), sodium calcium phosphate ($NaCaPO_4$), and boron oxide (B_2O_3), as matched with the International Centre for Diffraction Data (ICDD) reference codes in Table 4-8.

Table 4-8: S53B50 Scaffold Phase Identification XRD.

Ref. Database	Ref. Code	Compound Name	Chemical Formula	Fig. 4-17 Legend
ICDD	00-020-0236	Calcium Silicate	Ca_2 Si O_4	▲
ICDD	00-038-0903	Oxygen	O_2	❤
ICDD	01-076-0647	Silicon Oxide	Si O_2	★
ICDD	00-029-1194	Sodium Calcium Phosphate	Na Ca (P O_4)	■
ICDD	01-076-0781	Boron Oxide	B_2 O_3	●

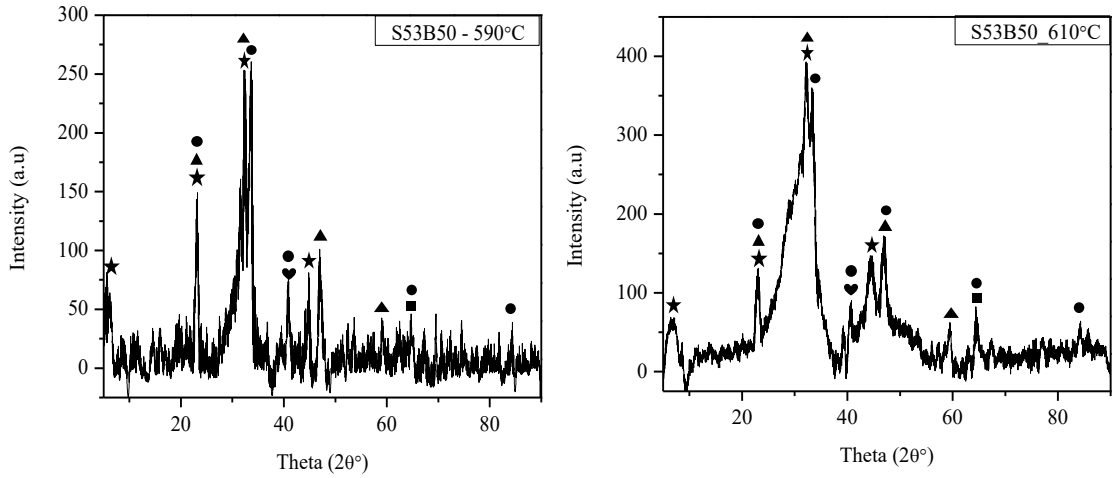

Figure 4-17: S53B50 Sintered at 590ºC and 610ºC XRD Patterns.

The peaks intensity changed significantly sintering at 610°C evident in Figure 4-17, suggesting a transformation or growth in the crystalline phases. The most notable change implied enhanced crystallization or a higher degree of ordering within these phases at the elevated temperature. The results imply that the sintering process at 610°C may enhance the crystallinity of certain phases within borosilicate glass.

The XRD analysis conducted on P40B10 samples sintered at 570°C and 600°C presented identifiable phases reported in Table 4-9. For the sample sintered at 570°C, the XRD pattern showed prominent peaks that corresponded to the presence of boron oxide (B_2O_3), sodium oxide (NaO_2), lime (Ca_4O_4), phosphorus oxide (P_2O_5), strontium borate ($SrO(B_2O_3)_2$), and oxygen (O_2), with reference codes from ICDD and Crystallography Open Database (COD) databases.

Table 4-9: P40B10 Scaffold Phase Identification XRD

Ref. Database	Ref. Code	Compound Name	Chemical Formula	Fig. 4-18 Legend
ICDD	00-024-0160	Boron Oxide	$B_2\ O_3$	○
ICDD	01-077-0208	Sodium Oxide	$Na\ O_2$	□
COD	96-900-6704	Lime	$Ca_4.00\ O_4.00$	△
ICDD	01-087-0952	Phosphorus Oxide	$P_2\ O_5$	☆
ICDD	01-074-1587	Strontium Borate	$Sr\ O\ (B_2\ O_3)_2$	⬠
ICDD	01-073-0229	Oxygen	O_2	♡

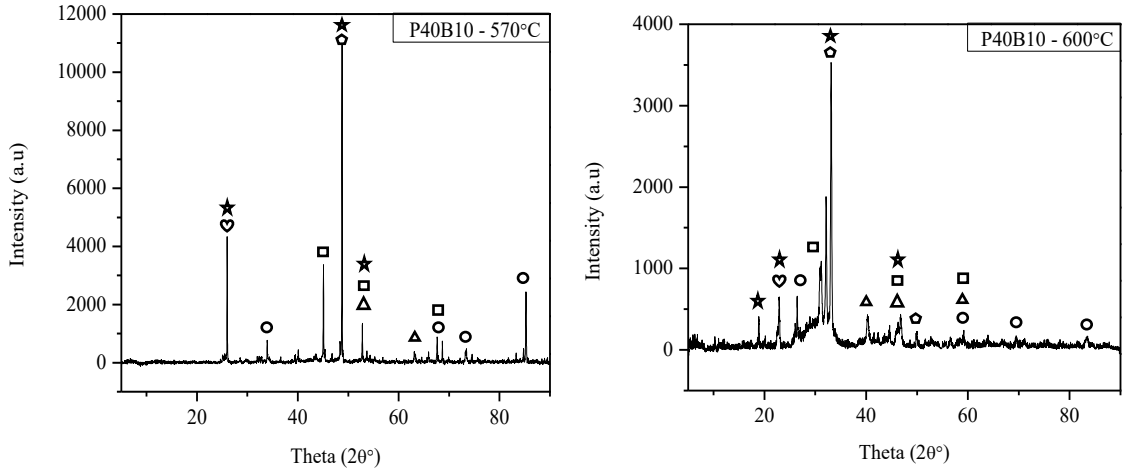

Figure 4-18: P40B10 Sintered at 570ºC and 600ºC XRD Patterns.

Sintering at an elevated 600°C resulted in a discernible shift in the intensity of the peaks in Figure 4-18. This shift suggests an alteration in the crystallinity or least likely a quantity of the phases present. The data indicated that higher temperature might promote the growth or better crystallinity of phases like boron oxide and strontium borate, which were consistent with the ICDD reference codes 00-024-0160 and 01-074-1587.

Analysis of two phosphate glass samples, sintered at 490°C and 520°C, displayed varying crystalline structures. The sample processed at 490°C showed a relatively low-intensity pattern, indicative of a less crystalline structure. Reference to the phase-matched table confirmed the presence of phases such as phosphorus oxide (P_2O_5), sodium oxide (NaO_2), and strontium-related compounds including strontium oxide (SrO), strontium phosphate ($Sr_3(PO_4)_2$), and strontium phosphide (Sr_3P_2), based on ICDD reference codes.

Table 4-10: Sr Scaffold Phase Identification XRD

Ref. Database	Ref. Code	Compound Name	Chemical Formula	Fig. 4-19 Legend
ICDD	00-005-0318	Phosphorus Oxide	$P_2 O_5$	☆
ICDD	01-077-0209	Sodium Oxide	$Na O_2$	⚄
ICDD	00-027-1304	Strontium Oxide	Sr O	⬠
ICDD	00-014-0271	Strontium Phosphate	$Sr_3 (P O_4)_2$	❂
ICDD	00-023-0549	Strontium Phosphide	$Sr_3 P_2$	⚠
ICDD	00-011-0648	Sodium Phosphate	$Na P O_3$	😍

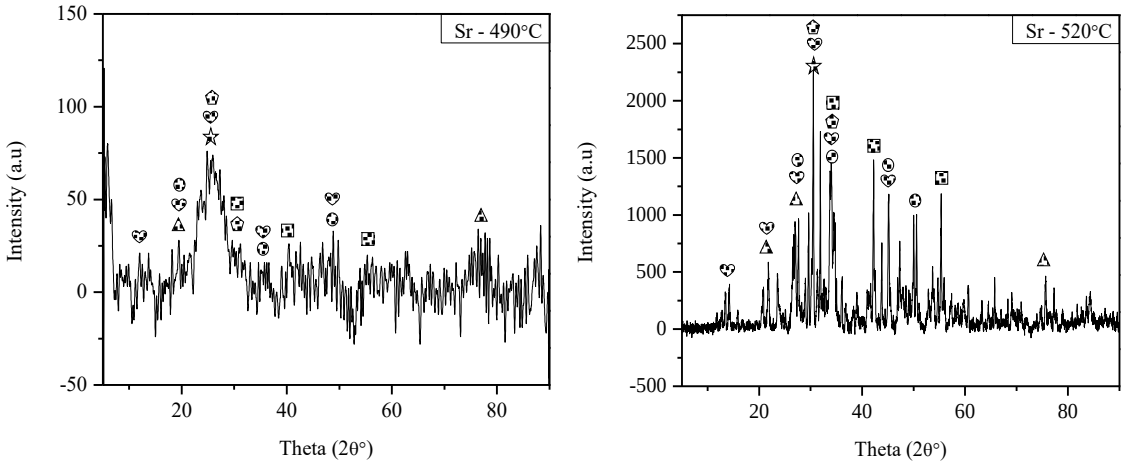

Figure 4-19: Sr Sintered at 490ºC and 520ºC XRD Patterns.

Sr scaffold sintered at 520°C XRD pattern revealed a significant increase in peak intensity, suggesting a greater degree of crystallization. Notable was the emergence of pronounced peaks corresponding to strontium phosphate and sodium phosphate, with reference codes 00-014-0271 and 00-011-0648, indicating that these phases were more prevalent at the higher sintering temperature.

4.8.2 Scaffold's Crystallization X-ray Diffraction

Initially, the raw XRD data of post-sintering samples presented in section 4.8.1 above were noisy; however, subsequent smoothing enhanced the data's clarity. By integrating the refined curves in Origin software to measure area, crystallinity defined by Mannan *et al.*, (2005) as $Crystallinity\ index = \frac{Area\ of\ all\ crystalline\ peaks}{Area\ of\ all\ crystalline\ and\ amorphous\ peaks}$ was quantified in each sample. These findings underpin discussions on how sintering temperature affects crystallinity, mechanical integrity, and degradation patterns of the glass scaffolds.

In the S53B50 patterns in Figure 4-20; sample sintered at 590°C showed a lower sum of crystalline peaks area with values of 1000.66, 985.37, and 1028.57, correlating to a crystallinity index of 47.44%. Conversely, the scaffold sintered at 610°C displayed a

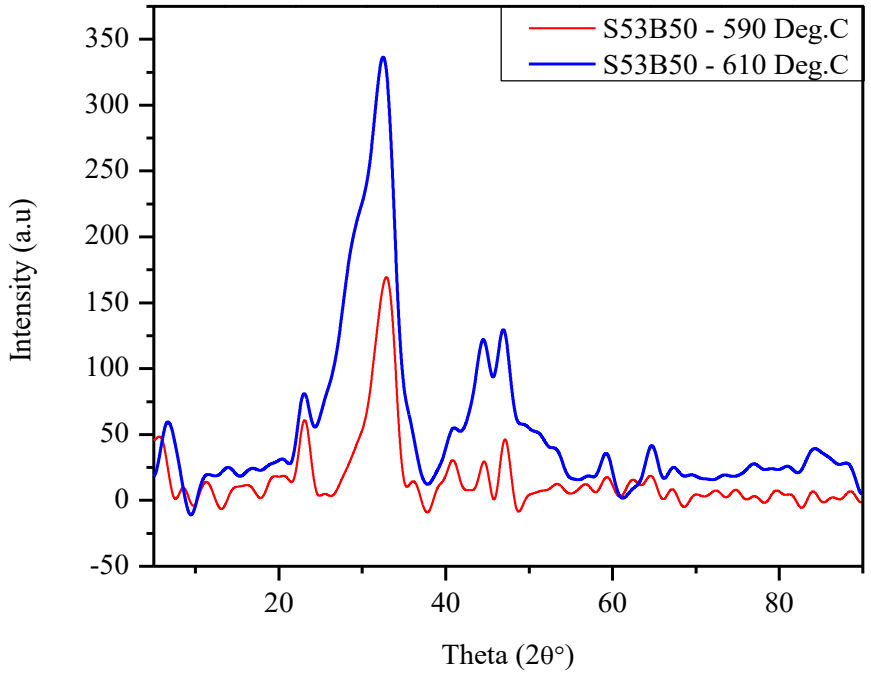

Figure 4-20: Smoothed S53B50 Scaffold's Crystallization XRD Patterns.

significant increase in the sum of crystalline peaks area, presenting values of 2972.19, 3186.47, and 3277.28, which corresponded to a crystallinity index of 57.59%. This increment in crystallinity index with the elevation of sintering temperature suggests a positive correlation between sintering temperature and the development of crystalline phases within the glass matrix.

Table 4-11: Post-sintering S53B50 Scaffolds' Crystallinity Indexes.

Sintered Scaffolds	Sum of Crystalline Peaks Area			Area of Crystalline + Amorphous Peaks	Crystallinity Index (Avg. %)
	Measure 1	Measure 2	Measure 3		
S53B50 - 590°C	1000.66	985.37	1028.57	2118.17	47.44
S53B50 - 610°C	2972.19	3186.47	3277.28	5461.64	57.59

The P40B10 scaffolds sintered at 570°C showed a sum of crystalline peaks area with the measures of 5531.17, 5711.35, and 5668.56 reported in Table 4-12. This resulted in a calculated crystallinity index of 45.12%. In comparison, the scaffolds sintered at 600°C exhibited a similar sum of crystalline peaks area with values of 5527.32, 5865.70, and 5377.97. However, the crystallinity index for these scaffolds increased to 57.06%. The increase in crystallinity index with the higher sintering temperature indicates a greater degree

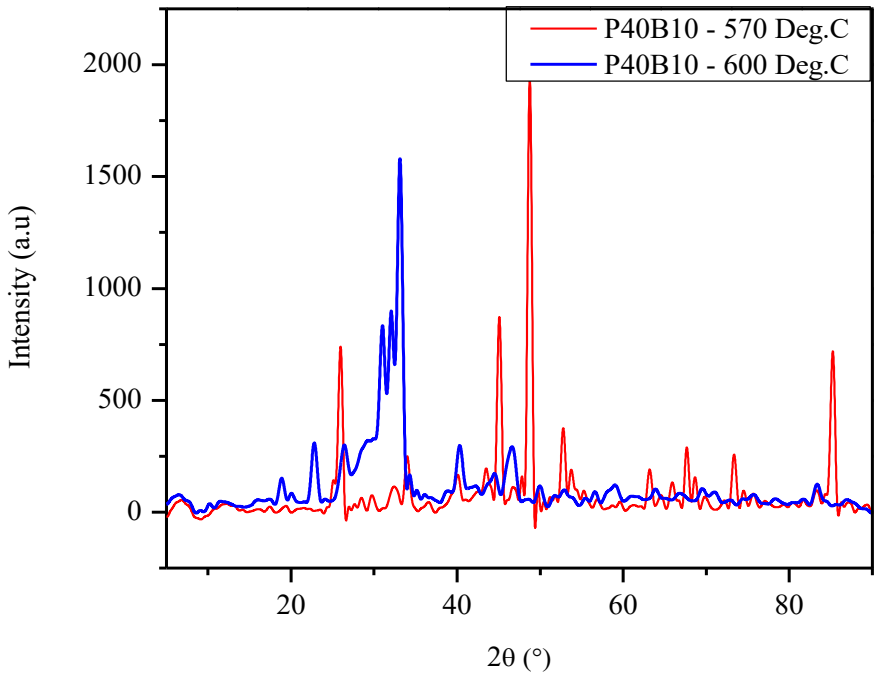

Figure 4-21: Smoothed P40B10 Scaffold's Crystallization XRD Patterns.

of crystalline phase development in the scaffold sintered at 600°C. These data suggest a direct influence of sintering temperature on the crystallinity and potentially on the mechanical properties of the P40B10 glass scaffolds.

Table 4-12: Post-sintering P40B10 Scaffolds' Crystallinity Indexes.

Sintered Scaffolds	Sum of Crystalline Peaks Area			Area of Crystalline + Amorphous Peaks	Crystallinity Index (Avg. %)
	Measure 1	Measure 2	Measure 3		
P40B10 - 570°C	5531.17	5711.35	5668.56	12492.64	45.12
P40B10 - 600°C	5527.32	5865.70	5377.97	9797.33	57.06

The sample sintered at 490°C had an average crystallinity index of 59.58% based on the measured sum of crystalline peaks area. In contrast, the sample sintered at 520°C had a

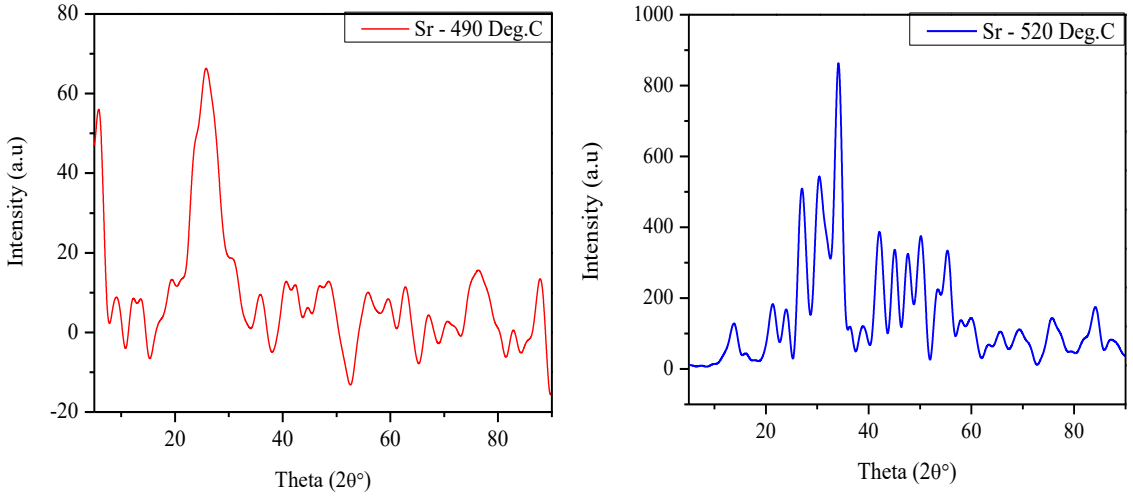

Figure 4-22: Smoothed Sr 490ºC and 520ºC Scaffold's Crystallization XRD Patterns.

higher average crystallinity index of 67.80%. This indicates a more pronounced crystalline phase formation at the higher sintering temperature.

Table 4-13: Post-sintering Sr Scaffolds' Crystallinity Indexes.

Sintered Scaffolds	Sum of Crystalline Peaks Area			Area of Crystalline + Amorphous Peaks	Crystallinity Index (Avg. %)
	Measure 1	Measure 2	Measure 3		
Sr - 490°C	1143.93	1315.75	1274.57	2089.34	59.58
Sr - 520°C	8151.71	7652.51	7953.33	11680.58	67.80

4.9 Porosity Analysis

The porosity of scaffold specimens at varying sintering temperatures is tabulated in 4-14 using the formula $\%Porosity = \left(1 - \frac{D_b}{D_{th.}}\right) \times 100$, where D_b is the measured specimen density and $D_{th.}$ is the theoretical density (Flint and Flint, 2002). The table showcases the calculated porosity values, indicating how porosity varies inversely with bulk density and directly with theoretical density.

Table 4-14: Comparative Analysis of Porosity in Scaffold Specimen at Different Sintering Temperatures.

Specimen	Measured density (g/cm^3)	Theoretical density (g/cm^3)	Relative density (%)	Porosity (%)
Sr 490°C	0.88	2.65	33.2	66.8
Sr 520°C	1.12	2.65	42.3	57.7
P40B10 570°C	0.98	2.25	43.6	56.4
P40B10 600°C	1.03	2.25	45.8	54.2
S53B50 590°C	0.91	2.26	40.3	59.7
S53B50 610°C	1.04	2.26	46.0	54.0

The scanning electron microscope (SEM) micrographs of the scaffold samples revealed distinct porosity characteristics. Scaffold A, prepared at S53B50 610°C, displayed a uniform pore distribution with a moderate level of interconnectivity, as evidenced by the visible open channels between pores. This sample achieved a measured density of 1.04 g/cm^3, with a porosity of 54.0%, indicating a substantial void volume within the structure.

Scaffold B, corresponding to P40B10 sintered at 600°C, showed a more irregular pore structure with less uniformity in size and distribution. The interconnectivity appeared reduced compared to Scaffold A, with fewer open channels visible in the SEM image. The porosity table reflects this observation with a slightly lower porosity percentage of 54.2% and a measured density of 1.03 g/cm^3.

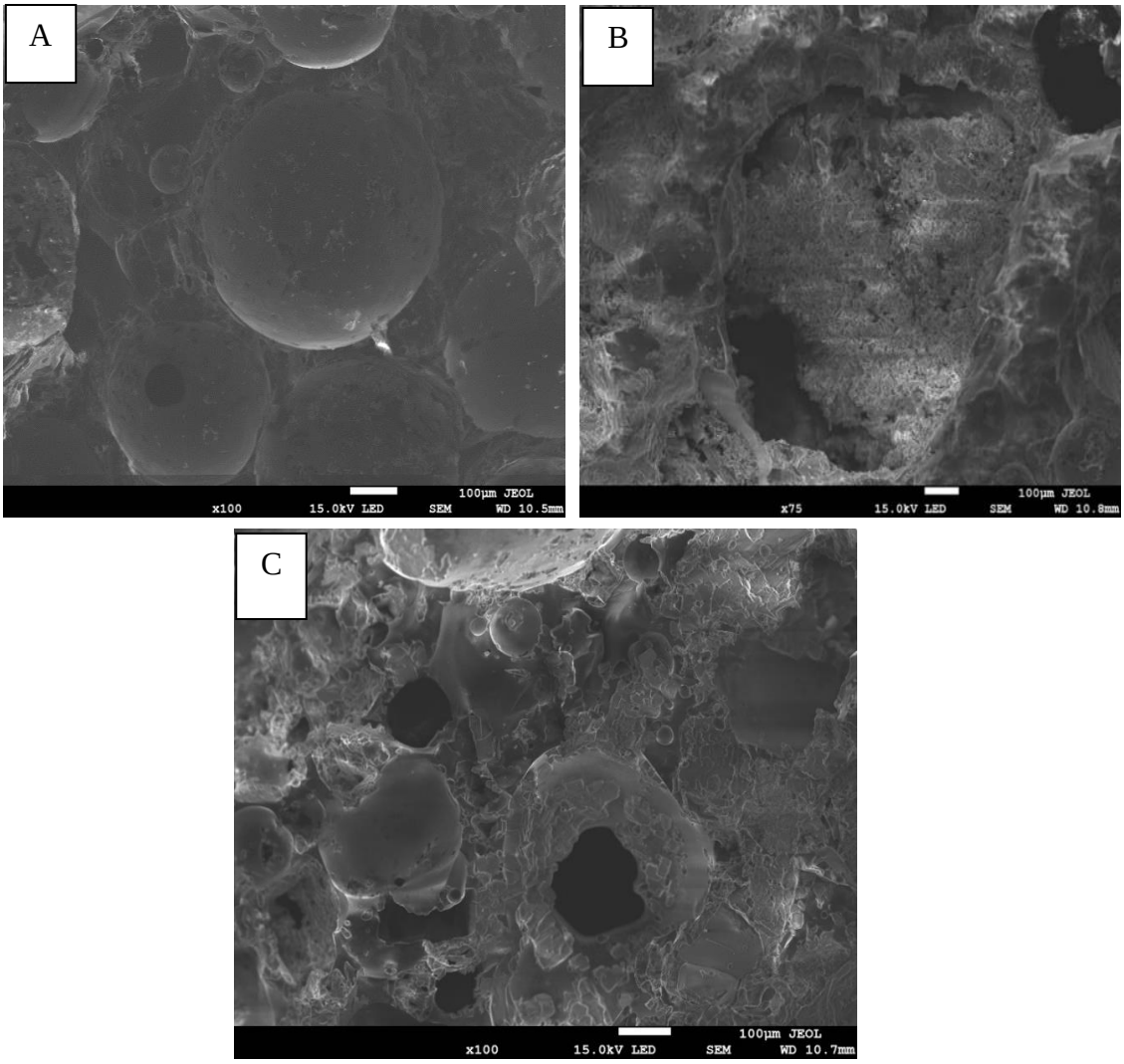

Figure 4-23: Porous Scaffolds' SEM Micrographs; A (S53B50 610ºC), B (P40B10 600ºC) and C (Sr 520ºC).

Lastly, Scaffold C, representing Sr bioactive glass sintered at 520°C, exhibited the highest level of porosity among the samples, with very pronounced, large pores and extensive interconnectivity. This is confirmed by the table, which lists a porosity of 57.7% and a measured density of 1.12 g/cm³, suggesting a highly porous matrix that would be conducive to tissue integration in biomedical applications.

Additionally, FIJI ImageJ software facilitated the quantitative measurements of porosity by processing sectional images A (S53B50 590°C), B (S53B50 610°C), C (P40B10 600°C), and D (Sr 520°C). The software enabled the extraction of pore size range, average pore size, total porous area, total surface area, and the porous fraction reported in Table 4-15.

Table 4-15: FIJI ImageJ Porosity Measurements of Scaffolds' Sectional Surface Micro Images.

Specimen	Pores Size Range (min. – max.) (µm)	Average Pore Size (µm)	Total Porous Area (μm^2)	Total Surface Area (μm^2)	Porous Fraction (%)
S53B50 - 590°C	132.2 – 652.4	436.4 (±54.9)	2267188.4	9566662.1	23.7
S53B50 - 610°C	395.0 – 879.7	624.4 (±53.8)	3859193.6	9503305.6	40.6
P40B10 - 600°C	215.4 – 1193.3	617.7 (±179.4)	5428365.7	9573642.7	56.7
Sr - 520°C	281.1 – 949.9	589.5 (±114.6)	3434549.6	9115831.7	37.7

Image A (S53B50 590°C) exhibited a wide range of pore sizes with an average size of 436.4 µm. The total porous area was 2267188.4 µm², accounting for 23.7% of the material. The micrograph indicated some interconnectivity between the pores. Image B (S53B50 610°C) had a narrower pore size distribution with a higher average size of 624.4 µm. The total porous

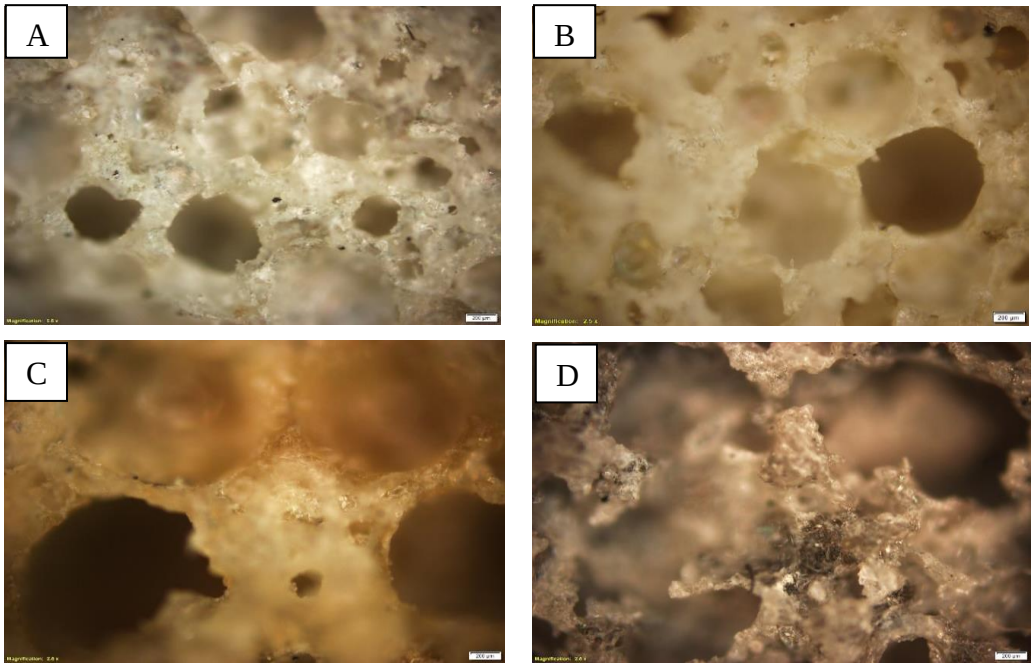

Figure 4-24: Porous Scaffolds' Sectional Surface Microscopic Sectional Images A (S53B50 590°C), B (S53B50 610°C), C (P40B10 600°C), and D (Sr 520°C).

area was 3859193.6 µm², representing 40.6% of the material. Enhanced interconnectivity was observed. Image C (P40B10 600°C) had a pore size range of 215.4–1193.3 µm and the

highest average size of 617.7 μm. The total porous area was 5428365.7 μm², accounting for 56.7% of the material. Image D (Sr 520°C) displayed pore sizes ranging from 281.1 to 949.9 μm with an average of 589.5 μm. The total porous area was 3434549.6 μm², yielding a porous fraction of 37.7%. These results demonstrate the impact of sintering temperatures on the porosity.

4.10 Mechanical Properties

4.10.1 Compression Load Bearing Test

Compression load-bearing tests were conducted to determine the mechanical properties of the various produced scaffolds. The study investigated specimens sintered at the highest designated temperatures, therefore Sr at 520°C, P40B10 at 600°C, and S53B50 at 610°C. Each scaffold underwent a compression test, measuring the compressive stress and corresponding extension to report mechanical robustness in Table 4-16.

Table 4-16: Compression Load Bearing Analysis of Selected Porous Scaffolds.

Specimen	Diameter (mm)	Anvil height (mm)	Maximum Comp. Load (kN)	Compressive stress at Maximum Comp. load (MPa)	Compressive extension at Maximum Comp. load (mm)
Sr –520°C	19.92	11.00	-0.254	0.8	1.62
P40B10 – 600°C	19.98	10.88	-0.246	0.8	0.67
S53B500 - 610°C	20.00	10.95	-0.529	1.7	0.57

The Sr specimen, with a diameter of 19.92 mm and an anvil height of 11.00 mm, exhibited a maximum compression load of -0.254 kN, translating to a compressive stress of 0.8 MPa at a compressive extension of 1.62 mm. The P40B10 scaffold, similar in size with a 19.98 mm diameter and a 10.88 mm anvil height, demonstrated identical compressive stress at maximum compression load and a slightly lower compressive extension of 0.67 mm.

The S53B50 scaffold, measured at 20.00 mm in diameter and 10.95 mm in anvil height, showed a notable increase in compressive strength, with a maximum load of -0.529 kN

resulting in a higher compressive stress of 1.7 MPa. This sample also had a reduced compressive extension at maximum load, recorded at 0.57 mm, indicating a higher resistance to deformation under the same loading conditions.

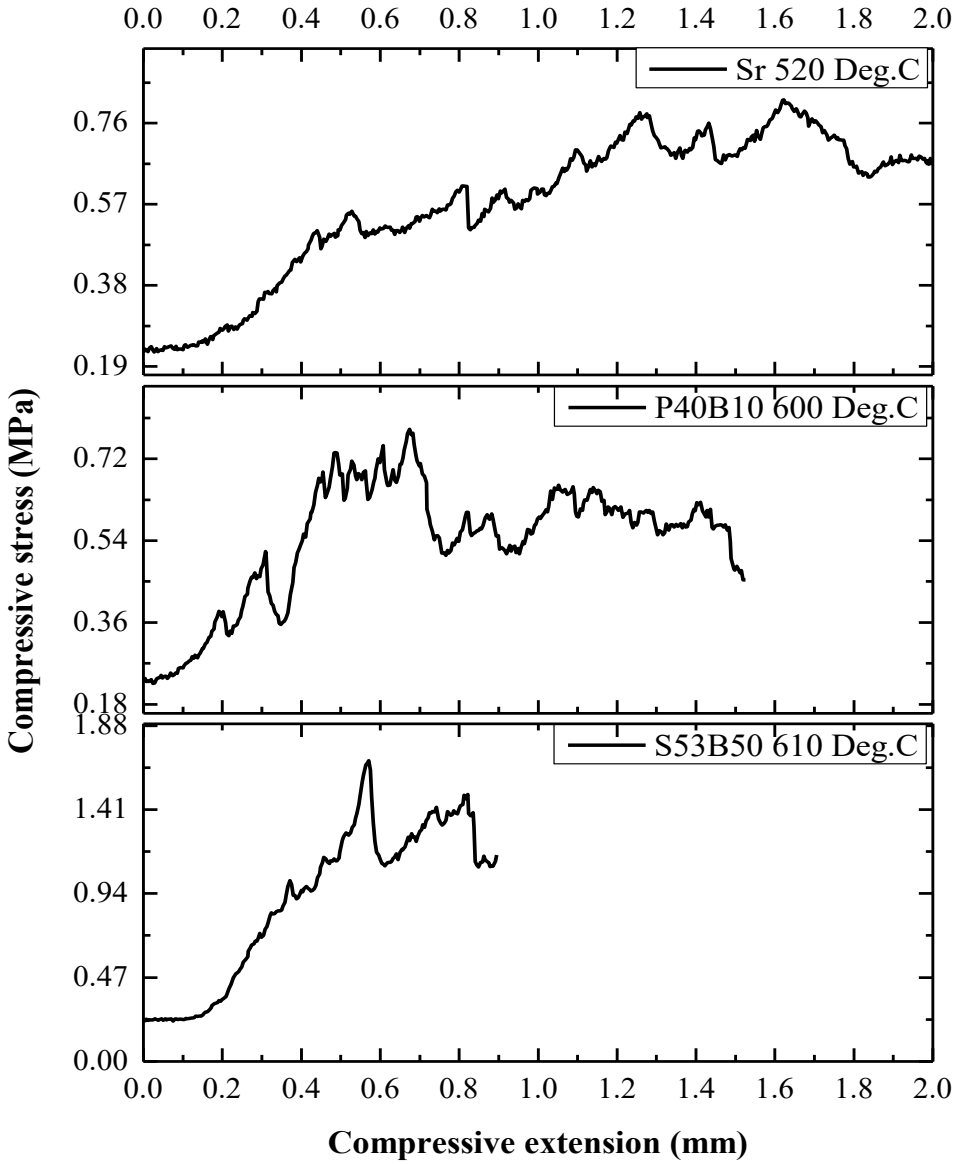

Figure 4-25: Compression Stress-Extension Tests of Scaffolds Sr, P40B10 and S53B50.

The graphical representation of the results in Figure 4-25 depicted a trend where higher compressive strength corresponded to decreased compressive extension. Implying that the mechanical integrity of scaffolds can be tailored for a range of different application.

4.10.2 Tribology Wear Analysis

The table presented a comprehensive tribology wear analysis of porous scaffold samples subjected to different standard loads. The analysis actively focused on three critical parameters: worn track area, wear rate, and coefficient of friction.

Table 4-17: Wear Resistance Results of Sr, P40B10 and S53B50 Scaffolds Tested at 3 and 5 N Standard Loads.

Specimen	Std. Load (N)	Worn Track (μm^2)	Wear Rate ($mm^3/N/m$)	Friction Coef. (μ)
Sr - 490°C	3	289.2	9.637E-005	0.809 (±0.185)
Sr - 490°C	5	218.9	4.378E-005	0.628 (±0.151)
P40B10 - 600°C	3	1516.2	0.0005053	0.591 (±0.196)
P40B10 - 600°C	5	38.0	7.593E-006	0.119 (±0.050)
S53B50 - 590°C	3	14315.9	0.004773	0.642 (±0.104)
S53B50 - 590°C	5	38629.5	0.007725	0.655 (±0.126)

For Sr - 490°C specimens, increasing load from 3N to 5N, the worn track area reduced from 289.2 µm² to 218.9 µm², wear rate from 9.637E-005 to 4.378E-005 mm³/Nm, and friction coefficient from 0.809 to 0.628, suggesting tighter compaction and improved wear resistance and tribological properties.

Similarly, for P40B10 - 600°C samples, increasing the load from 3N to 5N decreased the worn track area from 1516.2 µm² to 38.0 µm². The wear rate reduced significantly from 0.0005053 mm³/Nm to 7.593E-006 mm³/Nm, and the friction coefficient dropped from 0.591 to 0.119, indicating improved wear characteristics.

In contrast, S53B50 - 590°C samples exhibited an increase in worn track area from 14315.9 µm² to 38629.5 µm² and wear rate from 0.004773 to 0.007725 mm³/Nm. However, the friction coefficient slightly increased from 0.642 to 0.655, indicating a marginal change in tribological performance. Overall, the wear behaviours varied across different specimens and conditions, with Sr - 490°C and P40B10 - 600°C samples showing better wear resistance with increased load, while S53B50 - 590°C samples displayed a contrary trend.

CHAPTER 5: DISCUSSION

Chapter 5 discusses the synthesis success of glass powders and the fabrication of porous scaffolds using SPS, showcasing their suitability for medical applications through mechanical property evaluations. The chapter further explores the optimal porosity for bone ingrowth and potential medicinal biomolecule loading, presenting a comprehensive discussion on scaffold preparation, crystallinity, and mechanical properties, including compressive strength and wear resistance, to underscore the research objectives in scaffold development for medical applications.

5.1 Preparation of Highly Porous Bioactive Glass Scaffolds

5.1.1 Methodology and Process

Three bioactive glass batches were prepared with distinct compositions: Borosilicate (S53B50), Borophosphate (P40B10), and Phosphate (Sr). Starting batch preparation involved calculating oxide compositions and corresponding reagent masses detailed in section 3.2, then characterizing temperature stability to achieve homogeneous melting.

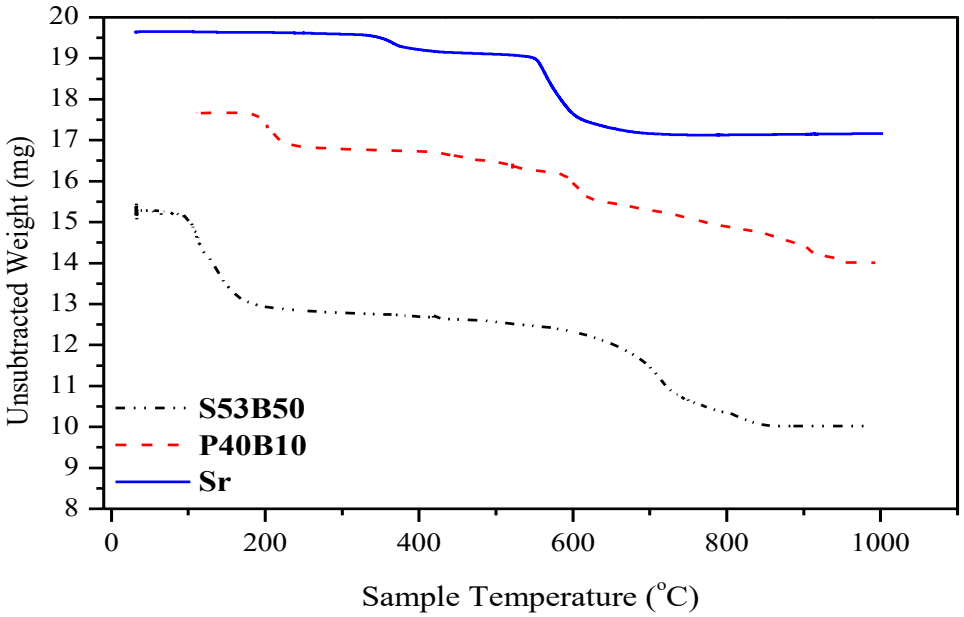

Figure 5-1: Decomposition and Thermal Stability of S53B50, P40B10 and Sr.

TGA of bioactive glass compositions, as evidenced by the Figure 5-1 above, indicates the thermal stability and decomposition patterns of each glass type. S53B50 glass exhibited a significant mass loss of 34.5% within the range of 600-900°C, aligning with findings that borosilicate glasses undergo considerable structural changes within this temperature bracket (Tainio *et al.*, 2017). Conversely, the P40B10 glass displayed a lower mass loss of 16.92% between 300-700°C, indicative of its comparatively higher thermal stability, which is critical for applications requiring gradual degradation (Gharbi *et al.*, 2023). The glass melting curve,

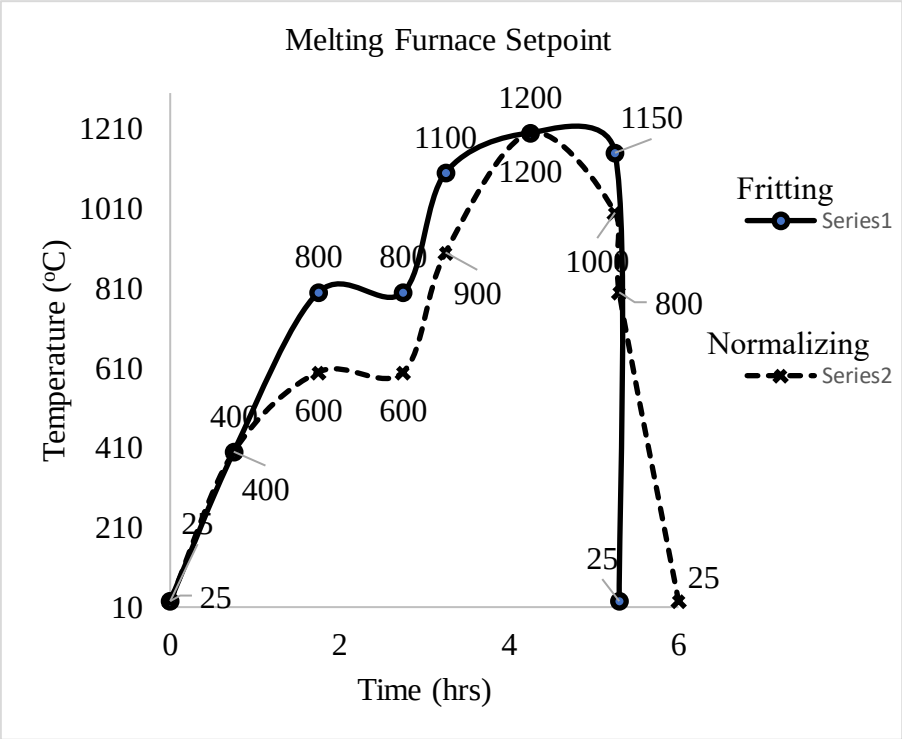

Figure 5-2: Melt Derivation Curves Show Temperature Holding at 800 and 900 ^{O}C, for Complete Decomposition, Homogenous Melting Above 1100 ^{O}C and Rapid Cooling Glass Formation.

peaking at around 1200°C for S53B50 and 1100°C for P40B10 and Sr, underlines the material's response to high-temperature processing, a feature essential for scaffold manufacturing. The retained masses post-melting, which are substantial, suggest a strong, stable glass network post-thermal treatment, beneficial for the intended structural and medical applications of the bioactive glasses (Qi *et al.*, 2018).

Summary of particle size distributions from milling displays a comparative analysis of fritted versus normalized samples in Figure 5-3. The fritted S53B50 exhibited a smaller median particle size (D_{10}) and a much larger size at the 90th percentile (D_{90}), indicating a broad size distribution. This trend was similarly observed, albeit less pronounced, in the P40B10

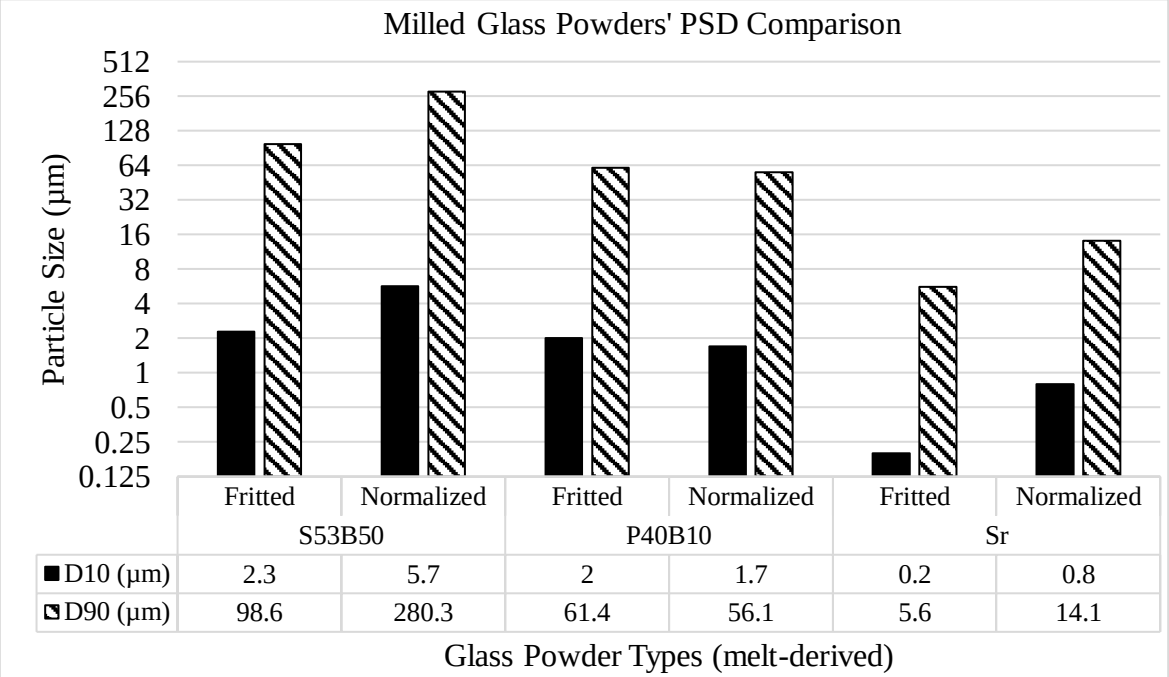

Figure 5-3: Comparing Fritted and Normalized Glass Powder Particle Size Distribution.

samples. In contrast, the Sr powders showed the most significant size reduction upon normalization. These observations align with the literature that reports the PSD as a crucial factor in scaffold synthesis, influencing mechanical strength and bioactivity (Reiter *et al.*, 2019).

The FTIR analysis of bioactive glass reveals distinct characteristic peaks, indicative of their crystalline phases and bonding configurations. For instance, smaller peaks at 500 and 1000 cm^{-1} in bioactive glass are identified as symmetric stretching vibrations of a Si-O-Si crystalline phase, suggesting the presence of silicate networks. These IR spectra also show sharp peaks representing well-crystallized phases in materials like Hench Bioglass® (Ouis, Abdelghany and Elbatal, 2012). The FTIR analysis peaks, along with their potential assignments based on existing scientific literature, are summarized in the following table:

Table 5-1: FTIR Wavelength (cm^{-1}) Peak List and Bond Vibration Assignments of Control and Synthesized Compositions.

Sample	Peak (cm^{-1})	Possible Assignment
Zeolite Bioactive Glass (BG)	3534, 3051, 2409, 1938, 1514, 978, 737	OH stretching, Si-O-Si stretching, Carbonate groups, Si-O-Si or Si-OH bending, Si-O stretching
Powder A S53B50	3440, 2980, 2380, 1974, 1561, 1155,	OH stretching, C-H stretching, Si-O-Si bending and stretching, B-O stretching
Powder B P40B10	3434, 2827, 2191, 1920 to 1920	OH stretching, C-H stretching, C≡C or B-O-P linkages, Various bending and stretching vibrations
Powder C Sr	3322, 2856, 2003, 1502	OH stretching, C-H stretching, Multiple bond stretching and P-O bond vibrations

The zeolite often has peaks indicating hydroxyl groups (OH), silicate structures, carbonate groups, and Si-O-Si or Si-OH groups. Peaks at 978 cm^{-1} and 737 cm^{-1} correspond to Si-O stretching vibrations. S53B50 has peaks indicating OH stretching vibrations and B-O stretching vibrations. Peaks at 2380 cm^{-1} and 1974 cm^{-1} could be due to graphite or other carbonates, and peaks at 1561 cm^{-1} and 1155 cm^{-1} are likely due to Si-O-Si bending and stretching vibrations. P40B10 has peaks indicating OH stretching and B-O-P stretching vibrations. The peak at 2191 cm^{-1} might be due to carbon-carbon triple bonds or carbon-nitrogen triple bonds likely from graphite. The fingerprint region shows various bending and stretching vibrations. Powder C Sr has peaks indicating OH stretching and C-H stretching vibrations. The absorption peaks at 2003 cm^{-1} and 1502 cm^{-1} could involve phosphates or other inorganic groups. Studies like those by Arango-Ospina et al. suggest the bioactive behaviour of scaffolds, as evidenced by HCA formation detected through FTIR spectroscopy. Additionally, Serra's research on bonding configurations in bioactive silica-based materials, using FTIR and XPS studies, provides insight into the presence of non-bridging silicon-oxygen bonds (Serra *et al.*, 2003).

5.1.2 Analysis of Porosity

The porosity analysis of scaffold specimens highlights the relationship between density, and porosity. From Table 4-14 in the results, it is evident that the porosity of the scaffolds varies directly with the bulk densities of glasses measured after synthesis in Figure 5-4.

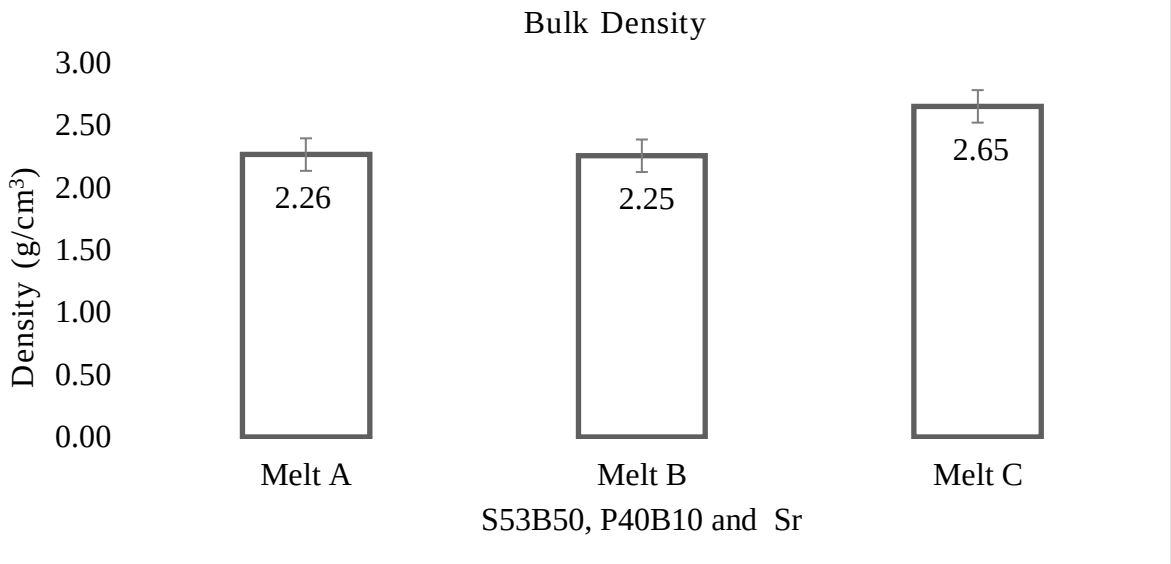

Figure 5-4: Bulk Densities of The Solid Ingots Measured After Cooling, Used as D_{th} to Calculate Porosity.

For S53B50, an average density of 2.26 ±0.12 g/cm³ was found, which correlated with the porosity values observed, particularly after sintering at 610°C, which showed a porosity of 54.0%. P40B10 scaffolds had a higher average density of 2.65 ±0.44 g/cm³, with a porosity of 54.2% at 600°C, indicating a denser yet similarly porous structure. The Sr scaffolds, with an average density of 2.25 ±0.28 g/cm³, demonstrated a higher porosity of 57.7% at 520°C, suggesting a more open and interconnected structure conducive to tissue integration, a finding echoed in the literature for bioactive glass scaffolds doped with SrO (Zhao *et al.*, 2021). Additionally, the observed S53B50, P40B10 and Sr glass densities are like respective values of 2.35 g/cm³, 2.58 g/cm³ and 2.30 g/cm³ theoretical densities reported by Erasmus *et al.*, (2018), who has studied the same material compositions.

The quantitative measurements of porosity using FIJI ImageJ software, as reported in Table 4-15, provides additional insights into the pore size range, average pore size, and total porous

area of the scaffolds. Specifically, the scaffold labelled “P40B10 - 600°C” shows the largest average pore size of 617 µm, and the highest porous fraction, nearing 50%. This suggests that as the average pore size increases, the porous fraction also tends to increase, which could be due to the larger pores contributing to a greater overall void space within the scaffold material. On the other hand, the scaffold labelled “Sr - 520°C” has a smaller average pore size and a correspondingly lower porous fraction, which is around 37.7%. This indicates that smaller pore sizes are associated with a lower porous fraction, likely because smaller pores occupy less volume, resulting in a denser scaffold structure with less void space.

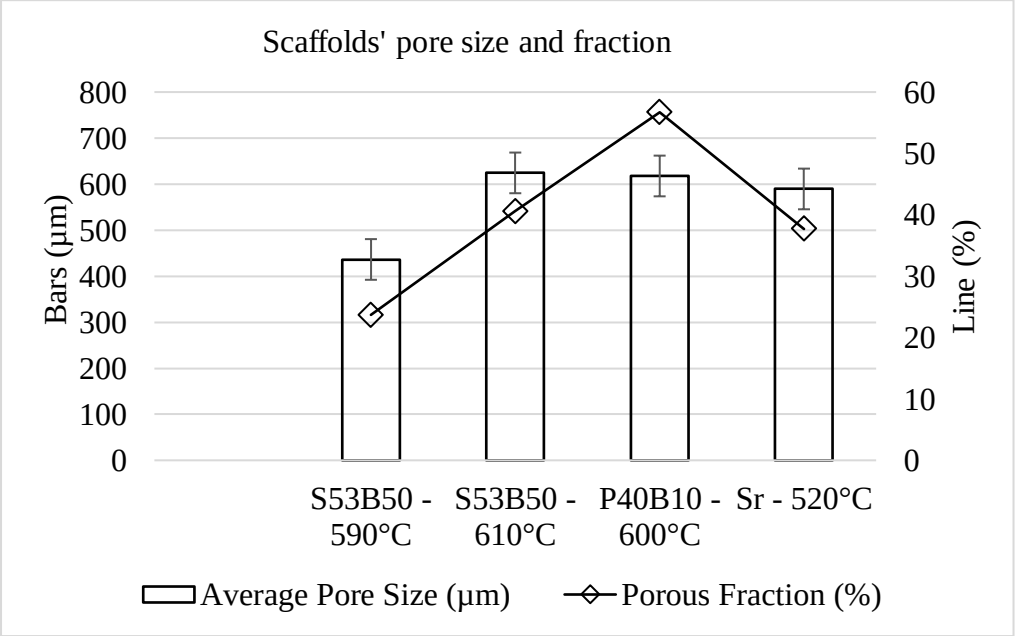

Figure 5-5: Porosity of Cross-Sectional Area of Various Scaffolds, Showing Pore Size and Fraction.

The S53B50 scaffold sintered at 610°C displayed an increased average pore size and porous fraction compared to the same composition sintered at 590°C. The porosity of the scaffolds, as indicated by the average pore size and porous fraction, is directly related to the objectives of the study outlined on preparation of highly porous scaffolds. The average pore size and porous fraction are key indicators of the level of porosity achieved in the scaffolds. The data shows that different sintering temperatures result in varying degrees of porosity, which is essential for preparing scaffolds with the desired level of porosity

5.2 Analysis of Crystallinity

Increased sintering temperatures resulted in higher crystallinity indexes calculated from integrated XRD peak areas, indicating greater crystalline phase formation. Crystallinity indexes ranged from to 45 - 59%. For S53B50, the closest sintering temperatures reported are 590 °C and 610 °C. The crystallinity index at 590 °C is 47.44% and at 610 °C is 57.59%.

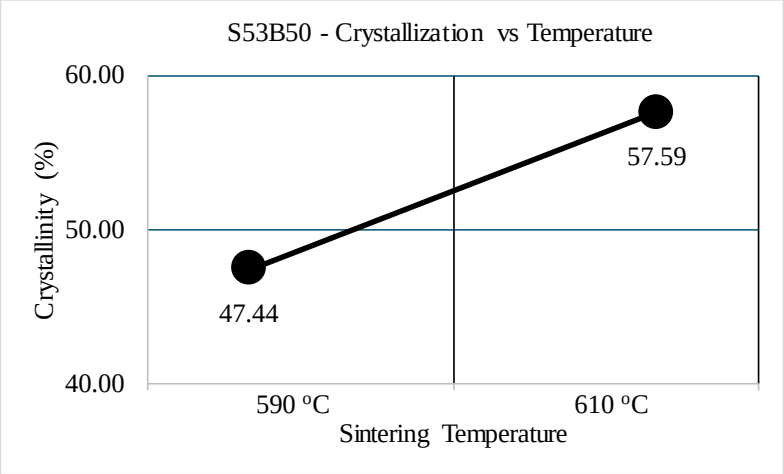

Figure 5-6: S53B50 Sintering Temperature and Crystallinity Index.

Since 590 °C is below 652 °C and the crystallinity index is below 50%, it supports the null hypothesis (H_0) that sintering below T_0 does not cause adverse crystallization of more than 50%. For P40B10, the closest sintering temperatures reported are 570 °C and 600 °C. The crystallinity index at 570 °C is 45.12% and at 600 °C is 57.06%.

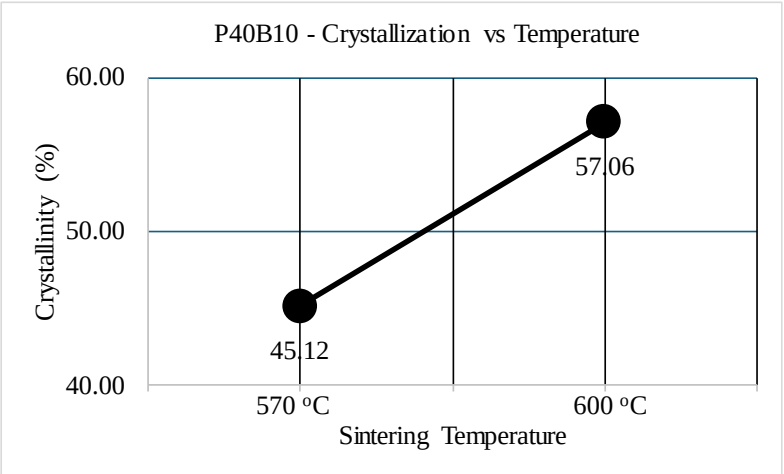

Figure 5-7: P40B10 Sintering Temperature and Crystallinity Index.

Since 570 °C is below 613 °C and the crystallinity index is below 50%, it also supports the null hypothesis (H_0). For Sr, the sintering temperatures reported are 490 °C and 520 °C. The crystallinity index at 490 °C is 59.58% and at 520 °C is 67.80%.

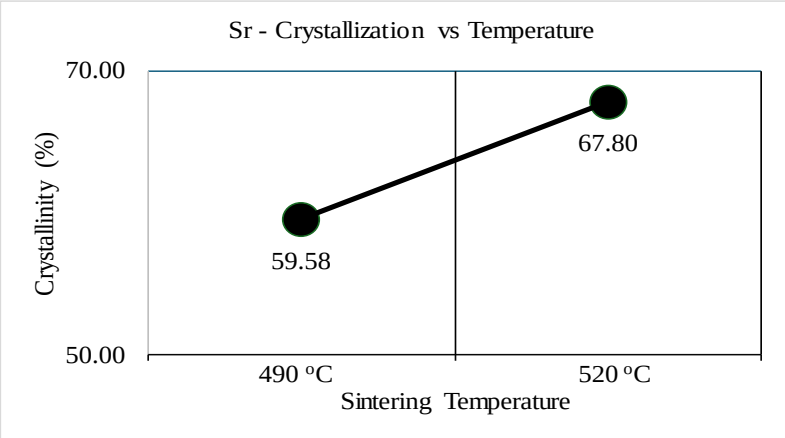

Figure 5-8: Sr Sintering Temperature and Crystallinity Index.

Although 520 ˚C is the sintering temperature 20 °C below T_0, the crystallinity index is well above 50%, which would support the alternative hypothesis (H_1) that sintering at this temperature does cause adverse crystallization of more than 50%.

These findings align with documented research, which supports the notion that higher temperatures can enhance the crystallization process of these materials (Erasmus *et al.*, 2017). The increase in temperature likely provides the energy necessary for the atoms or molecules to overcome activation barriers, enabling them to arrange into a more ordered crystalline structure. This is in line with the principles of thermodynamics and kinetic theory, which suggest that increased thermal energy can lead to increased atomic mobility, thereby facilitating the ordering process (Loh *et al.*, 2023).

5.3 Analysis of Mechanical Properties

5.3.1 Compression Load Bearing Analysis

Compression testing revealed increasing compressive strength but decreasing extension with higher sintering temperatures. S53B50 at 610°C withstood the highest load of 1.7MPa from the porous scaffold. The graph in Figure 5-9 of compressive stress versus compressive extension for the different scaffolds, includes a less porous specimen labelled S53B50 No Porogen (Normalized). This specimen serves as a comparative baseline to highlight the effects of porosity on the mechanical properties of the materials. From the graph, it is evident that the less porous S53B50 specimen exhibits a much steeper initial slope, indicating a

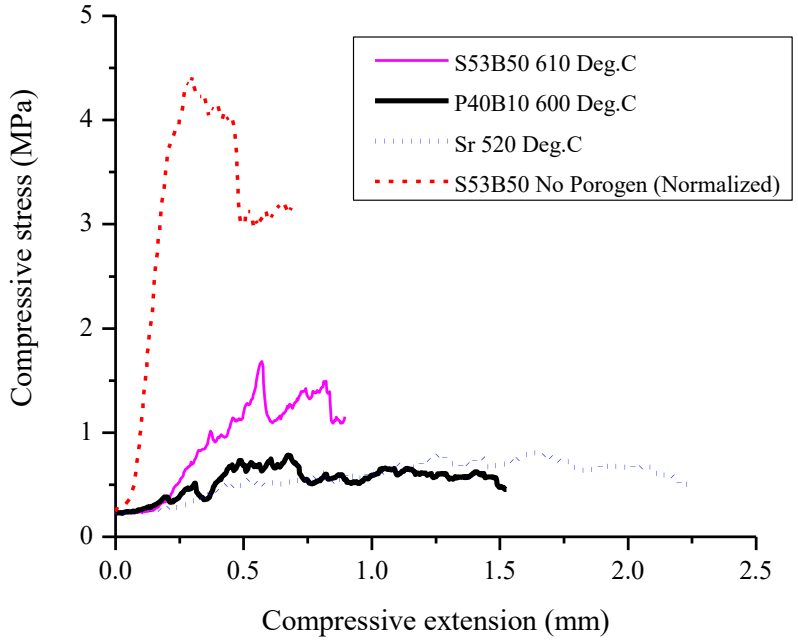

Figure 5-9: Scaffolds Compression Stress Diagram.

higher resistance to deformation, which is consistent with expectations that lower porosity generally leads to higher mechanical strength. This is due to the reduced presence of pores, which can act as stress concentrators and weaken the material under compressive loads. The normalized curve for the less porous S53B50 specimen peaks at a higher compressive stress value before a sharp drop, suggesting a brittle failure mode, which is typical for denser ceramics and materials with lower porosity. When comparing to commercial highly porous bioactive glass scaffolds designed to mimic trabecular bone, the results closely approach the

expected ranges. For instance, commercial scaffolds typically exhibit compressive strengths in the range of 2 to 3.5 MPa, like the natural trabecular bone (Fu *et al.*, 2013). This comparison indicates that the S53B50 scaffold approaches the lower end of this range, suggesting a promising performance in terms of mechanical robustness and potential application in bone tissue engineering.

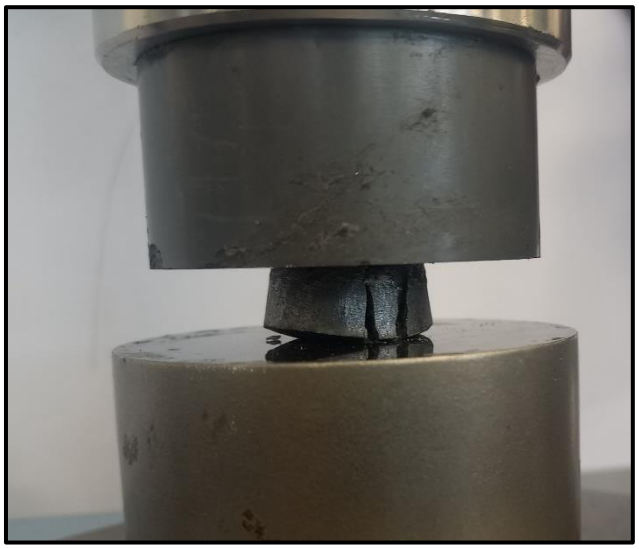

Figure 5-10: Cracks Propagating at Maximum Loading Stress of Porous Scaffolds.

In contrast, the other specimens with higher porosity, such as Sr sintered at 520°C and P40B10 sintered at 600°C, show a more gradual slope and lower peak stress values, indicating that they can absorb more deformation before crack propagation (Fig. 5-10).

This behaviour is indicative of materials that have a more ductile or plastic failure mode, which can be beneficial in applications where energy absorption is critical, such as in impact-resistant structures or biomedical implants that mimic the mechanical properties of bone.

5.3.2 Wear Resistance Analysis

The wear performance of materials is often correlated with their mechanical properties, such as hardness and toughness, which can be influenced by factors like porosity, grain size, and the presence of secondary phases. Lower porosity generally results in better wear resistance because there are fewer weak spots where material removal can initiate. The samples, Sr -

490°C, P40B10 - 600°C, and S53B50 - 590°C, show variability in wear rates and friction coefficients indicative of their tribological behaviour. Tribology testing found improved wear resistance and lower friction coefficients at higher loads for Sr-490°C and P40B10-600°C, but worsening performance for S53B50-590°C.For Sr - 490°C samples, increasing the standard load leads to a decrease in both the worn track area and the wear rate, suggesting an enhancement in compaction and wear resistance. This observation is coherent with the known densification behaviour of bioactive glasses under load, which improves their mechanical stability (Baino and Fiume, 2019).

The P40B10 - 600°C samples show a drastic decrease in wear track area and wear rate with increasing load, which could be attributed to the structural rearrangement and potential phase transformations that occur at higher temperatures and loads. The role of borosilicate glass, known for its thermal resistance and chemical durability contributes to this behaviour under tribological stress (Chakraborty *et al.*, 2023).

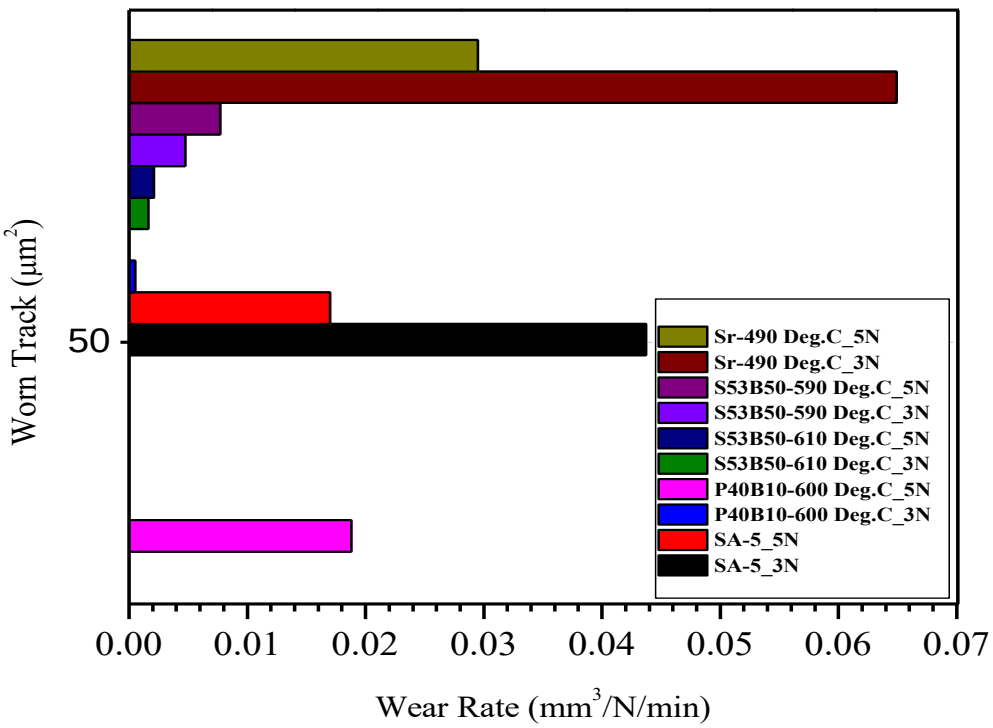

Figure 5-11: Wear of the Various Scaffolds Analysed at 3 and 5 N Standard Loading.

Conversely, the S53B50 - 590°C samples exhibited an increase in worn track area with increasing load, which could point towards a limit to the load-bearing capacity of this composition. The slight increase in the friction coefficient could also suggest alterations in the surface interactions under the tribological conditions (Prasad, 2017).

Comprehensive analysis using TGA, FTIR, XRD, SEM, and mechanical testing, characterized microstructural and mechanical properties of the as prepared scaffolds. Using NaCl as a pore-generating agent developed highly porous scaffolds, with pores covering up to 57 % of some of the observed surface areas. Higher sintering temperatures increased scaffold density, compressive strength, and crystallinity while decreasing porosity to as low as 54% in S53B50 formed at 610 °C. Objectives were successfully achieved demonstrating the ability to control scaffold properties for different applications via the sintering process. All scaffolds are unlikely to mechanically suffice as structural implants but should rather be applied in drug delivery use owing to low strength with the highest observation of 1.7 MPa.

CHAPTER 6: CONCLUSIONS AND RECOMMENDATIONS

This work on developing bioactive glass scaffolds for medical applications has demonstrated relevant findings in the field of biomaterials starting with a varying thermal stability and decomposition characteristics across the different compositions. Specifically, the S53B50 mainly composed of SiO_2 + B_2O_3, exhibited the most significant mass loss at higher temperature ranges from 600 °C to 900 °C, compared to the phosphate compositions, which decomposed at lower temperature ranges of 300-700 °C. The thermal characteristics for synthesis are as expected from literature with the borosilicate requiring a higher melting temperature of 1200 °C, because of the higher SiO_2 content. Additionally, fritting was found to yield more amorphous bioglass powders in comparison to casting a monolith then annealing.

Interconnected mesopore (130-1200 µm) morphologies are found in all sintered scaffolds using NaCl as a pore generator, indicative of support for trabecular bone growth ability. Crystallinity indexes rose with temperature, reflecting more crystalline phases: S53B50 showed 47.44 % at 590 °C to 57.59 % at 610 °C, and P40B10 had 45.12 % at 570 °C to 57.06 % at 600 °C. Higher temperatures shifted structures from amorphous to crystalline. For S53B50 and P40B10, crystallization stayed below 50 % at 590 °C and 570 °C, respectively, aligning with H_0. Conversely, Sr exceeded 50 % crystallization below T_0, stressing the critical role of sintering temperature on scaffold structure.

The mechanical strength of the scaffolds, as assessed by compression testing, showed that S53B50 had the highest strength of 1.7 MPa, whilst the Sr glass observed highest deformation of 1.62 mm at maximum loading. Therefore, the scaffolds produced are having low potential for load-bearing applications, however they are quite suitable for drug loading and delivery considerations. Tribological testing revealed that while Sr and P40B10 scaffolds improved performance under higher loads, S53B50's performance varied. This

variation in tribological behaviours underscores the need for further research into the wear properties of these materials for long-term implantation scenarios. To assess long-term biocompatibility and scaffold stability, a detailed corrosion study in SBF is suggested. This would provide valuable insights into the scaffold's degradation kinetics, ion release behaviour, and its impact on surrounding biological environments. In addition, an interdisciplinary collaborative approach is recommended to assess in vitro characteristics in the presence of cells and immune system inhibitors.

REFERENCES

Aalto-Setälä, L., Siekkinen, M., Lindfors, N. and Hupa, L., 2023. Dissolution of Glass–Ceramic Scaffolds of Bioactive Glasses 45S5 and S53P4. *Biomedical Materials & Devices*, pp.1-11.

Abdollahi, S., Paryab, A., Khalilifard, R., Anousheh, M. and Khachatourian, A.M., 2021. The Fabrication and Characterization of Bioactive Akermanite/Octacalcium Phosphate Glass-Ceramic Scaffolds Produced via PDC Method. *Ceramics International*, *47*(5), pp.6653-6662.

Adel, I.M., ElMeligy, M.F. and Elkasabgy, N.A., 2022. Conventional and Recent Trends of Scaffolds Fabrication: A Superior Mode for Tissue Engineering. *Pharmaceutics*, *14*(2), p.306.

Al-Harbi, N., Mohammed, H., Al-Hadeethi, Y., Bakry, A.S., Umar, A., Hussein, M.A., Abbassy, M.A., Vaidya, K.G., Al Berakdar, G., Mkawi, E.M. and Nune, M., 2021. Silica-Based Bioactive Glasses and Their Applications in Hard Tissue Regeneration: A Review. *Pharmaceuticals*, *14*(2), p.75.

Anand, A., Lalzawmliana, V., Kumar, V., Das, P., Devi, K.B., Maji, A.K., Kundu, B., Roy, M. and Nandi, S.K., 2019. Preparation and in vivo biocompatibility studies of different mesoporous bioactive glasses. *Journal of the Mechanical Behavior of Biomedical Materials*, *89*, pp.89-98.

Arango-Ospina, M. and Boccaccini, A.R., 2022. Bioactive Glasses and Ceramics for Tissue Engineering. In *Tissue Engineering Using Ceramics and Polymers* (pp. 111-178). Woodhead Publishing.

Araujo, M.S., Bartolomé, J.F. and Mello-Castanho, S., 2020. Tribological and Mechanical Behaviour Of 45S5 Bioglass®-Based Compositions Containing Alumina and Strontium. *Ceramics International*, *46*(15), pp.24347-24354.

Arcos, D. and Portolés, M.T., 2023. Mesoporous Bioactive Nanoparticles for Bone Tissue Applications. *International Journal of Molecular Sciences*, *24*(4), p.3249.

Arepalli, S.K., Tripathi, H., Manna, P.P., Pankaj, P., Krishnamurthy, S., Patne, S.C., Pyare, R. and Singh, S.P., 2019. Enhanced In Vivo Biocompatibility of Magnesia-Contained Bioactive Glasses. *Journal of the Australian Ceramic Society*, *55*, pp.337-342.

Azadani, R.N., Sabbagh, M., Salehi, H., Cheshmi, A., Raza, A., Kumari, B. and Erabi, G., 2021. Sol-gel: Uncomplicated, Routine and Affordable Synthesis Procedure for Utilization of Composites in Drug Delivery. *Journal of Composites and Compounds*, *3*(6), pp.57-70

Badiee, M., Nemati, N.H., Khorasani, M.T. and Shokrgozar, M.A., 2022. Highly Porous Bio-Glass Scaffolds Fabricated by Polyurethane Template Method with Hydrothermal Treatment for Tissue Engineering Uses. *Iranian Journal of Basic Medical Sciences*, *25*(12), p.1513.

Baino, F. and Fiume, E., 2019. Elastic Mechanical Properties of 45S5-Based Bioactive Glass–Ceramic Scaffolds. *Materials*, *12*(19), p.3244.

Baino, F., 2018. Bioactive Glasses–When Glass Science and Technology Meet Regenerative Medicine. *Ceramics International*, *44*(13), pp.14953-14966.

Baino, F., Barberi, J., Fiume, E., Orlygsson, G., Massera, J. and Verné, E., 2019. Robocasting of Bioactive SiO_2-P_2O_5-CaO-MgO-Na_2O-K_2O Glass Scaffolds. *Journal of Healthcare Engineering*, *2019*.

Baino, F., Ferraris, S., Miola, M., Verné, E., Evans, I. and Bretcanu, O., 2019. Multifunctional Bioactive Glasses and Glass-Ceramics: Beyond 'Traditional'Bioactivity. In *Biomedical, Therapeutic and Clinical Applications of Bioactive Glasses* (pp. 35-67). Woodhead Publishing.

Baino, F., Fiorilli, S. and Vitale-Brovarone, C., 2017. Composite Biomaterials Based on Sol-Gel Mesoporous Silicate Glasses: A review. *Bioengineering*, *4*(1), p.15.

Baino, F., Hamzehlou, S. and Kargozar, S., 2018. Bioactive Glasses: Where Are We and Where Are We Going? *Journal of Functional Biomaterials*, *9*(1), p.25.

Bellucci, D., Sola, A., Salvatori, R., Anesi, A., Chiarini, L. and Cannillo, V., 2014. Sol–gel Derived Bioactive Glasses with Low Tendency to Crystallize: Synthesis, Post-Sintering Bioactivity and Possible Application for The Production of Porous Scaffolds. *Materials Science and Engineering: C*, *43*, pp.573-586.

Bellucci, D., Veronesi, E., Dominici, M. and Cannillo, V., 2020. On The In Vitro Biocompatibility Testing of Bioactive Glasses. *Materials*, *13*(8), p.1816.

Ben-Arfa, B.A. and Pullar, R.C., 2020. A Comparison of Bioactive Glass Scaffolds Fabricated by Robocasting from Powders Made by Sol–Gel and Melt-Quenching Methods. *Processes*, *8*(5), p.615.

Bento, R., Gaddam, A. and Ferreira, J.M., 2021. Sol–Gel Synthesis and Characterization of a Quaternary Bioglass for Bone Regeneration and Tissue Engineering. *Materials*, *14*(16), p.4515.

Bohorquez-Moreno, C.D., Öksüz, K.E. and Dincer, E., 2023. Porous Polymer Scaffolds Derived from Bioresources for Biomedical Applications. *Cellulose Chemistry And Technology*, *57*(1-2), pp.107-116.

Bromet, B.A., Blackwell, N.P., Abokefa, N., Freudenberger, P., Blatt, R.L., Brow, R.K. and Semon, J.A., 2023. The Angiogenic Potential of pH-Neutral Borophosphate Bioactive Glasses. *Journal of Biomedical Materials Research Part A*.

Cannio, M., Bellucci, D., Roether, J.A., Boccaccini, D.N. and Cannillo, V., 2021. Bioactive Glass Applications: A Literature Review of Human Clinical Trials. Materials 2021, 14, 5440.

Chakraborty, A., Prasad, S., Kant, S., Vel, R., Tripathy, S., Sinha, P.K., Dey, K.K., Lodhi, L., Ghosh, M., Allu, A.R. and Bodhak, S., 2023. Thermally Stable Bioactive Borosilicate Glasses: Composition–Structure–Property Correlations. *Journal of Materials Research*, pp.1-17.

Che, L. *et al.* (2023) 'A biomimetic and bioactive scaffold with intelligently pulsatile teriparatide delivery for local and systemic osteoporosis regeneration', *Bioactive Materials*, 19, p. 75. Available at: https://doi.org/10.1016/j.bioactmat.2022.03.023.

Choi, W., Youngseok, K. and Choi, S., 2018. Glass Composition, Preparation Method of Coating Composition, And Cooking Appliance. *The Journal of Prosthetic Dentistry, 71(5), pp.453-461*.

Chyzy, A., Tomczykowa, M. and Plonska-Brzezinska, M.E., 2020. Hydrogels As Potential Nano-, Micro-and Macro-Scale Systems for Controlled Drug Delivery. *Materials*, *13*(1), p.188

Cyster, L.A., Grant, D.M., Howdle, S.M., Rose, F.R.A.J., Irvine, D.J., Freeman, D., Scotchford, C.A. and Shakesheff, K.M., 2005. The Influence of Dispersant Concentration on The Pore Morphology of Hydroxyapatite Ceramics for Bone Tissue Engineering. *Biomaterials*, *26*(7), pp.697-702.

da Silva, G.L., Rodrigues, I.F., Pereira, S.S.S., Fontoura, G.M.G., Reis, A.S., Pedrochi, F. and Steimacher, A., 2022. Bioactive Antibacterial Borate Glass and Glass-Ceramics. *Journal of Non-Crystalline Solids*, *595*, p.121829.

El-Ghannam, A., Hamazawy, E. and Yehia, A., 2001. Effect of Thermal Treatment on Bioactive Glass Microstructure, Corrosion Behavior, ζ Potential, and Protein Adsorption. *Journal of Biomedical Materials Research: An Official Journal of The Society for Biomaterials, The Japanese Society for Biomaterials, and The Australian Society for Biomaterials and the Korean Society for Biomaterials*, *55*(3), pp.387-395.

Elsayed, H., Colombo, P., Crovace, M.C., Zanotto, E.D. and Bernardo, E., 2021. Suitability of Biosilicate® Glass-Ceramic Powder for Additive Manufacturing of Highly Porous Scaffolds. *Ceramics International*, *47*(6), pp.8200-8207.

Ensoylu, M., Deliormanlı, A.M. and Atmaca, H., 2022. Preparation, Characterization, and Drug Delivery of Hexagonal Boron Nitride-Borate Bioactive Glass Biomimetic Scaffolds for Bone Tissue Engineering. *Biomimetics*, *8*(1), p.10.

Erasmus, E.P., Johnson, O.T., Sigalas, I. and Massera, J., 2017. Effects of Sintering Temperature on Crystallization and Fabrication of Porous Bioactive Glass Scaffolds for Bone Regeneration. *Scientific Reports*, *7*(1), p.6046.

Essien, E.R., Adams, L.A., Shaibu, R.O., Olasupo, I.A. and Oki, A., 2012. Economic route to sodium-containing silicate bioactive glass scaffold. *Open Journal of Regenerative Medicine*, *1*(03), pp.33-40.

Filho, O.P., La Torre, G.P. and Hench, L.L., 1996. Effect of Crystallization on Apatite-Layer Formation of Bioactive Glass 45S5. *Journal of Biomedical Materials Research: An Official Journal of The Society for Biomaterials and The Japanese Society for Biomaterials*, *30*(4), pp.509-514.

Fiume, E., Ciavattini, S., Verné, E. and Baino, F., 2021. Foam Replica Method In The Manufacturing Of Bioactive Glass Scaffolds: Out-of-Date Technology or Still Underexploited Potential? *Materials*, *14*(11), p.2795.

Fiume, E., Serino, G., Bignardi, C., Verné, E. and Baino, F., 2020. Sintering Behavior of a Six-Oxide Silicate Bioactive Glass for Scaffold Manufacturing. *Applied Sciences*, *10*(22), p.8279.

Flint, L.E. and Flint, A.L., 2002. 2.3 Porosity. *Methods of Soil Analysis: Part 4 Physical Methods*, *5*, pp.241-254.

Fu, Q., Beall, G.H. and Smith, C.M., 2017. Nature-Inspired Design of Strong, Tough Glass-Ceramics. *MRS Bulletin*, *42*(3), pp.220-225.

Fu, Q., Saiz, E., Rahaman, M.N. and Tomsia, A.P., 2011. Bioactive Glass Scaffolds for Bone Tissue Engineering: State of The Art and Future Perspectives. *Materials Science and Engineering: C*, *31*(7), pp.1245-1256.

Fu, Q., Saiz, E., Rahaman, M.N. and Tomsia, A.P., 2013. Toward Strong and Tough Glass and Ceramic Scaffolds for Bone Repair. *Advanced Functional Materials, 23*(44), pp.5461-5476.

Gavinho, S.R., Prezas, P.R., Ramos, D.J., Sá-Nogueira, I., Borges, J.P., Lança, M.C., Silva, J.C., Henriques, C.M., Pires, E., Kumar, J.S. and Graça, M.P.F., 2019. Nontoxic Glasses: Preparation, Structural, Electrical and Biological Properties. *International Journal of Applied Ceramic Technology*, *16*(5), pp.1885-1894.

Gerhardt, L.C. and Boccaccini, A.R., 2010. Bioactive Glass and Glass-Ceramic Scaffolds for Bone Tissue Engineering. *Materials*, *3*(7), pp.3867-3910.

Gharbi, A., Oudadesse, H., El Feki, H., Cheikhrouhou-Koubaa, W., Chatzistavrou, X., V. Rau, J., Heinämäki, J., Antoniac, I., Ashammakhi, N. and Derbel, N., 2023. High Boron Content Enhances Bioactive Glass Biodegradation. *Journal of Functional Biomaterials*, *14*(7), p.364.

Gomes, A.D., dos Santos, D.M., Dumont, M.R., Houmard, M., de Oliveira, A.A. and Nunes, E.H., 2023. Preparation of Hydroxyapatite/Bioactive Glass/Collagen Scaffolds for Use In Tissue Engineering. *Journal of Non-Crystalline Solids*, *616*, p.122492.

Goncalves, A.D., Balestri, W. and Reinwald, Y., 2020. Biomedical implants for regenerative therapies. *Biomaterials*, pp.1-36.

González González, A., Rivas Santana, M., Zambrano Robledo, P.D.C. and Quiza, R., 2022. Thermal and Morphological Characterization of 3D-Printed PLA Scaffolds for Biomedical Applications. *MRS Advances*, *7*(35), pp.1206-1211.

Guduric, V., Wieckhusen, J., Bernhardt, A., Ahlfeld, T., Lode, A., Wu, C. and Gelinsky, M., 2022. Composite Bioinks with Mesoporous Bioactive Glasses—A Critical Evaluation of Results Obtained by In Vitro Experiments. *Frontiers in Bioengineering and Biotechnology*, *9*, p.767256.

Haque, J., Munna, A.H., Ayon, A.S.R., Shaitee, Z.R. and Saha, A., 2020. A Comprehensive Overview of the Pertinence and Possibilities of Bioactive Glass in the Modern Biological World. *Journal of Biomaterials*, *4*(2), pp.23-38.

Hatton, Jonathan, Graham Roy Davis, Abdel-Hamid I. Mourad, Nizamudeen Cherupurakal, Robert G. Hill, and Sahar Mohsin. Fabrication of Porous Bone Scaffolds Using Alginate and Bioactive Glass. *Journal of functional biomaterials* 10, no. 1 (2019): 15.

Hench, L.L., 1991. Bioceramics: From Concept to Clinic. *Journal of the American Ceramic Society*, *74*(7), pp.1487-1510.

Hench, L.L., 2006. The Story of Bioglass®. *Journal of Materials Science: Materials in Medicine*, *17*(11), pp.967-978.

Hench, L.L., 2013. Chronology of Bioactive Glass Development and Clinical Applications, *New Journal of Glass and Ceramics*, 03(02), pp. 67–73.

Hench, L.L., 2015. Opening Paper 2015-Some Comments on Bioglass: Four Eras of Discovery and Development. *Biomedical glasses*, *1*(1).

Hua, S.B., Su, J., Deng, Z.L., Wu, J.M., Cheng, L.J., Yuan, X., Chen, F., Zhu, H., Qi, D.H., Xiao, J. and Shi, Y.S., 2021. Microstructures and Properties of 45S5 Bioglass® & BCP Bioceramic Scaffolds Fabricated by Digital Light Processing. *Additive Manufacturing*, *45*, p.102074.

Hung, G.Y., Chen, P.Y., Wang, C.Y., Tu, C.S., Chen, C.S., Lai, P.L. and Feng, K.C., 2023. Tailoring Bioactive and Mechanical Properties in Polycrystalline Cao–SiO_2–P_2O_5 Glass-Ceramics. *Ceramics International*, *49*(5), pp.7289-7298.

Hyunh, N.B., Palma, C.S.D., Rahikainen, R., Mishra, A., Azizi, L., Verne, E., Ferraris, S., Hytonen, V.P., Sanches Ribeiro, A. and Massera, J., 2021. Surface Modification of Bioresorbable Phosphate Glasses for Controlled Protein Adsorption. *ACS Biomaterials Science & Engineering*, *7*(9), pp.4483-4493.

Jain, S., Gujjala, R., Azeem, P.A., Ojha, S. and Samudrala, R.K., 2022. A Review on Mechanical and In-Vitro Studies of Polymer Reinforced Bioactive Glass-Scaffolds and Their Fabrication Techniques. *Ceramics International*, *48*(5), pp.5908-5921.

Jang, J.W., Min, K.E., Kim, C., Shin, J., Lee, J. and Yi, S., 2023. Scaffold Characteristics, Fabrication Methods, and Biomaterials for the Bone Tissue Engineering. International Journal of Precision Engineering and Manufacturing, 24(3), pp.511-529.

Jeyachandran, D. and Cerruti, M., 2023. Glass, Ceramic, Polymeric, and Composite Scaffolds with Multiscale Porosity for Bone Tissue Engineering. *Advanced Engineering Materials*, *25*(17), p.2201743.

Jones, J.R., 2013. Review Of Bioactive Glass: From Hench to Hybrids. *Acta Biomaterialia*, *9*(1), pp.4457-4486.

Jones, J.R., Brauer, D.S., Hupa, L. and Greenspan, D.C., 2016. Bioglass and Bioactive Glasses and Their Impact on Healthcare. *International Journal of Applied Glass Science*, *7*(4), pp.423-434.

Jones, J.R., Lin, S., Yue, S., Lee, P.D., Hanna, J.V., Smith, M.E. and Newport, R.J., 2010. Bioactive Glass Scaffolds for Bone Regeneration and Their Hierarchical Characterisation. *Proceedings of the Institution of Mechanical Engineers, Part H: Journal of Engineering in Medicine*, *224*(12), pp.1373-1387.

Kamboj, N., Ressler, A. and Hussainova, I., 2021. Bioactive Ceramic Scaffolds for Bone Tissue Engineering by Powder Bed Selective Laser Processing: A Review. *Materials*, *14*(18), p.5338.

Kaou, M.H., Furkó, M., Balázsi, K. and Balázsi, C., 2023. Advanced Bioactive Glasses: The Newest Achievements and Breakthroughs In The Area. *Nanomaterials*, *13*(16), p.2287.

Kargozar, S., Baino, F., Hamzehlou, S., Hill, R.G. and Mozafari, M., 2018a. Bioactive Glasses Entering the Mainstream. *Drug Discovery Today*, *23*(10), pp.1700-1704.

Kargozar, S., Baino, F., Hamzehlou, S., Hill, R.G. and Mozafari, M., 2018b. Bioactive Glasses: Sprouting Angiogenesis in Tissue Engineering. *Trends In Biotechnology*, *36*(4), pp.430-444.

Kargozar, S., Montazerian, M., Fiume, E. and Baino, F., 2019. Multiple and Promising Applications of Strontium (Sr)-Containing Bioactive Glasses In Bone Tissue Engineering. *Frontiers In Bioengineering and Biotechnology*, *7*, p.161.

Kargozar, S., Mozafari, M., Hill, R.G., Milan, P.B., Joghataei, M.T., Hamzehlou, S. and Baino, F., 2018. Synergistic Combination of Bioactive Glasses and Polymers for Enhanced Bone Tissue Regeneration. *Materials Today: Proceedings*, *5*(7), pp.15532-15539.

Kaur, G., Kumar, V., Baino, F., Mauro, J.C., Pickrell, G., Evans, I. and Bretcanu, O., 2019. Mechanical Properties of Bioactive Glasses, Ceramics, Glass-Ceramics and Composites:

State-Of-The-Art Review and Future Challenges. *Materials Science and Engineering: C*, *104*, p.109895.

Kaur, G., Pandey, O.P., Singh, K., Homa, D., Scott, B. and Pickrell, G., 2014. A Review of Bioactive Glasses: Their Structure, Properties, Fabrication And Apatite Formation. *Journal of Biomedical Materials Research Part A: An Official Journal of The Society for Biomaterials, The Japanese Society for Biomaterials, and The Australian Society for Biomaterials and the Korean Society for Biomaterials*, *102*(1), pp.254-274.

Khurshid, Z., Husain, S., Alotaibi, H., Rehman, R., Zafar, M.S., Farooq, I. and Khan, A.S., 2019. Novel techniques of scaffold fabrication for bioactive glasses. In Biomedical, Therapeutic and Clinical Applications of Bioactive Glasses (pp. 497-519). Woodhead Publishing.

Kim, C.Y., Clark, A.E. and Hench, L.L., 1989. Early Stages of Calcium-Phosphate Layer Formation in Bioglasses. *Journal of Non-Crystalline Solids*, *113*(2-3), pp.195-202.

Knowles, J.C., 2003. Phosphate Based Glasses for Biomedical Applications. *Journal of Materials Chemistry*, *13*(10), pp.2395-2401.

Kokubo, T. and Yamaguchi, S., 2016. Novel Bioactive Materials Derived by Bioglass: Glass-Ceramic A-W and Surface-Modified Ti Metal. *International Journal of Applied Glass Science*, *7*(2), pp.173-182.

Kurkjian, C.R. and Prindle, W.R., 1998. Perspectives On the History of Glass Composition. *Journal of the American Ceramic Society*, *81*(4), pp.795-813.

Lara-Ochoa, S., Ortega-Lara, W. and Guerrero-Beltrán, C.E., 2021. Hydroxyapatite Nanoparticles in Drug Delivery: Physiochemistry and Applications. *Pharmaceutics*, *13*(10), p.1642.

Leach, J.K., Kaigler, D., Wang, Z., Krebsbach, P.H. and Mooney, D.J., 2006. Coating of VEGF-Releasing Scaffolds with Bioactive Glass for Angiogenesis and Bone Regeneration. *Biomaterials*, *27*(17), pp.3249-3255.

Lee, N.K., Cho, S. and Kim, I.S., 2022. Ferritin–A Multifaceted Protein Scaffold for Biotherapeutics. *Experimental and Molecular Medicine*, *54*(10), pp.1652-1657.

Lemos, E.M., Patrício, P.S. and Pereira, M.M., 2016. 3D Nanocomposite Chitosan/Bioactive Glass Scaffolds Obtained Using Two Different Routes: An Evaluation of The Porous Structure and Mechanical Properties. *Química Nova*, *39*, pp.462-466.

Leonardi, E., Ciapetti, G., Baldini, N., Novajra, G., Verné, E., Baino, F. and Vitale-Brovarone, C., 2010. Response of Human Bone Marrow Stromal Cells to A Resorbable P_2O_5–SiO_2–Cao–MgO–Na_2O–K_2O Phosphate Glass Ceramic for Tissue Engineering Applications. *Acta Biomaterialia*, *6*(2), pp.598-606.

Li, H., Wu, Z., Zhou, Y. and Chang, J., 2019. Bioglass For Skin Regeneration. In *Biomaterials for Skin Repair and Regeneration* (pp. 225-250). Woodhead Publishing.

Li, W., Cheng, X., Wang, Y. and Wang, S., 2021. Projection Printing of Scaffolds with Shape Recovery Capacity and Simultaneously Improved Stiffness and Toughness Using An Ultra-Fast Curing Poly (Propylene Fumarate)/Hyperbranched Additive Resin. *Additive Manufacturing*, *48*, p.102446.

Liang, W., Wu, X., Dong, Y., Shao, R., Chen, X., Zhou, P. and Xu, F., 2021. In Vivo Behavior of Bioactive Glass-Based Composites in Animal Models for Bone Regeneration. *Biomaterials Science*, *9*(6), pp.1924-1944.

Lin, K., Chang, J., Liu, Z., Zeng, Y. and Shen, R., 2009. Fabrication and Characterization of 45S5 Bioglass Reinforced Macroporous Calcium Silicate Bioceramics. *Journal of the European Ceramic Society*, *29*(14), pp.2937-2943.

Liu, X., Pan, H., Fu, H., Fu, Q., Rahaman, M.N. and Huang, W., 2010. Conversion of Borate-Based Glass Scaffold to Hydroxyapatite in A Dilute Phosphate Solution. *Biomedical Materials*, *5*(1), p.015005.

Liu, X., Rahaman, M.N., Fu, Q. and Tomsia, A.P., 2012. Porous and Strong Bioactive Glass (13-93) Scaffolds Prepared by Unidirectional Freezing of Camphene-Based Suspensions. *Acta Biomaterialia*, *8*(1), pp.415-423.

Loh, Z.W., Zaid, M.H.M., Matori, K.A., Kechik, M.M.A., Fen, Y.W., Mayzan, M.Z.H., Liza, S. and Cheong, W.M., 2023. Phase Transformation and Mechanical Properties of New Bioactive Glass-Ceramics Derived from $CaO–P_2O_5–Na_2O–B_2O_3–SiO_2$ Glass System. *Journal of the Mechanical Behavior of Biomedical Materials*, *143*, p.10588

Lu, J., Wang, Z., Zhao, Z., Song, W., Yu, H. and Chen, C., 2022, April. The Application of 3D Printing Technology in Fabrication of Calcium Phosphate-based Biomaterials for Bone Repairment. In *Proceedings of the 12th International Conference on Biomedical Engineering and Technology* (pp. 219-223).

Mannana, A., Kazmia, K.R., Khan, I.H. and Khan, M.S., 2006. A Method for The Determination of Relative Crystallinity of Minerals by X-Ray Diffraction. *Biological Sciences-PJSIR*, *49*(2), pp.72-76.

Mansour, A., Romani, M., Acharya, A.B., Rahman, B., Verron, E. and Badran, Z., 2023. Drug Delivery Systems in Regenerative Medicine: An Updated Review. *Pharmaceutics*, *15*(2), p.695.

Martelli, A., Bellucci, D. and Cannillo, V., 2023. Additive Manufacturing of Polymer/Bioactive Glass Scaffolds for Regenerative Medicine: A Review. *Polymers*, *15*(11), p.2473.

Massera, J., 2020. Bioactive Glass-Ceramics: From macro to nano. In *Nanostructured Biomaterials for Regenerative Medicine* (pp. 275-292). Woodhead Publishing.

Me, B., Mh, S. and Bagheri, R., 2015. Bioactive Glasses in Dentistry: A Review. *Journal of Dental Biomaterials*, 22.

Mecca, F.G., Bellucci, D. and Cannillo, V., 2023. Effect of Thermal Treatments and Ion Substitution on Sintering and Crystallization of Bioactive Glasses: A Review. *Materials*, *16*(13), p.4651.

Migneco, C., Fiume, E., Verné, E. and Baino, F., 2020. A Guided Walk Through the World of Mesoporous Bioactive Glasses (MBGs): Fundamentals, Processing, and Applications. *Nanomaterials*, *10*(12), p.2571.

Monmaturapoj, N., Uanlee, T., Nampuksa, K., Kasiwat, A. and Makornpan, C., 2022. Preparation and Properties of Porous Biphasic Calcium Phosphate/Bioactive Glass Composite Scaffolds for Biomedical Applications. *Materials Today Communications*, *33*, p.104993.

Montazerian, M., Shearer, A. and Mauro, J.C., 2024. Perspectives on the Impact Of Crystallization in Bioactive Glasses and Glass-Ceramics. International Journal of Ceramic Engineering & Science, 6(1), p.e10194.

Muñoz, F. and Sánchez-Muñoz, L., 2019. The Glass-Forming Ability Explained from Local Structural Differences by NMR Between Glasses and Crystals in Alkali Metaphosphates. *Journal of Non-Crystalline Solids*, *503*, pp.94-97.

Nandi, S.K., Kundu, B. and Datta, S., 2011. Development and Applications of Varieties of Bioactive Glass Compositions in Dental Surgery, Third Generation Tissue Engineering, Orthopaedic Surgery and as Drug Delivery System. *Biomaterials Applications for Nanomedicine*, *4*, pp.69-116.

Nandi, S.K., Mahato, A., Kundu, B. and Mukherjee, P., 2016. Doped Bioactive Glass Materials in Bone Regeneration. *Advanced Techniques in Bone Regeneration*, *10*, p.63266.

Olăreț, E., Stancu, I.C., Iovu, H. and Serafim, A., 2021. Computed Tomography as A Characterization Tool for Engineered Scaffolds with Biomedical Applications. *Materials*, *14*(22), p.6763.

Oonishi, H., Hench, L.L., Wilson, J., Sugihara, F., Tsuji, E., Kushitani, S. and Iwaki, H., 1999. Comparative Bone Growth Behaviour in Granules of Bioceramic Materials of Various Sizes. *Journal of Biomedical Materials Research: An Official Journal of The Society for Biomaterials, The Japanese Society for Biomaterials, and the Australian Society for Biomaterials*, *44*(1), pp.31-43.

Oonishi, H., Hench, L.L., Wilson, J., Sugihara, F., Tsuji, E., Matsuura, M., Kin, S., Yamamoto, T. and Mizokawa, S., 2000. Quantitative Comparison of Bone Growth Behaviour In Granules of Bioglass®, A-W Glass-Ceramic, and Hydroxyapatite. *Journal of*

Biomedical Materials Research: An Official Journal of The Society for Biomaterials, The Japanese Society for Biomaterials, and The Australian Society for Biomaterials and the Korean Society for Biomaterials, *51*(1), pp.37-46.

Ouis, M.A., Abdelghany, A.M. and ElBatal, H.A., 2012. Corrosion Mechanism and Bioactivity of Borate Glasses Analogue to Hench's Bioglass. *Processing and Application of Ceramics*, *6*(3), pp.141-149.

Park, J.H., Jo, S.B., Lee, J.H., Lee, H.H., Knowles, J.C. and Kim, H.W., 2023. Materials and Extracellular Matrix Rigidity Highlighted in Tissue Damages and Diseases: Implication for Biomaterials Design and Therapeutic Targets. *Bioactive Materials*, *20*, pp.381-403

Prasad, S., Vyas, V.K., Ershad, M. and Pyare, R., 2017. Crystallization and Mechanical Properties of (45S5-HA) Biocomposite for Biomedical Implantation.

Qi, X., Wang, H., Zhang, Y., Pang, L., Xiao, W., Jia, W., Zhao, S., Wang, D., Huang, W. and Wang, Q., 2018. Mesoporous Bioactive Glass-Coated 3D Printed Borosilicate Bioactive Glass Scaffolds for Improving Repair of Bone Defects. *International Journal of Biological Sciences*, *14*(4), p.471.

Rahaman, M.N., Day, D.E., Bal, B.S., Fu, Q., Jung, S.B., Bonewald, L.F. and Tomsia, A.P., 2011. Bioactive Glass in Tissue Engineering. *Acta Biomaterialia*, *7*(6), pp.2355-2373.

Rahmati, M. and Mozafari, M., 2019. Selective Contribution of Bioactive Glasses to Molecular and Cellular Pathways. *ACS Biomaterials Science & Engineering*, *6*(1), pp.4-20.

Rainer, A., Giannitelli, S.M., Abbruzzese, F., Traversa, E., Licoccia, S. and Trombetta, M., 2008. Fabrication of Bioactive Glass–Ceramic Foams Mimicking Human Bone Portions for Regenerative Medicine. *Acta Biomaterialia*, *4*(2), pp.362-369.

Rana, T., Naeem, Z., Javaid, S., Sajid, N., Habib, A., Khan, M.I., Fatima, M. and Khan, A.Q., 2021. Hydrogels-A Novel Drug Delivery System. *Biomedical Journal of Scientific & Technical Research*, *33*(1), pp.25486-25498.

Rawlings, R.D., Wu, J.P. and Boccaccini, A.R., 2006. Glass-Ceramics: Their Production from Wastes—A Review. *Journal of materials science*, *41*, pp.733-761.

Reiter, T., Panick, T., Schuhladen, K., Roether, J.A., Hum, J. and Boccaccini, A.R., 2019. Bioactive Glass-Based Scaffolds Coated with Gelatin for The Sustained Release of Icariin. *Bioactive Materials*, *4*, pp.1-7

Ribeiro, V.P., Oliveira, J.M. and Reis, R.L., 2022. Tissue Engineered Biomaterials and Drug Delivery Systems. *Pharmaceutics*, *14*(12), p.2827.

Rousselle, S.D., Ramot, Y., Nyska, A. and Jackson, N.D., 2019. Pathology of Bioabsorbable Implants in Preclinical Studies. *Toxicologic Pathology*, *47*(3), pp.358-378.

Rubežić, M.Z., Krstić, A.B., Stanković, H.Z., Ljupković, R.B., Ranđelović, M.S. and Zarubica, A.R., 2020. Different Types of Biomaterials: Structure and Application: A Short Review. *Advanced Technologies*, *9*(1), pp.69-79.

Ruiz-Aguilar, C., 2023. Porous Phosphate-Based Bioactive Glass/B-TCP Scaffold for Tooth Remineralization. *Plos One*, *18*(5), p.e0284885.

Ruiz-Aguilar, C., Alcántara-Quintana, L.E., Aguilar-Reyes, E.A. and Olivares-Pinto, U., 2022. Fabrication, Characterization, and In Vitro Evaluation Of B-TCP/Zro2-Phosphate-Based Bioactive Glass Scaffolds for Bone Repair. *Boletín de La Sociedad Española de Cerámica y Vidrio*, *61*(3), pp.191-202.

Saravanakumar, B., Rajkumar, M. and Rajendran, V., 2011. Synthesis And Characterisation of Nanobioactive Glass for Biomedical Applications. *Materials Letters, 65*(1), pp.31-34.

Sarker, B., Hum, J., Nazhat, S.N. and Boccaccini, A.R., 2015. Combining Collagen and Bioactive Glasses for Bone Tissue Engineering: A Review. *Advanced Healthcare Materials*, *4*(2), Pp.176-194.

Sayre, E.V. and Smith, R.W., 1961. Compositional Categories of Ancient Glass. *Science*, *133*(3467), pp.1824-1826.

Schumacher, M., Habibovic, P. and Van Rijt, S., 2021. Mesoporous Bioactive Glass Composition Effects on Degradation and Bioactivity. *Bioactive Materials*, *6*(7), pp.1921-1931.

Sergi, R., Bellucci, D., Salvatori, R., Anesi, A. and Cannillo, V., 2020. A Novel Bioactive Glass Containing Therapeutic Ions with Enhanced Biocompatibility. *Materials, 13*(20), p.4600.

Serra, J., González, P., Liste, S., Serra, C., Chiussi, S., León, B., Pérez-Amor, M., Ylänen, H.O. and Hupa, M., 2003. FTIR and XPS Studies of Bioactive Silica Based Glasses. *Journal of Non-Crystalline Solids, 332*(1-3), pp.20-27.

Serva, A., Guerault, A., Ishii, Y., Gouillart, E., Burov, E. and Salanne, M., 2020. Structural and Dynamic Properties of Soda–Lime–Silica in The Liquid Phase. *The Journal of Chemical Physics, 153*(21).

Shafaghi, R., Rodriguez, O., Wren, A.W., Chiu, L., Schemitsch, E.H., Zalzal, P., Waldman, S.D., Papini, M. and Towler, M.R., 2021. In Vitro Evaluation of Novel Titania-Containing

Borate Bioactive Glass Scaffolds. *Journal of Biomedical Materials Research Part A*, *109*(2), pp.146-158.

Shah, F.A. and Czechowska, J., 2018. Bioactive Glass and Glass-Ceramic Scaffolds for Bone Tissue Engineering. In *Bioactive Glasses* (pp. 201-233). Woodhead Publishing.

Sharifi, E., Bigham, A., Yousefiasl, S., Trovato, M., Ghomi, M., Esmaeili, Y., Samadi, P., Zarrabi, A., Ashrafizadeh, M., Sharifi, S. and Sartorius, R., 2022. Mesoporous Bioactive Glasses in Cancer Diagnosis and Therapy: Stimuli-Responsive, Toxicity, Immunogenicity, and Clinical Translation. *Advanced Science*, *9*(2), p.2102678.

Silva, L.D., Puosso, F.C., Soares, V.O., Peitl Filho, O., do RF Sabino, S., Serbena, F.C., Crovace, M.C. and Zanotto, E.D., 2021. Two-Step Sinter-Crystallization of K_2O–CaO–P_2O_5–SiO_2 (45S5-K) Bioactive Glass. *Ceramics International*, *47*(13), pp.18720-18731.

Skallevold, H.E., Rokaya, D., Khurshid, Z. and Zafar, M.S., 2019. Bioactive Glass Applications in Dentistry. *International Journal of Molecular Sciences*, *20*(23), p.5960.

Souza, M.T., Renno, A.C.M., Peitl, O. and Zanotto, E.D., 2017. New Highly Bioactive Crystallization-Resistant Glass for Tissue Engineering Applications. *Translational Materials Research*, *4*(1), p.014002.

Stanić, V., 2017. Variation In Properties of Bioactive Glasses After Surface Modification. *Clinical Applications of Biomaterials: State-of-the-Art Progress, Trends, and Novel Approaches*, pp.35-63.

Staniewicz-Brudnik, B., Karolus, M., Cholewa-Kowalska, K., Skrabalak, G., Laszkiewicz-Łukasik, J., Drukała, J., Stalińska, J. and Dziedzic, K., 2022. Selected Physico-Chemical

Properties of Composite Scaffolds of Sintered Submicrocrystalline Corundum and Bioglass. *The International Journal of Advanced Manufacturing Technology*, *120*(3-4), pp.1867-1876.

Tainio, J., Paakinaho, K., Ahola, N., Hannula, M., Hyttinen, J., Kellomäki, M. and Massera, J., 2017. In Vitro Degradation of Borosilicate Bioactive Glass and Poly (L-Lactide-CO- ε-Caprolactone) Composite Scaffolds. *Materials*, *10*(11), p.1274.

Thananukul, K., Kaewsaneha, C., Opaprakasit, P., Lebaz, N., Errachid, A. and Elaissari, A., 2021. Smart Gating Porous Particles as New Carriers for Drug Delivery. *Advanced Drug Delivery Reviews*, *174*, pp.425-446.

Tian, X., Li, A., Li, S., Wang, X., Qu, Y., Zhao, F., Xu, Y., Yue, Y. and Kang, J., 2022. Crystallization Behavior and Mechanical Properties of High Strength Mica-Containing Glass-Ceramics from Granite Wastes. *Ceramics International*, *48*(16), pp.23119-23126.

Toosi, S., Naderi-Meshkin, H., Esmailzadeh, Z., Behravan, G., Ramakrishna, S. and Behravan, J., 2022. Bioactive Glass-Collagen/Poly (Glycolic Acid) Scaffold Nanoparticles Exhibit Improved Biological Properties and Enhance Osteogenic Lineage Differentiation of Mesenchymal Stem Cells. *Frontiers in Bioengineering and Biotechnology*, *10*, p.963996.

Tulyaganov, D.U., Fiume, E., Akbarov, A., Ziyadullaeva, N., Murtazaev, S., Rahdar, A., Massera, J., Verné, E. and Baino, F., 2022. In Vivo Evaluation of 3D-Printed Silica-Based Bioactive Glass Scaffolds for Bone Regeneration. *Journal of Functional Biomaterials*, *13*(2), p.74.

Tüncer, M., Yücesoy, D.T. and Öksel Karakuş, C., 2022. Green Synthesis of Nanostructured Bioactive Glass for Dental Applications. *Toxicology Letters*.

Vafa, E., Bazargan-Lari, R. and Bahrololoom, M.E., 2021. Synthesis Of 45S5 Bioactive Glass-Ceramic Using the Sol-Gel Method, Catalyzed by Low Concentration Acetic Acid Extracted from Homemade Vinegar. *Journal of Materials Research and Technology*, *10*, pp.1427-1436.

Valente, K.P., Brolo, A. and Suleman, A., 2020. From Dermal Patch to Implants—Applications of Biocomposites in Living Tissues. *Molecules*, *25*(3), p.50

van Gestel, N.A.P., Gabriels, F., van Rietbergen, B., Arts, J.J. and Hofmann, S., 2018. Mechanical Properties of Bioactive Glasses. In *Bioactive Glasses* (pp. 87-102). Woodhead Publishing.

Veeman, D., Sai, M.S., Sureshkumar, P., Jagadeesha, T., Natrayan, L., Ravichandran, M. and Mammo, W.D., 2021. Additive Manufacturing of Biopolymers for Tissue Engineering and Regenerative Medicine: An Overview, Potential Applications, Advancements, and Trends. *International Journal of Polymer Science*, *2021*, pp.1-20.

Veljović, D., Jokić, B., Petrović, R., Palcevskis, E., Dindune, A., Mihailescu, I.N. and Janaćković, D.J., 2009. Processing Of Dense Nanostructured HAP Ceramics by Sintering and Hot Pressing. *Ceramics International*, *35*(4), pp.1407-1413.

Wang, S. and Zhang, D., 2010. Biological Activity Evaluation of Porous HA Ceramics Using NH_4 HCO_3/PVA As Pore-Creating Agents. *Journal of Biomedical Engineering*, *27*(6), pp. 1280–1285.

Wu, C. and Chang, J., 2012. Mesoporous Bioactive Glasses: Structure Characteristics, Drug/Growth Factor Delivery and Bone Regeneration Application. *Interface Focus*, *2*(3), pp.292-306.

Wu, C. and Chang, J., 2014. Multifunctional Mesoporous Bioactive Glasses for Effective Delivery of Therapeutic Ions and Drug/Growth Factors. *Journal of Controlled Release*, *193*, pp.282-295.

Wu, C., Chang, J. and Xiao, Y., 2011. Mesoporous Bioactive Glasses as Drug Delivery and Bone Tissue Regeneration Platforms. *Therapeutic Delivery*, *2*(9), pp.1189-1198.

Wuersching, S.N., Högg, C., Kohl, L., Reichl, F.X., Hickel, R. and Kollmuss, M., 2023. Leaching Components and Initial Biocompatibility of Novel Bioactive Restorative Materials. *Dental Materials*, *39*(3), pp.293-304.

Yamaguchi, S., 2022. Borate Bioactive Glass. *Bioactive Glasses and Glass-Ceramics: Fundamentals and Applications*, pp.79-86.

Yao, H., Luo, J., Deng, Y., Li, Z. and Wei, J., 2022. Alginate-Modified Mesoporous Bioactive Glass and Its Drug Delivery, Bioactivity, and Osteogenic Properties. *Frontiers in Bioengineering and Biotechnology*, *10*, p.994925.

Zhao, R., Shi, L., Gu, L., Qin, X., Song, Z., Fan, X., Zhao, P., Li, C., Zheng, H., Li, Z. and Wang, Q., 2021. Evaluation of Bioactive Glass Scaffolds Incorporating Sro or Zno for Bone Repair: In Vitro Bioactivity and Antibacterial Activity. *Journal of Applied Biomaterials & Functional Materials*, *19*, p.22808000211040910.

APPENDICES

Appendix 1: Ethical clearance certificate

UNAM
UNIVERSITY OF NAMIBIA

ETHICAL CLEARANCE CERTIFICATE

Ethical Clearance Reference Number: JED1822 **Date:** 29 November 2022

This Ethical Clearance Certificate is issued by the University of Namibia Ethics Committee (REC) in accordance with the University of Namibia's Research Ethics Policy and Guidelines. Ethical approval is given in respect of undertakings contained in the Research Project outlined below. This Certificate is issued on the recommendations of the ethical evaluation done by the ethics committee.

Title of Project: DEVELOPMENT AND CHARACTERIZATION OF SINTERED POROUS BIOACTIVE GLASS SCAFFOLDS FOR MEDICAL APPLICATION

Principal researchers: MR LINUS ANGULA

Staff Number/ Student number: 201203016

Remarks:

Centre for Research Services

Take note of the following:

1. Any significant changes in the conditions or undertakings outlined in the approved Proposal must be communicated to the ethics committee. An application to make amendments may be necessary.
2. Any breaches of ethical undertakings or practices that have an impact on ethical conduct of the research must be reported to the ethics committee
3. The Principal Researcher must report issues of ethical compliance to the ethics committee (through the Chairperson) at the end of the Project or as may be requested by the ethics committee
4. The ethics committee retains the right to:

i) Withdraw or amend this Ethical Clearance if any unethical practices (as outlined in the Research Ethics Policy) have been detected or suspected,

ii) Request for an ethical compliance report at any point during the course of the research.

The ethics committee wishes you the best in your research.

Dr. Erasmus Shaanika (Chairperson: Decentralized Ethics Committee)

Prof. Davis Mumbengegwi (Head, Multidisciplinary Research)

Appendix 2: Research permission letter

CENTRE FOR RESEARCH SERVICES
Office of the Pro-Vice Chancellor: Research, Innovation & Development
University of Namibia, Private Bag 13301, Windhoek, Namibia
340 Mandume Ndemufayo Avenue, Pioneers Park, Office F223 - Fblock, Second Floor
☎ +264 61 206 4673; E-mail:kmbulu@unam.na; URL.: http//www.unam.edu.na

UNAM
UNIVERSITY OF NAMIBIA

RESEARCH PERMISSION LETTER

Date: 02 /02/2023

Student Name: LINUS ANGULA

Student Number: 201203016

Programme: Master of Science Metallurgical Engineering

Approved Research Title: DEVELOPMENT AND CHARACTERIZATION OF SINTERED POROUS BIOACTIVE GLASS SCAFFOLDS FOR MEDICAL APPLICATION.

TO WHOM IT MAY CONCERN:

I hereby confirm that the above-mentioned student is registered at the University of Namibia for the programme indicated. The proposed study met all the requirements as stipulated in the University guidelines and has been approved by the relevant committees.

The proposal adheres to ethical principles as per attached Ethical Clearance Certificate. Permission is hereby granted to carry out the research as described in the approved proposal.

Best Regards

Dr. AEE Shikongo
Head: Postgraduate Research Support Services
Tel: +264 61 206 3129
E-mail: aeshikongo@unam.na

CENTRE FOR RESEARCH SERVICES
Office of the Director
2023 -02- 02
University of Namibia
UNAM

Appendix 3: Reagent blending and batch preparation (images).

Figure A-1: Analytical grade starting reagent powders.

Figure A-2: Reagent measuring and batching with a top pan balance.

Figure A-3: Blended reagent batches, bottled for tabular mixing.

Appendix 4: Melting and glass synthesizing (images).

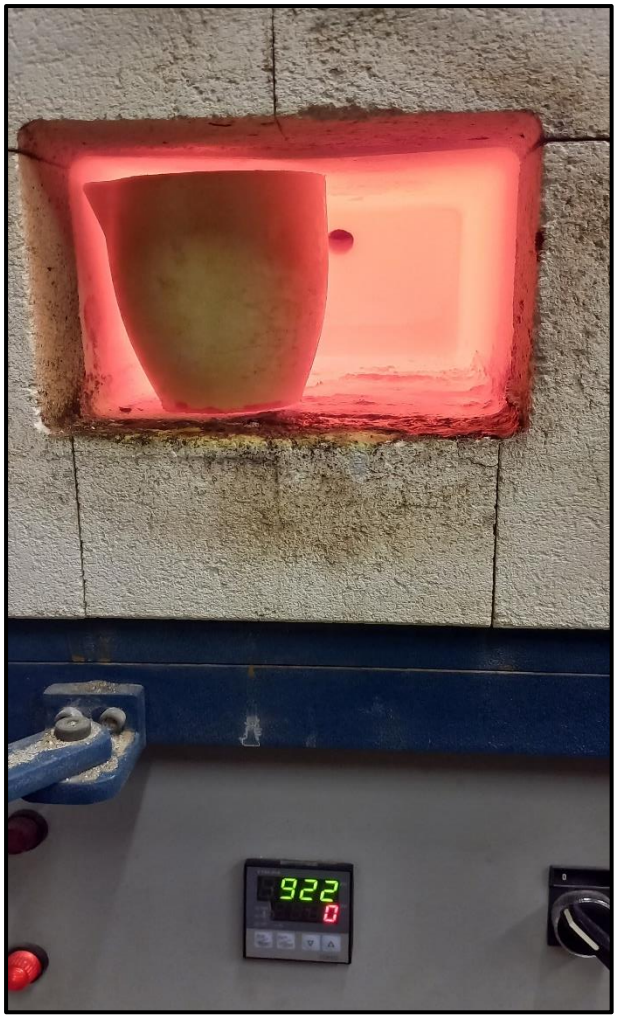

Figure A-4: Operating muffle furnace during melting.

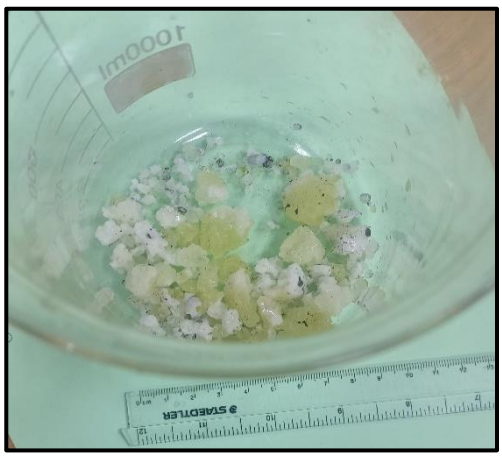

Figure A-5: S53B50 glass frits.

Figure A-6: P40B10 glass frits.

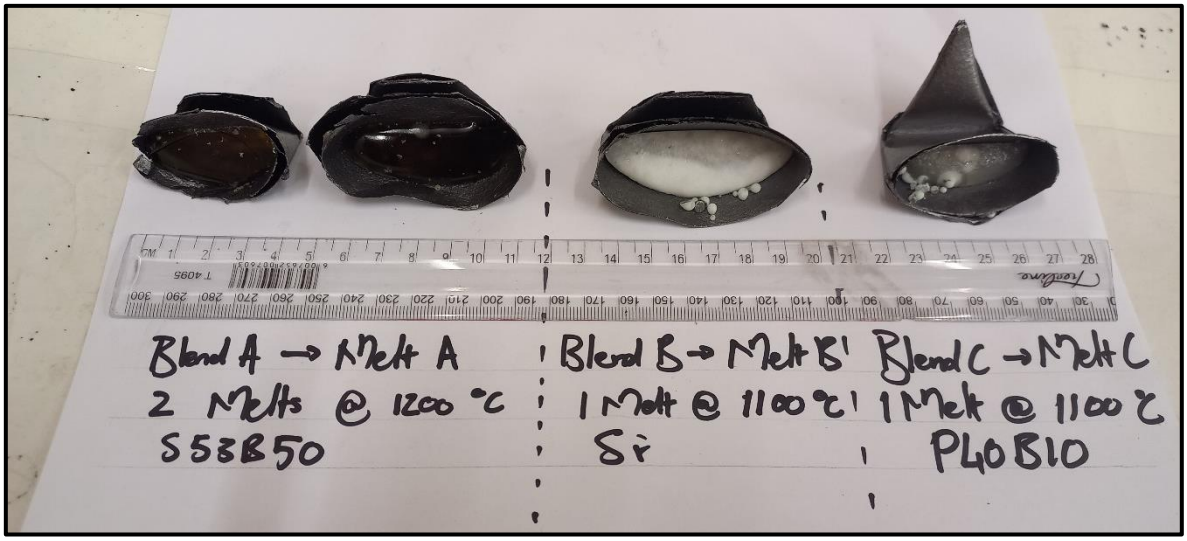

Figure A-7: Glass monoliths in graphite paper after melting and annealing.

Appendix 5: Glass ceramic powder preparation (images).

Figure A-8: Crushed glasses for planetary ball mill charge.

Figure A-9: Zirconium lined milling jars and milling balls for pulverizing.

Figure A-10: X-ray diffraction powder sample preparation.

Appendix 6: SPS porous scaffold fabrication specimen (images).

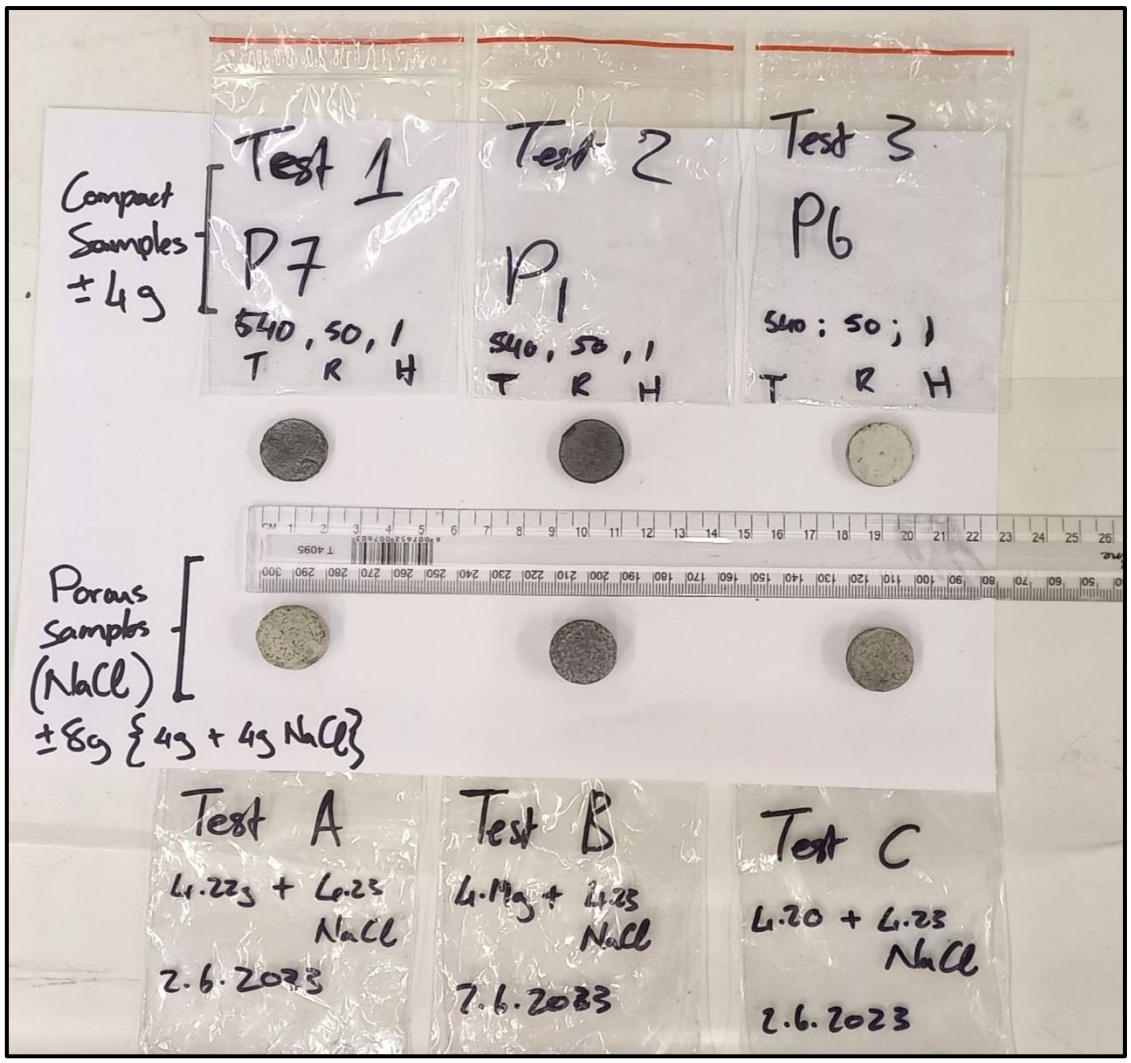

Figure A-11: SPS test specimens comparing dense compact vs porous sintering.

Figure A-12: 20mm diameter maintained after sacrificial porogen removal.